

Optimising NMR Spectroscopy through Method and Software Development

Jonathan Yong

University of Oxford

Contents

Abstract	v
Acknowledgements	vi
Preface	vii
List of figures	xi
List of tables	xv
List of code listings	xvii
1 NMR theory	1
1.1 Quantum mechanics	2
1.2 The rotating frame	5
1.3 Density operators	8
1.4 Pulse sequences	11
1.4.1 1D pulse-acquire	11
1.4.2 INEPT and product operators	15
1.4.3 2D NMR: general principles	19
1.4.4 The States HSQC experiment	23
1.4.5 The echo-antiecho HSQC: gradients and coherence selection	24
1.5 References	32
2 Pure shift NMR	35
2.1 Theoretical background	36
2.2 Pure shift in practice	40
2.2.1 Acquisition modes	40
2.2.2 Pure shift elements	42
2.2.3 PSYCHE in detail	44

2.3	PSYCHE with a variable number of saltires	48
2.4	Direct optimisation of PSYCHE waveform	52
2.4.1	Techniques for pure shift optimisations	52
2.4.2	Flip angle optimisation	56
2.4.3	Waveform parameterisation and optimisation	58
2.5	Time-reversal method	63
2.6	‘Discrete PSYCHE’	67
2.6.1	Speeding up dPSYCHE simulations	68
2.6.2	Optimisations and experimental evaluation	71
2.7	Ultrafast PSYCHE-iDOSY	77
2.8	References	84
3	POISE	93
3.1	Introduction	94
3.2	Technical overview	96
3.2.1	Routines	97
3.2.2	The experiment	98
3.2.3	Optimisation options	99
3.2.4	Optimisation algorithms	99
3.2.5	Implementation details	105
3.3	What POISE is not	108
3.4	Applications	109
3.4.1	Pulse width calibration	109
3.4.2	Ernst angle optimisation	114
3.4.3	Inversion–recovery	118
3.4.4	NOE mixing time	119
3.4.5	ASAP-HSQC excitation delay	123
3.4.6	Ultrafast NMR	126
3.4.7	HMBC low-pass J-filter	131
3.4.8	PSYCHE pure shift NMR	136
3.4.9	Water suppression	141
3.4.10	Diffusion NMR	145
3.5	POISE for ESR	153
3.6	References	155
4	NOAH	164
4.1	Introduction	166
4.1.1	Time savings and sensitivity analyses	166

4.1.2	Magnetisation pools	170
4.1.3	Case studies	172
4.2	GENESIS: automated pulse programme creation	178
4.2.1	Motivation	179
4.2.2	Implementation details	180
4.2.3	Processing improvements	188
4.3	Discussion of individual modules	190
4.3.1	^{13}C sensitivity-enhanced HSQC	190
4.3.2	^{15}N HMQC	203
4.3.3	^{15}N sensitivity-enhanced HSQC	209
4.3.4	Dual HSQC and HSQC-TOCSY	215
4.3.5	HSQC-COSY	224
4.3.6	2DJ and PSYCHE	228
4.3.7	HMBC	230
4.3.8	ADEQUATE	239
4.4	Solvent suppression in NOAH	240
4.4.1	Presaturation	241
4.4.2	Intrinsic suppression	241
4.4.3	Excitation sculpting	242
4.5	Parallel and generalised NOAH supersequences	244
4.6	References	244
A	Other work	234
A.1	NMR plotting in Python	234
A.2	Citation management	235
A.3	Group website and pulse programming tutorials	235
A.4	References	235

refsection:1

refsection:2

refsection:3

refsection:4

Chapter 4

NOAH

chpt : noah

This final chapter describes my work on *NOAH* (NMR by Ordered Acquisition using ^1H detection) *supersequences*, pulse sequences which record multiple 2D datasets (*‘modules’*) in the time required for one. This is an attractive NMR technique for several reasons: the time savings are clearly a key factor, but the flexibility of being able to combine almost any set of modules also makes NOAH supersequences applicable to a variety of contexts.

I begin by introducing the concepts underlying NOAH supersequences, as well as a general discussion of the time savings (and sensitivity per unit time) benefits thus realised. I then describe the GENESIS (GENeration of Supersequences In Silico) website, which allows users to generate Bruker pulse programmes for almost every imaginable NOAH supersequence. After this, my work on various aspects of the actual sequences themselves is described, with a special focus on newly developed and/or improved modules. Finally, the design of ‘parallel’ supersequences which use interleaved and/or time-shared modules is discussed.

This work was done in close collaboration with Ěriks Kupĉe (Bruker UK). However, all results and analysis shown in this chapter are mine. The work in this chapter forms the subject of several publications:

- Yong, J. R. J.; Hansen, A. L.; Kupĉe, Ě.; Claridge, T. D. W. Increasing sensitivity and versatility in NMR supersequences with new HSQC-based modules. *J. Magn. Reson.* **2021**, 329, 107027, DOI: [10.1016/j.jmr.2021.107027](https://doi.org/10.1016/j.jmr.2021.107027)
- Kupĉe, Ě.; Yong, J. R. J.; Widmalm, G.; Claridge, T. D. W. Parallel NMR Supersequences: Ten Spectra in a Single Measurement. *JACS Au* **2021**, 1, 1892–1897, DOI: [10.1021/jacsau.1c00423](https://doi.org/10.1021/jacsau.1c00423)
- Yong, J. R. J.; Kupĉe, Ě.; Claridge, T. D. W. Modular Pulse Program Generation for NMR

Supersequences. *Anal. Chem.* **2022**, *94*, 2271–2278, DOI: [10.1021/acs.analchem.1c04964](https://doi.org/10.1021/acs.analchem.1c04964)

- Yong, J. R. J.; Kupče, Ě.; Claridge, T. D. W. Uniting Low- and High-Sensitivity Experiments through Generalised NMR Supersequences. **2022**, manuscript in preparation

The material in the introductory sections also closely follow two reviews which I have contributed to:

- Kupče, Ě.; Frydman, L.; Webb, A. G.; Yong, J. R. J.; Claridge, T. D. W. Parallel nuclear magnetic resonance spectroscopy. *Nat. Rev. Methods Primers* **2021**, *1*, No. 27, DOI: [10.1038/s43586-021-00024-3](https://doi.org/10.1038/s43586-021-00024-3)
- Yong, J. R. J.; Kupče, Ě.; Claridge, T. D. W. In *Fast 2D solution-state NMR: concepts and applications*, Giraudeau, P., Dumez, J.-N., Eds., forthcoming, 2022

4.1 Introduction

sec:noah__introduction

The characterisation of small molecules and biomolecules by NMR spectroscopy relies on a suite of standard 2D NMR experiments, which seek to detect heteronuclear scalar couplings (e.g. HSQC and HMBC), homonuclear scalar couplings (e.g. COSY and TOCSY), or through-space interactions (e.g. NOESY and ROESY). Although 2D experiments provide far superior resolution and information content compared to 1D spectra, they also require substantially longer experiment durations, as the indirect dimension must be constructed through the acquisition of many t_1 increments. This problem is further exacerbated by the fact that structural elucidation or verification often necessitates the acquisition of several different 2D experiments.

The acceleration of 2D NMR has thus proven to be a popular area of research, and we may broadly categorise the existing techniques into two classes.* Firstly come the methods which seek to directly speed up the acquisition of *individual* 2D spectra: these include non-uniform sampling (NUS),^{7–10} fast pulsing (i.e. shortening of recovery delays),^{11–14} ultrafast NMR,^{5,15–19} Hadamard encoding,^{20,21} and spectral aliasing.^{22–25}

On the other hand, *multiple-FID experiments* aim to collect two or more 2D spectra in the time required for one. The corresponding FIDs may either be detected at the same time (as in time-shared NMR^{26–28} and multiple-receiver NMR^{29–31}), or *sequentially*: NOAH supersequences^{5,32,33} fall under this category. Specifically, NOAH supersequences are set aside from other sequential-acquisition experiments^{34–39} by their ‘modular’ nature: they can be constructed from building blocks which each (usually) contain one FID. Typically, each of these building blocks corresponds to a specific 2D experiment, as will be shown below. It should be noted that there are several other multiple-FID experiments which, while not explicitly advertised as such, are built from ‘modules’ and are conceptually identical to NOAH experiments;^{40–43} I do not discuss these here.

The concatenation of different modules in NOAH supersequences relies on the combination of modules which draw on different *magnetisation pools*. Before explaining this, I first provide an overview of how the time savings for NOAH experiments may be quantified and analysed.

4.1.1 Time savings and sensitivity analyses

subsec:noah__snr

In a typical 2D NMR experiment, the majority of the experiment duration is taken up by the *recovery delay*—the time required for spins to return to their equilibrium polarisation, such that the next transient or t_1 increment can be recorded. The removal (or shortening) of recovery

*These are by no means mutually exclusive: many of the techniques here can be combined to provide even greater efficiency.

./figures/noah/timings.png

Figure 4.1: (a) NOAH-2 SC supersequence, comprising HSQC and COSY modules (see table 4.1 for an explanation of the single-letter module codes used). (b) ‘Conventional’ echo–antiecho HSQC (the same as in fig. 1.7). (c) ‘Conventional’ COSY. The timings referred to in the text are highlighted for all three experiments; I have assumed that d_1 for each experiment is the same. Note that the lengths are not to scale: d_1 is typically far longer than the τ_{ps} and τ_{acq} .

delays is thus a very effective way of speeding up 2D data acquisition. In NOAH supersequences, 2D experiments (‘modules’) can be directly concatenated without the addition of extra recovery delays between them: only one overall recovery delay is required for the entire supersequence. This means that, to a first approximation, a supersequence containing N modules ($N \geq 2$) can be acquired in the time needed for just one module. Figure 4.1 shows an example of a NOAH supersequence formed from two modules (HSQC and COSY): the various timings referred to in the text which follows are also marked on the diagram.

The duration of an NMR experiment, τ_{exp} , can be expressed as a sum of its parts:

$$\tau_{exp} = \tau_{ps} + \tau_{acq} + d_1, \quad (4.1) \quad \text{\small \{eq:exp_duration_2d\}}$$

where τ_{ps} is the time required for the pulse sequence itself (typically several milliseconds), τ_{acq} is the acquisition time (several hundred milliseconds), and d_1 is the recovery delay (one or more

seconds). The *time-saving factor* ρ_t for a NOAH supersequence, as compared to a series of conventional standalone experiments, is then:

$$\rho_t = \frac{\sum_i \tau_{\text{conv}}^{(i)}}{\tau_{\text{NOAH}}} = \frac{\sum_i (\tau_{\text{ps}}^{(i)} + \tau_{\text{acq}}^{(i)} + d_1^{(i)})}{d_1 + \sum_i (\tau_{\text{ps}}^{(i)} + \tau_{\text{acq}}^{(i)})}, \quad (4.2) \quad \{\text{eq:rho}_t\}$$

where τ_{NOAH} is the duration of the NOAH experiment, τ_{conv} is the duration of a conventional experiment, and the superscript (i) represents the i -th module or conventional experiment being acquired. The sum runs from $i = 1$ to N , where N is the number of modules. If we assume that $d_1^{(i)} = d_1$ is the same for all N conventional experiments and the supersequence, then in the limit where

$$d_1 \gg \sum_i \tau_{\text{ps}}^{(i)} + \tau_{\text{acq}}^{(i)}, \quad (4.3) \quad \{\text{eq:d1_limit}\}$$

we have that $\rho_t \rightarrow Nd_1/d_1 = N$. This analysis makes plenty of assumptions, and is not entirely valid in practice. For example, *each* τ_{acq} is often around 5–10% of d_1 , so is not entirely negligible, especially in longer supersequences. Furthermore, some modules require longer τ_{ps} : most notable is the NOESY module, which contains a mixing time of several hundred milliseconds. (HMBC, TOCSY, and ROESY spectra are also lesser offenders.) These factors serve to reduce ρ_t from its idealised value of N ; generally, this deviation is larger as N increases, because eq. (4.3) becomes less and less valid. Nevertheless, the general point that time savings are approximately proportional to N stands.

For relatively concentrated samples, where sensitivity is not an issue, we can in fact end the discussion here. In this *sampling-limited regime*, the minimum 2D experiment duration is dictated purely by the number of t_1 increments needed to obtain sufficient resolution in the indirect dimension, as well as the minimum phase cycle required for artefact suppression.* NOAH supersequences are identical to conventional experiments in both aspects, but provide a time-saving factor of $\rho_t \sim N$.

The development of modern NMR instrumentation, including high-field magnets and cryogenic probes, means that the sampling-limited regime continues to be extended to ever lower concentrations. However, it is often not this simple: the opposite *sensitivity-limited regime* is still very commonly encountered, for example with naturally insensitive experiments (e.g. ADEQUATE), low-field benchtop NMR, or most simply, dilute samples.†

In such cases, it becomes mandatory to compare the SNRs of the NOAH modules and con-

*With modern gradient-enhanced experiments, the minimum phase cycle may well not even be a ‘cycle’; see also fig. 1.8.

†If the SNR factor $A^{(i)}$ as discussed below is *very small*, then it is possible that even concentrated samples may be shifted into the sensitivity-limited regime. This is never really the case in practice, though, as will be shown in § 4.1.3.

ventional experiments. To do so, we define for each module an *SNR factor* $A^{(i)}$, which is the SNR of the NOAH module divided by the SNR of a conventional experiment, acquired with the same parameters.* In general, we have that $A \leq 1$, because NOAH modules frequently contain small modifications from conventional experiments (as will be explained in § 4.1.2). The *gain in sensitivity per unit time*, $\varepsilon^{(i)}$, is then defined by

$$\varepsilon^{(i)} = A^{(i)} \sqrt{\rho_t}, \quad (4.4) \quad \{\text{eq:varepsilon}_i\}$$

where the square root accounts for the fact that SNR scales only as the square root of the number of scans, or the number of times the experiment can be repeated in a given period. Of course, the exact values calculated for $A^{(i)}$ (and hence $\varepsilon^{(i)}$) will depend on the sample chosen for the comparison. These values should therefore be assumed to be valid only for similar samples.

If $\varepsilon^{(i)} > 1$, as is frequently the case, this means that the NOAH supersequence provides greater sensitivity per unit time in the i -th module compared to a standalone experiment. Equivalently, performing a NOAH experiment allows data of sufficient sensitivity to be obtained in less time. Naturally, this condition is most important for modules which are inherently insensitive, particularly heteronuclear correlation modules. For sensitive (typically homonuclear) modules, it is often perfectly tolerable to have $A < 1$ or even $\varepsilon < 1$, as even with this sensitivity penalty they are still more intense than the heteronuclear modules.

Another issue with NOAH supersequences is that each module is run with the same number of scans (phase cycle). Although this was touted as a benefit in the sampling-limited regime, this may in fact be undesirable in the sensitivity-limited regime, where insensitive experiments need to be run with more scans than sensitive ones. In this case, the *effective* time savings provided by NOAH experiments are smaller:

$$\rho_{t,\text{eff}} = \frac{\sum_i \tau_{\text{conv}}^{(i)}}{\tau_{\text{NOAH}}} = \frac{\sum_i S^{(i)} (\tau_{\text{ps}}^{(i)} + \tau_{\text{acq}}^{(i)} + d_1^{(i)})}{S d_1 + S \sum_i (\tau_{\text{ps}}^{(i)} + \tau_{\text{acq}}^{(i)})}, \quad (4.5) \quad \{\text{eq:rho}_t\text{-eff}\}$$

where each standalone experiment is acquired with $S^{(i)}$ scans and the NOAH experiment with S scans. Typically, S is simply the largest of the $S^{(i)}$. If $S^{(i)} = S$ for all i , then eq. (4.5) simply reduces to eq. (4.2); on the other hand, if the $S^{(i)}$'s are different, then we have that $\rho_{t,\text{eff}} < \rho_t$. In such a situation, it is probably more appropriate to describe a NOAH supersequence as ‘measuring the most insensitive module and getting the others for free.’ Indeed, if $S = S^{(i)} \gg S^{(j \neq i)}$, then ‘the other’ modules require almost no time to measure (relative to the least sensitive module), and $\rho_{t,\text{eff}}$ tends towards 1, meaning that even the time-saving utility of NOAH vanishes. A corollary

*The relative SNR will likely vary from peak to peak in the spectrum, and $A^{(i)}$ should in theory be quoted either as an average over all peaks, or as a range. This is what I have done in this thesis. However, comparisons in the literature are not always as thorough.

of this is that NOAH supersequences are generally best constructed from modules which have similar intrinsic sensitivities and hence similar $S^{(i)}$'s.

As the reader can no doubt appreciate by now, the comparison of NOAH and conventional spectra is fraught with subtleties (which are sometimes glossed over in the literature, but invariably surface in real-life discussions). In fact, it is not difficult to construct yet more edge cases. For example, one may not want to acquire all the individual spectra ‘conventionally’: for example, NUS may be used for an HSQC experiment but not for others; or d_1 may be varied for different experiments. These will have an impact on both the durations of the experiments, as well as their sensitivities. To make any meaningful quantitative comparisons, it is therefore necessary to restrict the discussion to values of ρ_t , A , and ε , which can be objectively calculated. These should of course be read with the qualitative understanding that depending on the context, these aforementioned factors may lead to *some*—but never a *complete*—decrease in the utility of NOAH experiments.

4.1.2 Magnetisation pools

Having gotten this relatively dry material out of the way, I now turn to exactly how NOAH supersequences are constructed. Ordinarily, if the recovery delay is removed from an NMR experiment, its sensitivity will be greatly reduced because insufficient magnetisation will have recovered between repetitions; or in other words, $A^{(i)}$ will be very small. Such experiments would only really be useful well in the sampling-limited regime.

The key to avoiding this in NOAH supersequences is to make sure that *each module samples a different source of magnetisation*. For example, an HSQC module can be designed to only sample magnetisation of protons directly bonded to the 1.1%-natural abundance ^{13}C , and leave all other proton magnetisation untouched. Immediately following this, the remainder of the proton magnetisation can then be used to record (say) a COSY module, without needing a separate recovery delay. Using the notation of Orts and Gossert,⁴⁴ the magnetisation of ^{13}C -bound protons is denoted as $^1\text{H}^{\text{C}}$, and the magnetisation of protons *not* bonded to ^{13}C is denoted as $^1\text{H}^{\text{!C}}$. Protons not directly bonded to NMR-active heteronuclei are labelled $^1\text{H}^{\text{!X}}$, and will often be referred to as ‘bulk’ magnetisation, since (in natural-abundance samples) the majority of protons fall into this category.

Most standard 2D experiments do not preserve unused magnetisation but instead dephase it through CTP gradient selection; thus, NOAH modules often require some modifications compared to standard experiments. For example, compared to the echo–antiecho HSQC (discussed in § 1.4.5), the NOAH HSQC module³² adds an extra CTP gradient so that the bulk magnetisation is refocused and ultimately returned to the $+z$ equilibrium state (fig. 4.2a). (This is largely

identical to the ‘symmetrised’ ASAP-HSQC experiment.⁴⁵⁾

./figures/noah/hsqc_hmbc_prodops.png

figfigoebabbspob

Figure 4.2: (a) NOAH HSQC module. (b) NOAH HMBC module. The 90° pulse highlighted in red is described in § 4.3.7. Delays are set as: $\Delta = 1/(4 \cdot {}^1J_{\text{CH}})$; $\Delta_{\text{LR}} = 1/(2 \cdot {}^nJ_{\text{CH}})$; $\tau_1 = 1/(2 \cdot {}^1J_{\text{CH,max}})$; $\tau_2 = 1/(2 \cdot {}^1J_{\text{CH,min}})$ (see also § 3.4.7 for the LPJF). Phase cycling is performed with $\phi_1 = (x, -x)$, $\phi_2 = (x, x, -x, -x)$, and $\phi_{\text{rec}} = (x, -x, -x, x)$. Gradient amplitudes are $(g_1, g_2, g_3, g_4, g_5) = (80\%, \pm 40.2\%, 15\%, -10\%, -5\%)$. Product operator analysis is provided above both modules for both the ${}^1\text{H}^{\text{C}}$ and ${}^1\text{H}^{\text{I}^{\text{C}}}$ magnetisation pools; the notation for this is explained in the *Preface*.

Sometimes, the modifications required are more extensive, as in the HMBC module. If this module is followed by an HSQC module (or any other module which draws on ${}^1\text{H}^{\text{C}}$ magnetisation), the initial 90° excitation pulse must be replaced with a *zz*-filter (fig. 4.2b). This performs an *isotope-selective rotation* in that ${}^1\text{H}^{\text{C}}$ magnetisation is stored along the *z*-axis, but ${}^1\text{H}^{\text{I}^{\text{C}}}$ magnetisation is excited (and subsequently detected). In general, sequences which are thus modified have lower sensitivities (i.e. $A < 1$) than the ‘original’ sequences from which they were derived. This is partly because of imperfect manipulation of magnetisation by the extra pulse sequence elements, and also increased losses due to relaxation during these extended sequences.

In contrast, modules placed towards the *end* of a supersequence do not need to be modified, as they do not need to preserve any magnetisation. This includes virtually all homonuclear modules, which are allowed to simply consume any remaining magnetisation. Although this makes their

implementation very straightforward, in general these modules will *also* suffer some losses in sensitivity, because the preceding modules do not perfectly retain all magnetisation.

Thus, in general, it is not possible for any module in a NOAH supersequence to have $A = 1$, unless it is placed first in the supersequence *and* has not undergone any modifications.* Such cases are very rare, and it is thus necessary to accept some decreases in A , which are often fairly small (on the order of 10–20%). In the sampling-limited regime, sensitivity is not at a premium and this is often perfectly tolerable. In the sensitivity-limited regime, the full time savings ρ_t cannot be realised, but since ε is still typically larger than 1, there is still an overall boost in sensitivity per unit time.

4.1.3 Case studies

Using all that has been described in the previous sections, we now look at a few ‘typical’ supersequences to understand their construction. A quick note about the nomenclature of NOAH supersequences is warranted here. Supersequences are labelled by the number of modules N , plus a series of single-letter codes corresponding to the identity and ordering of the modules involved (table 4.1). Occasionally, superscripts or subscripts are used to qualify the modules involved.† Thus, a NOAH supersequence containing three modules—say ^{15}N HMQC, ^{13}C HSQC, and CLIP-COSY—would be referred to as a NOAH-3 $\text{M}_{\text{N}}\text{SC}^{\text{C}}$. Table 4.2 provides values of ρ_t and A for each module of several typical supersequences, which will be rationalised in the text which follows.

NOAH-2 SC: HSQC + COSY

We begin with perhaps the simplest example of a NOAH supersequence, one containing the HSQC and COSY modules: this is labelled as a NOAH-2 SC experiment (entry 1, table 4.2). As shown in fig. 4.2a, the HSQC module only samples $^1\text{H}^{\text{C}}$ magnetisation, and leaves $^1\text{H}^{\text{C}}$ magnetisation along the $+z$ -axis. Although the HSQC experiment has to be modified to preserve this $^1\text{H}^{\text{C}}$ magnetisation, its sensitivity is practically unaffected as compared to a ‘standard’ HSQC ($A = 0.97$). Furthermore, the COSY module retains *most* of its sensitivity ($A = 0.90$). The small loss here is because the HSQC module does not *perfectly* preserve the $^1\text{H}^{\text{C}}$ magnetisation: for example, evolution of J-couplings as well as relaxation occur during the HSQC pulse sequence,

*Of course, this also depends on exactly *what* standalone experiment the NOAH supersequence is being compared against. Sometimes, in the literature, the NOAH experiment has been compared against its constituent modules acquired in a standalone fashion; in this case, the first module will always have $A = 1$. This tells us how much we gain through the act of concatenating modules, but is less meaningful in the ‘real world’ where one is interested in how useful NOAH is relative to ‘typical’ optimised 2D experiments. I therefore prefer to make comparisons against standard-library sequences.

†With the increasing number of modules, and the variety of modern NMR experiments which could be incorporated into NOAH supersequences, keeping these abbreviations short yet meaningful has been a challenge.

^1H - ^{15}N modules		^1H - ^{13}C modules		^1H - ^1H modules	
Module	Code	Module	Code	Module	Code
HMQC	M_N	HSQC	S	COSY	C
HSQC	S_N	seHSQC	S^+	CLIP-COSY	C^c
seHSQC	S_N^+	HSQC-TOCSY	S^T	DQF-COSY	C
HMBC	B_N	HSQC-COSY	S^C	TOCSY	T
		2BOB	O	NOESY	N
		HMBC	B	ROESY	R
		ADEQUATE	A	PSYCHE	P
				TSE-PSYCHE	P^T
				PSYCHE 2DJ	J

tbl:noah_modules

Table 4.1: A (non-exhaustive) list of single-letter module codes for a selection of NOAH modules. Note that, in the literature, the ^{15}N HMQC module has been referred to simply by ‘M’, since the HSQC module is preferred for ^1H - ^{13}C correlations. In this thesis, I include the subscript N throughout to avoid any ambiguity.

Entry	Sequence	τ_{NOAH}	ρ_t	A				
				HMBC	seHSQC	HSQC	COSY	TOCSY
1	SC	15 min 0 s	1.87			0.97	0.90	
2	SCT	16 min 25 s	2.60			1.01	0.99	0.79
3	BS	15 min 40 s	1.82	0.93		0.87		
4	SB	15 min 35 s	1.83	0.99		0.96		
5	BSCT	17 min 48 s	3.22	0.95		0.90	0.36	0.28
6	BS_N^+ SCT	18 min 57 s	3.74	0.95	0.71	0.66	0.38	0.30
7	S_N^+ BSCT	18 min 56 s	3.75	0.76	0.79	0.74	0.33	0.26

tbl:noah_sensitivities

Table 4.2: Sensitivity and time-saving analyses of several typical NOAH supersequences. All experiments were acquired with 2 scans per increment, 256 t_1 increments, an acquisition time of 67 ms, and a recovery delay of 1.5 s. The HMBC module used here includes the extra ^{13}C 90° pulse described later in § 4.3.7: this has no significant impact on the SNR, and is only mentioned as a technicality. The ^{15}N seHSQC module is that described in § 4.3.3. The CT module here was run with States indirect-dimension quadrature detection, and the individual C module (in entry 1) with echo-antiecho. The following Bruker library sequences were used as the ‘conventional’ experiments: hmbcetgp12nd, hsqcetf3gpsi2, hsqcetgpsp.2, cosygpqf, and dipsi2gpshz. *Data code:* 7Z-220224.

which are ignored in the product operator analysis in fig. 4.2a.

The value of the time-saving factor, $\rho_t = 1.87$, is very close to the theoretical limit of $N = 2$. This reflects the fact that the pulse sequence itself, τ_{ps} , is fairly short for both the HSQC and COSY modules; the deviation therefore chiefly arises from the acquisition time, τ_{acq} . In all respects, this is therefore an example of an ‘ideal’ NOAH supersequence, where the combination of two modules provides time savings without compromising on sensitivity.

It is worth pointing out that the order of the modules cannot be reversed: the COSY module cannot be (easily) modified to preserve $^1\text{H}^{\text{C}}$ magnetisation. In a hypothetical NOAH-2 CS supersequence, the later HSQC module would only be able to use magnetisation recovered during the COSY FID, leading to substantial sensitivity drops.

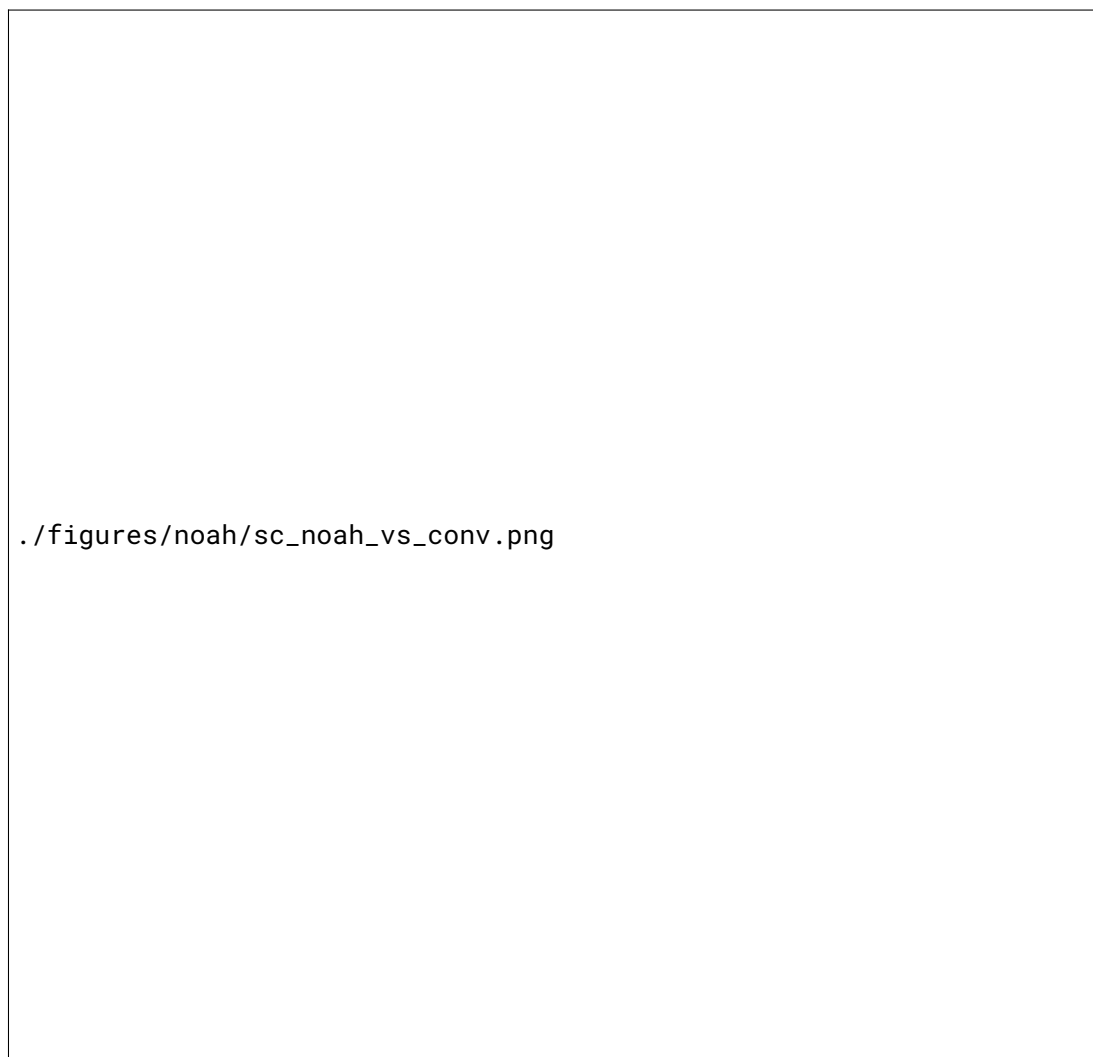


Figure 4.3: (a) HSQC from NOAH-2 SC supersequence. (b) COSY from NOAH-2 SC supersequence. (c) Standalone HSQC. (d) Standalone COSY; off-diagonal artefacts are highlighted in the red box. Data code: 7Z-220224.

A final point to consider would be whether the NOAH data has comparable spectral quality in terms of (for example) artefacts. In this case, the answer is yes: the NOAH HSQC spectrum is virtually identical to the standalone (figs. 4.3a and 4.3c; both spectra have low-level artefacts of different kinds, which do not seriously impede the interpretation and are not shown). On the other hand, the NOAH COSY spectrum seems to actually *improve* on the standalone COSY, in that it better suppresses off-diagonal artefacts (figs. 4.3b and 4.3d). These artefacts likely arise in the standalone COSY because of accidental refocusing of magnetisation which has not completely

relaxed between t_1 increments.⁴⁶ In contrast, the NOAH COSY module has an extra set of HSQC gradients between every repetition of the COSY, so accidental refocusing is less likely. (Similar artefacts have been noted before in the DQF-COSY experiment,^{47,48} and have also shown to be attenuated in the corresponding NOAH module.⁴⁹) That said, such improvements are not always guaranteed: there are sometimes artefacts which arise uniquely in NOAH experiments, some of which are discussed in the following sections.

NOAH-3 SCT: HSQC + COSY + TOCSY

Evidently, the fact that the HSQC preserves almost all $^1\text{H}^{13}\text{C}$ magnetisation means that *any* homonuclear module—or a combination thereof—can be placed after it. In general, since homonuclear modules tend to consume any remaining bulk magnetisation, it is very difficult to create combinations of homonuclear modules which do not lead to significant reductions in sensitivity. The only real exceptions are COSY/X combinations, where X can be NOESY, ROESY, or TOCSY: instead of concatenating the COSY and X modules, the COSY pulse sequence can instead be nested *within* the X module, as was first demonstrated with X = NOESY.^{34,35} Here, we use the COSY/TOCSY combination as an example.³⁷ The COSY, TOCSY, and combined COSY/TOCSY modules are shown in fig. 4.4.

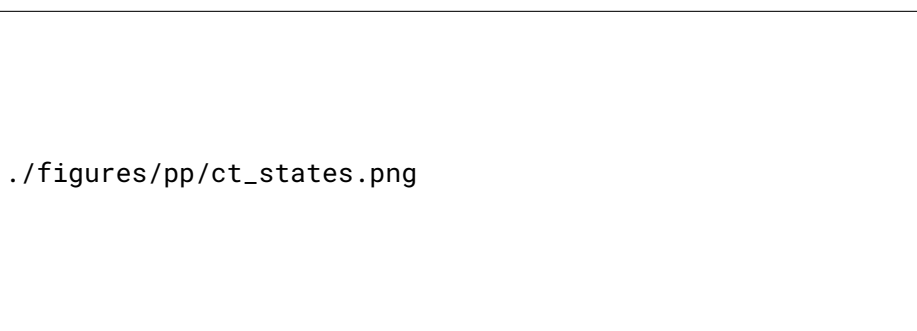


Figure 4.4: (a) COSY module. (b) TOCSY module; zero-quantum suppression is employed before and after the isotropic mixing period. (c) Combined COSY/TOCSY module, where the COSY FID is acquired immediately before the TOCSY mixing.

As shown in table 4.2 (entry 2), this nesting of the COSY module does not materially affect the TOCSY sensitivity. A small loss of approximately 20% is observed, which is partly due to the imperfect magnetisation preservation by the HSQC, and perhaps also due to relaxation during the COSY acquisition period. As for the time-saving factor, a slightly larger deviation ($\rho_t = 2.60$) is observed from the ideal value of 3. This reflects the addition of a TOCSY mixing period, which contributes to τ_{ps} .

NOAH-2 BS: HMBC + HSQC

As mentioned previously, the HMBC module shown in fig. 4.2b is designed to retain $^1\text{H}^\text{C}$ magnetisation through the addition of the zz -filter. This can be used in a subsequent HSQC module in a NOAH-2 BS supersequence. Entry 3 of table 4.2 shows that the addition of the zz -filter to the HMBC causes a relatively small 7% decrease in sensitivity; on the other hand, the HSQC loses 13% of its sensitivity because of incomplete magnetisation preservation.

Generally, it has been recommended that less sensitive modules are placed earlier in the supersequence so that they can access a larger proportion of the equilibrium magnetisation. Since the HMBC is less sensitive of the two modules, this rule of thumb suggests that the BS supersequence would be better than the alternative SB supersequence. In fact, the opposite is true, as entry 4 of table 4.2 shows. The HSQC module has a boost in sensitivity because it is placed first in the supersequence, and no longer needs to rely on the $^1\text{H}^\text{C}$ magnetisation preserved by the HMBC; and the HMBC also benefits because the zz -filter modification is no longer needed.* Arguably, the ordering of modules in a supersequence should be considered on a case-by-case basis.

NOAH-4 BSCT: HMBC + HSQC + COSY + TOCSY

We now move on to a longer supersequence containing four modules, with a correspondingly larger ρ_t value of 3.22. The sensitivity of the HSQC module is practically the same as in the NOAH-2 BS supersequence just described: however, the COSY and TOCSY modules expose one weakness of the HMBC module which has so far been overlooked. In principle, the HMBC module should only excite magnetisation of protons which are long-range coupled to ^{13}C (which we could, for example, denote as $^1\text{H}^\text{C(LR)}$). This magnetisation pool should be separate from both the directly coupled protons ($^1\text{H}^\text{C}$), as well as protons which are not coupled to any ^{13}C at all ($^1\text{H}^\text{C}$). Unfortunately, this is not the case: it is not actually possible to separate the $^1\text{H}^\text{C(LR)}$ and $^1\text{H}^\text{C}$ magnetisation pools. The HMBC excites both of these magnetisation sources, dephases the latter using CTP gradients, and detects the signal arising from the former.

What this means, of course, is that the COSY/TOCSY module which rely on $^1\text{H}^\text{C}$ magnetisation will have substantially lower sensitivities. The signal detected in these two modules derives only from whatever has recovered during the previous two acquisition periods, as shown in entry 5 of table 4.2: A for COSY and TOCSY is 0.36 and 0.28 respectively. That said, this is in fact not likely to be an issue *even* for sensitivity-limited samples. Because the intrinsic sensitivity of the HMBC is orders of magnitude lower than the COSY and TOCSY, even with these large losses in sensitivity, the COSY and TOCSY spectra still have greater intensities than the HMBC. Thus, as long as the entire supersequence is acquired with enough scans to make the HMBC

*In fact, the final 180° pulse in the HMBC module could also be removed: this is likely to give a further boost in SNR, as discussed in § 4.3.7. However, this was not done here.

SNR sufficient, the SNR in the COSY and TOCSY will *also* be acceptable. This is illustrated in fig. 4.5.

A rather more insidious problem is that different signals relax at different rates: thus, the COSY and TOCSY spectra (or indeed, any homonuclear module) will have uneven intensities and are frequently asymmetric. This can be seen in the COSY spectrum, where a pair of asymmetric crosspeaks are highlighted. Adding a period of isotropic mixing before the COSY module⁵⁰ can help to ameliorate this to some extent (this was not performed when acquiring the data in fig. 4.5).

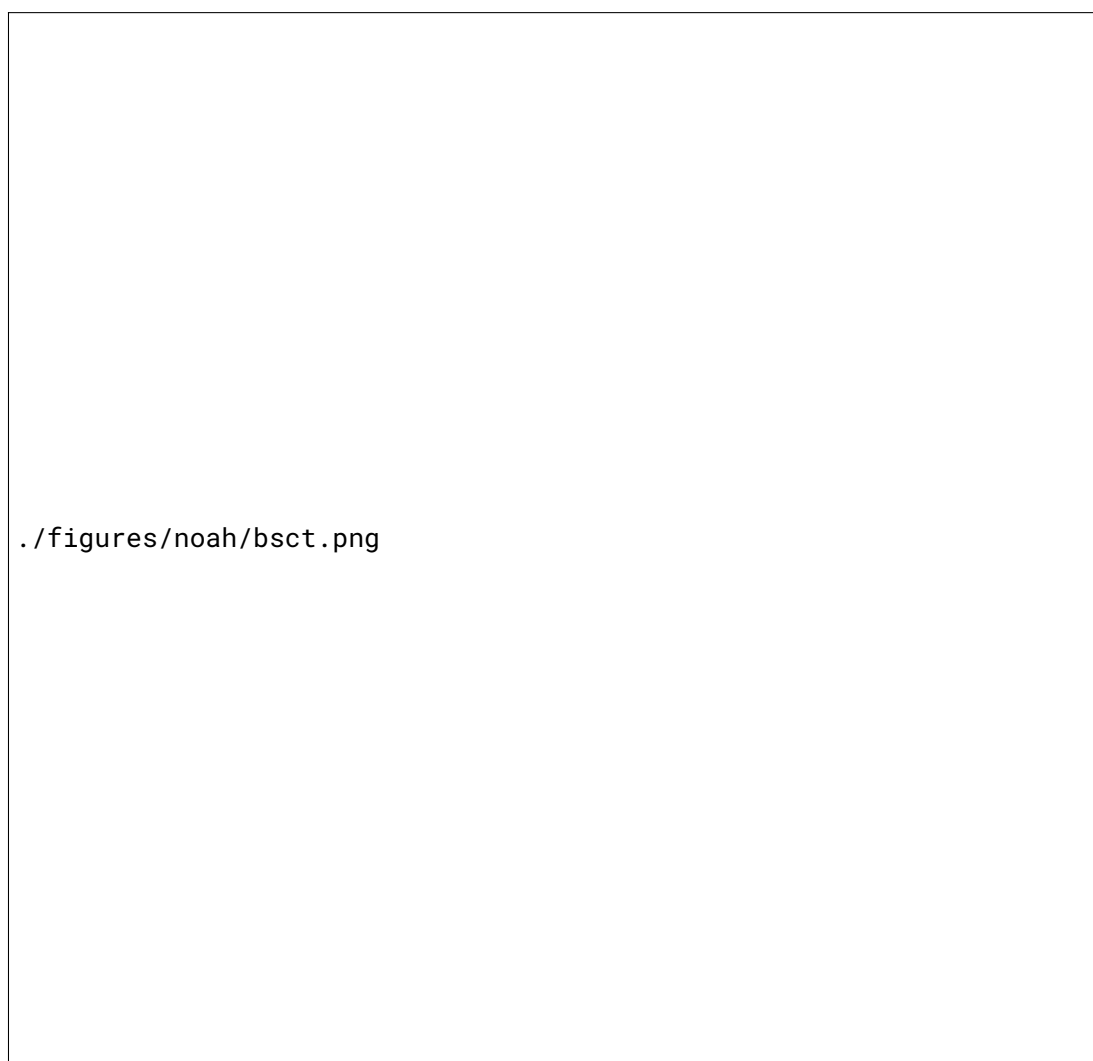


Figure 4.5: Spectra obtained from a NOAH-4 BSCT supersequence. (a) HMBC. (b) HSQC. (c) COSY; a pair of asymmetric crosspeaks are highlighted with red arrows. (d) TOCSY (60 ms DIPSI-2 mixing). Despite the COSY and TOCSY having only $\sim 30\%$ sensitivity compared to standalone experiments, the intensity of the spectra obtained is still perfectly acceptable (the contour levels chosen are 1–2 orders of magnitude larger than for the HMBC). *Data code:* 7Z-220224.

NOAH-5 BS_N⁺SCT: HMBC + ¹⁵N seHSQC + HSQC + COSY + TOCSY

As the final example, we add a further magnetisation pool to the mix, namely protons directly coupled to ¹⁵N (i.e. ¹H^N). As of the time of writing, the implementation of multiple-FID experiments on Bruker spectrometers limits N to a maximum of 5, so a supersequence such as the present NOAH-5 BS_N⁺SCT is the current limit. (However, there is no *scientific* argument forbidding $N > 5$, and it is likely that in future versions of TopSpin this restriction will be lifted.)

The values of A for each module are given in entry 6 of table 4.2. If the HMBC module is placed at the beginning of the supersequence, then in order to preserve *both* ¹H^N and ¹H^C magnetisation, the zz-filter must be extended to include ¹⁵N pulses.⁵¹ As before, the ¹⁵N seHSQC and ¹³C HSQC modules both suffer drops in sensitivity. For the ¹⁵N seHSQC, this is partly because of imperfect preservation of ¹H^N magnetisation by the HMBC, but also stems from the addition of the zz isotope-selective pulse (ZIP) element to the seHSQC pulse sequence; this is described further in § 4.3.3. On the other hand, for the ¹³C HSQC, the sensitivity loss stems purely from imperfect retention of ¹H^C magnetisation. Finally, because the HMBC dephases ¹H^IX magnetisation, the COSY and TOCSY at the end have lower sensitivities: however, as discussed above, this is not an issue in practice.

It is also possible to move the ¹⁵N seHSQC module to the front: this gives it a slightly greater sensitivity, at the cost of the HMBC (entry 7, table 4.2). In general, these two modules tend to have comparable sensitivity, and which of these two arrangements is better depends on which module the sensitivity needs to be optimised for.

Lastly, the value of ρ_t given here of 3.74 represents an effective upper limit on the time-saving factor. Although ρ_t increases with N , the extent to which it deviates from the ideal value of N also increases: it is very difficult to obtain $\rho_t > 4$, even with five modules in the supersequence. Of course, it is possible to increase ρ_t further by lengthening the recovery delay d_1 used for the experiments: for example, if d_1 is increased to 2 s from its present value of 1.5 s, ρ_t increases to 3.94. Obviously, this can only be pushed so far before it becomes meaningless.

4.2 GENESIS: automated pulse programme creation

sec:noah__genesis

In this section, I discuss the development of the GENESIS (GENeration of Supersequences In Silico) website (fig. 4.6): as the name suggests, it automatically generates pulse programmes for arbitrary NOAH supersequences. The website also provides extensive instructions on acquiring and processing NOAH data. Although this may at first glance appear slightly out of chronological order, in that the paper³ was published later than much of the other work in this chapter, an early

version of the GENESIS tool was in fact created much earlier (by July 2020).

The present version of GENESIS is available at <https://nmr-genesis.co.uk>; the source code can also be obtained from <https://github.com/yongrenjie/genesis>.

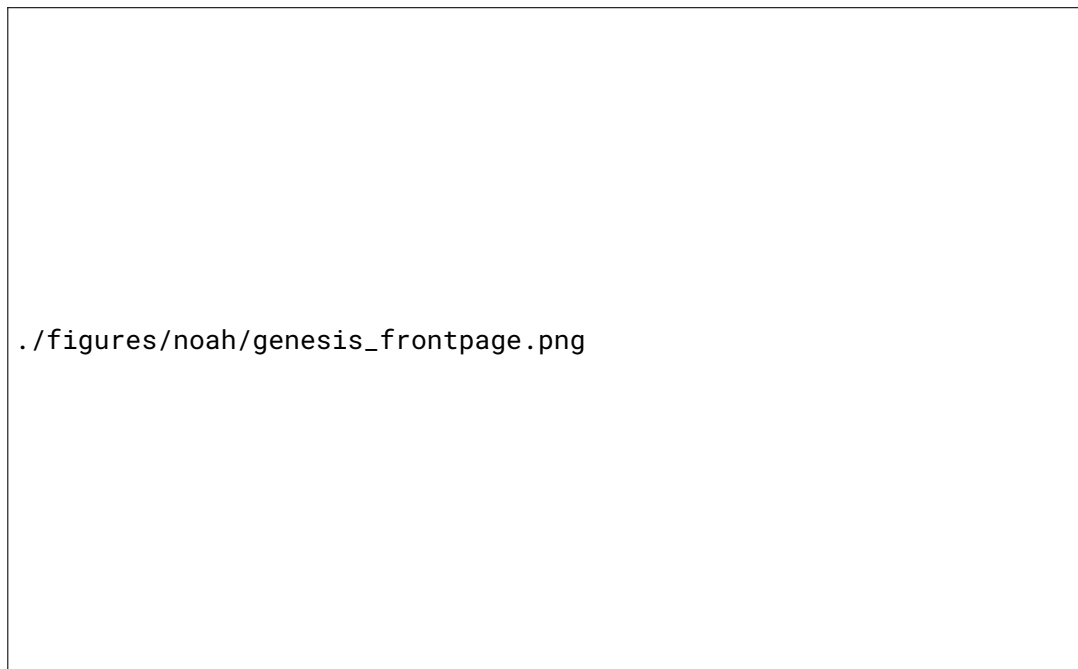


Figure 4.6: The front page of the GENESIS website (<https://nmr-genesis.co.uk>), as of 10 September 2022.

4.2.1 Motivation

From the preceding discussion in § 4.1, it is clear that modules which use different magnetisation pools can be combined almost at will. It does not matter *what* modules they are, merely what magnetisation pools they consume (and preserve). Thus, for example, the NOAH-2 SC supersequence can in fact be generalised to any $^1\text{H}^{\text{C}}$ module plus any $^1\text{H}^{\text{C}}$ module. Very broadly speaking, we may define a generic supersequence as having any or all of the following:

- a HMBC module, which actually uses $^1\text{H}^{\text{X}}$ magnetisation but can be placed at the front as discussed in the NOAH-3 BSC example above;
- a $^1\text{H}^{\text{N}}$ module;
- one or more $^1\text{H}^{\text{C}}$ modules (it is possible to partition the $^1\text{H}^{\text{C}}$ magnetisation pool between two modules, as will be discussed in § 4.3.4);
- one or more $^1\text{H}^{\text{X}}$ modules which consume bulk magnetisation.

In the first NOAH paper in 2017,³² a total of 285 ‘viable’ supersequences were already listed. If

we further take into account some of the new modules which were developed over the course of my DPhil (§ 4.3), the generic formula above provides for over 4000 viable supersequences.* (‘Non-viable’ sequences would be those which have undesirable drawbacks: for example, wrongly ordered modules like in a NOAH-2 CS supersequence.)

In spite of this, *only around 45 pulse programmes* had been made available (either via the supplementary information of NOAH papers, or the Bruker User Library). Traditionally, pulse programmes must be written by hand, which is a laborious and fairly error-prone process made worse by the sheer length of NOAH experiments. Doing this for thousands of supersequence is clearly impractical; furthermore, each time a new module is developed, or an old module is improved, updating every relevant supersequence would itself already be a mammoth task. This explains why—although the NOAH concept provides a clear blueprint for how supersequences may be constructed—there is still a huge gap between theory and practice.

To bridge this gap, I turned towards the *programmatic* generation of pulse programmes.† This not only allows for existing supersequences to be generated at will, but also provides an easy way for updates to be rapidly disseminated to the NMR community. Furthermore, a website can serve as a ‘one-stop’ shop where—after downloading pulse programmes—users may download the associated NOAH processing scripts and also access instructions on how to run NOAH experiments. This information did already exist, but was scattered across several different websites and/or journal supplementary information documents, and would have been needlessly confusing to a new user (not to mention the different versions of scripts available in different publications).

4.2.2 Implementation details

I will now describe a few features of GENESIS pulse programmes, as well as how these are implemented. The GENESIS code is written in TypeScript; during deployment, this is compiled to JavaScript, which can then be directly executed in the client’s web browser. No server-side code is required, meaning that the GENESIS web page is actually a static site (it is currently hosted using GitHub Pages).

*This is also ignoring the ‘parallel’ supersequences, which are discussed in § 4.5. The support for parallel supersequences in GENESIS is not complete: integrating these fully would require substantial changes to the user interface, which I have not had time to do.

†This is actually a bit of a lie: GENESIS was initially created for my own convenience. Throughout this chapter, I have had to perform many comparisons of different supersequences, and this tool spared me from having to write everything by hand (and—more often than not—subsequently discover mistakes which invalidated the results). Of course, it soon became apparent that it could find much wider use.

```

/* PREAMBLE */
; gns_noah2-SCqf
; 13C HSQC
; 1H magnitude-mode COSY
"d4          = 0.25s/cnst2" ; 13C INEPT
"in0         = inf1/2"      ; 13C HSQC increment
"in11        = 2*dw"        ; COSY increment
; ...
define delay DC_HSQCa
"DC_HSQCa    = d4-p14/2"
"l0          = td1/2"      ; TD1/NBL

/* MAIN SECTION */
1 ze
4 d1 st0
  ; MODULE 1 - HSQC
  (p1 ph0):f1
  ; ...
  goscpn ph30 cpd2:f2
  50u do:f2
  2m st
  ; MODULE 2 - COSY
  (p1 ph12):f1
  ; ...
  go=2 ph26
  1m iu1      ; TD1/NBL counter
  1m igrad EA ; echo-antiecho gradients
  1m id11     ; COSY t1
  30m wr #0 if #0 zd
if "l1 % 2 == 0" {
  1m id0      ; HSQC t1
}
  lo to 4 times l0
exit

/* EPILOGUE */
ph0=0
;gpnam4: SMSQ10.100
;gpz4: 70% (13C CTP)
;cpd2:wvm:wudec: cawurst_d-20(220 ppm, 1.4 ms; L2H)
;d4: 1/4J(CH)
;auprog: noah_hsqc:noah_cosy QF
;module identifiers: C_HSQC H_COSY_QF
;pulse programme created by genesis-v2.2.2, https://nmr-genesis.co.uk
;Sun Sep 11 2022 16:04:54 GMT+0800 (Malaysia Time)

```

Listing 4.1: Abridged GENESIS pulse programme for the NOAH-2 SC supersequence shown in fig. 4.1a.

Overall structure

The algorithm used for pulse programme construction can loosely be separated into three parts, which are shown in listing 4.1:

1. the *preamble*, which consists of everything up until the beginning of the actual pulse sequence (the `ze` command). This includes header comments as well as definitions of parameters, such as delays and pulse widths;
2. the *main section*, which contains the actual pulse sequence;
3. the *epilogue*, which contains phase cycle information as well as footer comments describing each parameter. Instructions for generating shaped pulses using Bruker's WaveMaker software are also included here, as well as instructions for automatic processing (§ 4.2.3), and comments indicating how the pulse programme was generated (for reproducibility purposes).

The construction of the preamble and main section is largely accomplished through the collation of module-specific information, the most important of which are:

- information about the module itself, which go into the header comments;
- parameter definitions, which are collated to form the preamble. Duplicates must be removed here to avoid errors; and
- the pulse programmes themselves, which are directly concatenated to form the main section.

These, as well as other smaller bits of information (e.g. relevant citations, appropriate processing scripts), are stored within `NOAHModule` objects (an example is provided in listing 4.2). Each distinct module corresponds to one such object. Therefore, if one wants to add a new module to GENESIS, most of the work can be completed by simply defining a new `NOAHModule` object: no changes to the algorithm itself are needed.

To put the epilogue together, the pulse programme constructed so far is scanned for pulse phases, shaped pulses, and all other parameters. Using predefined lookup tables, GENESIS then outputs pulse phase definitions, WaveMaker directives (where appropriate), and comments containing textual descriptions of each parameter. These comments are mostly cosmetic, but are very useful to the user as they are displayed in the `ased` screen when setting up an experiment. Finally, instructions for automatic processing of the NOAH data (explained in § 4.2.1) are added to the bottom, together with the version number and a timestamp (for reproducibility purposes).

```

let shortDescription = `; 13C HSQC`

let preamble = `
"d4      = 0.25s/cnst2"          ; 13C INEPT
; ...
"D[ID]a  = d4-p14/2"           // [ID] is later replaced with the module code
`

let pulprog = `
; 13C-1H HSQC

; INEPT
(p1 ph0):f1
; ...
goscnp ph30 cpd2:f2
50u do:f2
`

const mod = new NOAHModule(
  "C_HSQC",           // internal module code
  "c13",              // module category
  "S",               // single-letter code, Table 4.1
  [],                // relevant citations (if any)
  "noah_hsqc",       // AU programme for processing
  shortDescription,  // short description
  [AF_EDIT],         // available acquisition flags
  preamble,          // preamble text
  pulprog,           // pulse programme text
  1,                 // number of FIDs
  false              // flag for 'parallel' modules
);
export default mod;

```

Listing 4.2: An excerpt of the NOAHModule object for the HSQC module (internal code C_HSQC).

1st:module_c_hsqc

Phase/delay incrementation and looping

Since NOAH experiments are 2D experiments, there is one additional complication: the pulse programme must contain appropriate looping statements, together with pulse phase and delay incrementation, in order to correctly generate the indirect dimension. In many existing NOAH pulse programmes, looping in 2D experiments was written using the equivalent of for loops (listing 4.3, *left*). Although this suffices for the vast majority of supersequences, whenever anything must be incremented in a different way (e.g. for parallel supersequences, or the PSYCHE module which uses a different number of t_1 increments), the nested loop structure must be modified. I

therefore opted to change the structure to use only one loop, and to control the phase and delay incrementation using modular arithmetic (listing 4.3, *right*). The outcome is entirely equivalent, but edge cases can be implemented simply by adding another check on the loop counter L1.

<pre> "l0 = td1/4" 1 ze 3 1m 4 d1 st0 ; ... (pulse sequence goes here) ; in inner loop 1m igrad EA ; HSQC gradients 1m id11 ; COSY t1 30m wr #0 if #0 zd lo to 4 times 2 ; in outer loop 1m ip5*2 ; HSQC 13C 90 1m ip30*2 ; HSQC receiver 1m id0 ; HSQC t1 lo to 3 times l0 end </pre>	<pre> "l0 = td1/2" "l1 = 0" 1 ze 4 d1 st0 ; ... (pulse sequence goes here) ; on every pass 1m iu1 ; loop counter 1m igrad EA ; HSQC gradients 1m id11 ; COSY t1 30m wr #0 if #0 zd ; on every second pass if "l1 % 2 == 0" { 1m ip5*2 ; HSQC 13C 90 1m ip30*2 ; HSQC receiver 1m id0 ; HSQC t1 } lo to 4 times l0 end </pre>
---	---

Listing 4.3: Implementation of phase/delay incrementation and looping in previous NOAH sequences (*left*, using nested loops) and in GENESIS (*right*, using modular arithmetic).

lst:genesis_looping

Parameter standardisation

Each NOAH module contains a number of parameters, including pulse widths, delays, gradient amplitudes, shaped pulse waveforms. Since different modules are stored separately (as different objects), directly concatenating their pulse programmes may lead to conflicting parameter definitions. GENESIS avoids this by maintaining a global table of parameter definitions which are applied to all modules: when new modules are added, they must be checked against this to ensure that there are no inconsistencies.

In general, where possible, these parameters are chosen to be consistent with pulse programmes in the Bruker standard library: thus, for example, P1 is the ^1H 90° pulse width, and CNST2 is the

$^1J_{\text{CH}}$ value used for calculating INEPT delays. This makes it easy to read in parameters either from the *prosol* relation tables in TopSpin, or from other existing parameter sets. Some delays are module-specific and do not need to be reused, and in standard library sequences, are often labelled as DELTA1, DELTA2, and so on. To avoid conflicting definitions and also to improve readability, I rename these such that they include the name of the module: thus, in a ^{13}C HSQC these may be labelled DC_HSQC_1. Here, C_HSQC is the name associated with the NOAHModule object.

If combined with some caution when adding new modules, these measures ensure that *within* a supersequence there are no parameter clashes: we may view this as a *local uniqueness* of parameters. However, the impact of this design choice is even more far-reaching: since parameters are stored globally, they will always have the same value in *all* possible supersequences (or in other words, the parameters are *globally unique*). This makes it exceptionally easy to set up multiple different supersequences in TopSpin: virtually all of the parameter values may simply be copied from a previous NOAH dataset.

One potential issue with this strategy is that TopSpin provides a finite number of named pulse widths (for example). Thus, there are only so many different parameters which can be stored in a global table before running into inevitable conflicts. A workaround would be to sacrifice the global uniqueness of each parameter, and only have it be unique within a given supersequence. Fortunately, this situation has not (yet) surfaced.*

Parameter descriptions

At the epilogue of the pulse programme, extra comments are added for every parameter present in the pulse programme. Most of these are purely textual, and appear in the TopSpin ased parameter setup screen; this naturally helps to make the pulse programmes as easy to use as possible. However, some of these comments have especial meaning: gradient amplitudes and shapes, for example, are specified in a way which allows them to be automatically populated using the gppp Python script in TopSpin. Furthermore, WaveMaker directives are also specified for some shaped pulses, allowing them to be created in an on-the-fly manner using the wwm command. This means that the user (generally) need not separately download and install a set of shaped pulses.

*The number of *pulse phases* in particular, though, is dangerously close to the maximum number of 32. In fact, the global uniqueness criterion is not really important for pulse phases, because—unlike, say, delays—pulse phases are hardcoded in the pulse programme, and cannot be copied from one dataset to another. So, if necessary, I could dispense with the global uniqueness for pulse phases, at the cost of some increased code complexity. I did briefly contemplate this possibility, but since I am at the end of my DPhil and am unlikely to add any new modules soon, this will remain a hypothetical—for now.

Module choice

One final issue which must be overcome is the fact that some NOAH modules may be implemented differently depending on the supersequence which it is being used in. The HMBC module described in § 4.1.3 is one such example: the form of the zz-filter depends on whether the HMBC module must retain $^1\text{H}^{\text{C}}$ and/or $^1\text{H}^{\text{N}}$ magnetisation for subsequent modules. Thus, in the NOAH-2 BS supersequence the zz-HMBC must be used, but in the NOAH-2 SB supersequence the ‘original’ HMBC without a zz-filter is preferable. Since they have different pulse programmes, each of these ‘versions’ of the HMBC are described by *separate* NOAHModule objects.

However, it is unlikely that the majority of users would want to manually configure the supersequence in such detail. Thus, the GENESIS web interface actually hides these different versions from the user, only showing one button labelled ‘HMBC’. Under the hood, the correct version of the HMBC is automatically chosen based on what other modules the user has chosen (fig. 4.7).

./figures/noah/hmbc_flowchart.png

Figure 4.7: Flowchart showing how the correct ‘version’ of the HMBC module is determined when constructing a supersequence using GENESIS. When developer mode is on, the user directly chooses module codes corresponding to each version of the HMBC. When it is off, the appropriate version is chosen based on which other modules are present in the supersequence.

Should the user indeed desire to control the exact module used, the website also offers a ‘de-

veloper mode' switch: turning this on allows the user to directly choose the desired module code. (Enabling developer mode also reveals a handful of extra modules which were used exclusively for my DPhil and are not generally of interest.)

Tests

One risk inherent in any NMR experiment is the possibility of causing spectrometer damage when executing malformed pulse programmes. To minimise the chances of this, each version of GENESIS is checked against a series of automatic tests before being released. The most important tests ensure that each module containing decoupling statements also turn off decoupling immediately after acquisition. On top of this, there are also a series of regression tests where (Some) supersequences are checked against those generated by previous versions: any differences in these are automatically flagged for review.

None of this can actually *stop* wrong pulse programmes from being written. For example, if a module are incorrectly programmed (which is still very easy), then any supersequence containing that module will not be fully functional. However, the inclusion of tests minimises the chance of creating faulty pulse programmes.

It should be mentioned that this is not a *new* problem which GENESIS introduces: errors in pulse programmes can arise equally easily (if not *even more easily*) when they are handwritten. There is no way to really circumvent this, except through careful inspection of the pulse programme prior to execution. The real difference with GENESIS is that users may be more likely to blindly use the pulse programmes it creates, without applying an equal amount of caution. The tests are therefore not meant to ensure perfection, but rather to avoid some of the worst consequences which may surface. Of course, it is also not possible for GENESIS to prevent users from setting up parameters incorrectly (e.g. overly long acquisition times).

Reproducibility

The final section of a GENESIS pulse programme consists of comments intended solely for reproducibility purposes. These comments indicate exactly which NOAHModule objects were used to create the pulse programme (these can be manually entered via developer mode), as well as a GENESIS *version number*. Since GENESIS has been updated with some regularity during my DPhil, each release is assigned a version number, which broadly follows the principles of *semantic versioning*. Old versions of GENESIS may be accessed by navigating to the specific URL <https://nmr-genesis.co.uk/X/Y/Z> for version X.Y.Z. Together, these two pieces of information allow all pulse programmes to be regenerated whenever necessary: this is important for ensuring that the spectra thus acquired are reproducible (as far as possible).

How smart is GENESIS?

Having written several pages of text about the *features* present in GENESIS, it is tempting to think that it is ‘intelligent’ in its design of pulse programmes. At various points in time, extensions to the concept have even been proposed: in GENESIS, the building blocks used for pulse programme construction are NOAH modules, but one could envision breaking up these into the smallest possible units of pulses, delays, gradients, and so on, and using something like GENESIS to construct *arbitrary* pulse programmes. This was even speculatively mentioned in the paper.

However, in truth, GENESIS is a long way from being able to do such things. In particular, it does not have any actual understanding of the Bruker pulse programming syntax: *almost* all of the pulse programme instructions are hardcoded as strings.* Thus, the creation of pulse programmes is not *truly* being done from the ground up: instead of ‘combining pulse sequence elements’, a more accurate description is that the *text* corresponding to different pulse sequence elements is being concatenated. There is actually a substantial amount of brute force involved. In a similar way, it is not possible for the automated tests to really check for ‘correctness’ of the pulse programmes.

Of course, it is hardly a trivial task to write something more sophisticated: I would need to construct abstract representations of each pulse sequence element, and functions which could transform these into actual pulse programme commands. I feel that I would need rather more knowledge in computer science, especially a course on compilers and/or programming language theory, to do this. However, this was something I would have really liked to do had I had more time!

4.2.3 Processing improvements

Finally, I touch on a few small improvements in processing NOAH data: these are not strictly made possible by the GENESIS website, but having a unified source for pulse programmes and processing scripts does make it substantially easier to propagate these developments.

AU processing scripts

When processing NOAH experiments, the first step is to split up the FIDs of different modules into different files: this is done by the `splitx_au` AU programme. However, after that is done, `splitx_au` *also* calls on auxiliary AU programmes to process each of the resulting datasets. Each module is associated with a specific auxiliary AU programme: for example, HSQC data is processed with `noah_hsqc`, COSY data with `noah_cosy`, and so on.

*There are several exceptions where some parameters (for example, loop counters in DIPSI mixing) are dynamically generated, mainly to avoid clashes between different parts of the supersequence.

Previously, these auxiliary AU programmes had to be specified manually using the USERP1 through USERP5 processing parameters, which respectively apply to the first through fifth modules in a supersequence. Although this was a perfectly serviceable setup, I realised that it was a source of annoyance when running multiple different supersequences, as modules would often be processed incorrectly if the processing parameters were inadvertently copied. Even when just running a single supersequence, this was still an extra cognitive load, especially for users who may not have been familiar with NOAH experiments.

Since the pulse programme specifies which modules are run, and the ‘correct’ processing parameters also depend on the modules, it stands to reason that the processing parameters can be encoded in the pulse programme itself. Thus, all GENESIS pulse programmes contain a line near the bottom specifying which AU programmes are to be used for each of the modules present. I also modified the `splitx_au` AU programme to parse the pulse programme for this extra information. Thus, the USERP1 through USERP5 parameters need no longer be specified, as long as a GENESIS pulse programme and a recent version of `splitx_au` are used. These parameters still serve a purpose, though; if they are non-empty, they will override the ‘default’ processing instructions found in the pulse programme. This maintains backwards compatibility with, for example, parameter sets which have been previously saved; it also allows advanced users to customise the processing, if so desired.

Non-uniform sampling

Another small improvement relates to the implementation of non-uniform sampling (NUS) in NOAH supersequences. Because the indirect dimension in NOAH pulse programmes is generated through explicit looping (listing 4.3), instead of the `mc` macro used in most 2D experiments, the standard NUS implementation in TopSpin cannot be used. Instead, one must explicitly define a list of t_1 increments to sample (stored as the `VCLIST` parameter). On top of this, the original NUS implementation⁴⁹ used a Python script (`noah_nus.py`) to modify the NOAH pulse programme such that it only sampled t_1 values from this list. This, however, necessitated storing two copies of the same pulse programme, one with NUS and one without.

There is no way to circumvent the requirement for the `VCLIST` parameter, but in GENESIS pulse programmes, I opted to implement NUS as an acquisition flag which could be toggled. This means that there is no need to store two versions of the same pulse programme, and also makes it easier to seamlessly switch between non-uniform and uniform sampling as desired.

Unfortunately, this change is slightly more problematic than the `splitx_au` change: this new NUS implementation is not backwards-compatible, so requires a new NUS setup script which I have called `noah_nus2.py`. This script cannot be used with old pulse programmes, and the old script cannot be used with GENESIS pulse programmes. Nevertheless, it does represent a real

improvement over the previous implementation: the GENESIS website also helps to make the changeover as smooth as possible.*

4.3 Discussion of individual modules

sec:noah__modules

The GENESIS website makes it possible to easily implement and distribute entirely new modules, as well as updates to old modules: simply changing the underlying `NOAHModule` objects is sufficient to propagate changes to all supersequences generated using those modules. In this section, I discuss a number of new pulse sequence developments made in the course of my DPhil; all of these have been successfully implemented in GENESIS and are available to download.

With regards to sensitivity analyses, since this chapter discusses the design of *individual modules*, I have chosen to focus almost entirely on the SNR factor A : this is an intrinsic property of the module. In contrast, the quantities ρ_t and ε_t depend on the supersequence within which the module is used, and can be improved trivially by adding more modules to the supersequence under consideration. These numbers reflect the utility of the NOAH *technique*, but are not relevant to the individual modules from which they are constructed.

4.3.1 ^{13}C sensitivity-enhanced HSQC

subsec:noah__sehsqc_c

The first new module is the sensitivity-enhanced HSQC (seHSQC) experiment, which provides up to $2\times$ increased SNR over a standard (echo–antiecho) HSQC.[†] In the original version of the seHSQC (fig. 4.8a), developed by Cavanagh, Rance, and Kay (‘CRK’),^{53,54} this is accomplished through the so-called *preservation of equivalent pathways* (PEP) technique.⁵⁵

Just like in a standard HSQC, the experiment begins with an INEPT block and t_1 evolution. At the end of t_1 , there are two terms which are cosine- and sine-modulated with respect to Ω_S . In the standard HSQC, only the $2I_zS_y$ term is returned into observable ^1H magnetisation by the reverse INEPT block (see § 1.4.4). In contrast, the PEP block transfers *both* terms back to ^1H and subsequently detects both. Specifically, in the echo experiment it accomplishes the transfer $2I_zS_y \rightarrow I_y$ and $2I_zS_x \rightarrow I_x$, meaning that the density operator at the end of t_1

$$-2I_zS_y \cos(\Omega_S t_1) - 2I_zS_x \sin(\Omega_S t_1) \quad (4.6) \quad \text{\{eq:sehsqc_t1_modulati$$

*That said, there were still some bugs in the new NUS implementation right up until August 2022, so this change was not as smooth-sailing as I had hoped for.

[†]Since a States HSQC has $\sqrt{2}$ times the SNR of an EA HSQC (as shown in fig. 1.8), this also means that the seHSQC has a $\sqrt{2}$ SNR improvement over a States HSQC. The literature can be somewhat confusing on this point: sometimes the gain in signal is even conflated with the gain in SNR. The clearest exposition I have found is that provided by Kontaxis et al.⁵²

./figures/pp/sehsqc/all_po.png

Figure 4.8: Sensitivity-enhanced HSQC sequences discussed in this section, along with product operator analysis. This analysis is provided only for the first step of the phase cycle, and assumes an IS spin pair with $\Delta' = 1/(4 \cdot {}^1J_{CH})$. ‘ $\cos {}^1H^C$ ’ refers to the component of the ${}^1H^C$ magnetisation which is cosine-modulated during t_1 . (a) Cavanagh–Rance–Kay seHSQC. (b) NOAH seHSQC1 module. (c) NOAH seHSQC2 module. Phase cycling is performed with $\phi_1 = (x, -x)$, $\phi_2 = (x, x, -x, -x)$, and $\phi_{rec} = (x, -x, -x, x)$. The delay Δ is set to $1/(4 \cdot {}^1J_{CH})$; see the text for a discussion of Δ' . The pulses marked with a phase of $\pm y$ are applied with a phase of y in the echo experiment and $-y$ in the antiecho. Gradient amplitudes are $(g_1, g_2, g'_2, g_3, g_4) = (70\%, \pm 35.2\%, \pm 17.6\%, 11\%, -5\%)$.

is transformed into

$$-I_y \cos(\Omega_S t_1) - I_x \sin(\Omega_S t_1) \quad (4.7) \quad \text{{eq:sehsqc_before_dete}}$$

just prior to acquisition. During the FID, only the -1 -coherence component is detected:

$$\frac{1}{2i} L_- \cos(\Omega_S t_1) - \frac{1}{2} L_- \sin(\Omega_S t_1) = \frac{1}{2i} L_- \exp(-i\Omega_S t_1), \quad (4.8) \quad \text{{eq:sehsqc_detection_m}}$$

yielding a signal of

$$\frac{1}{2i} \exp(-i\Omega_S t_1) \exp(i\Omega_I t_2), \quad (4.9) \quad \text{{eq:s_echo_sehsqc}}$$

which has a $2\times$ larger amplitude than the original EA HSQC (eq. (1.96)). The antiecho experiment can be similarly analysed. Since the seHSQC has the same noise level as in an EA HSQC, this also corresponds to a $2\times$ increase in SNR.

It should, however, be noted that the PEP transfer is only fully attained for IS spin pairs if the delay Δ' is set to $1/(4 \cdot {}^1J_{CH})$. For I_2S or I_3S spin systems, no gain in sensitivity is accomplished with this setting of $\Delta' = 1/(4 \cdot {}^1J_{CH})$. It is more common, therefore, to shorten Δ' to $1/(8 \cdot {}^1J_{CH})$: this sacrifices some transfer efficiency for IS systems, but allows for some sensitivity enhancement for I_2S and I_3S systems (table 4.3). In this work, all experiments were run assuming a value of 145 Hz for ${}^1J_{CH}$.

Spin system	Theoretical sensitivity enhancement		
	$\Delta' = 1/(4 \cdot {}^1J_{CH})$	$\Delta' = 1/(8 \cdot {}^1J_{CH})$	$\Delta' = 1/(12 \cdot {}^1J_{CH})$
IS	2	1.71	1.5
I_2S	1	1.41	1.37
I_3S	1	1.21	1.25

Table 4.3: Theoretical sensitivity enhancements for IS , I_2S , and I_3S spin systems in the seHSQC, as a function of the delay Δ' . The values are taken from Schleucher et al.⁵⁶

NOAH seHSQC versions

Just like the original EA HSQC (fig. 1.7), the CRK seHSQC must be modified in order to be compatible with NOAH supersequences. In particular, the CTP gradients in the CRK seHSQC dephase the bulk ${}^1H^C$ magnetisation pool: we would very much like it to return that to $+z$ instead, so that it can be sampled in later homonuclear modules (or, indeed, a HMBC module). This experiment is more tricky to adapt than the HSQC, because there are *three* different magnetisation components to juggle: the cosine-modulated ${}^1H^C$, sine-modulated ${}^1H^C$, and ${}^1H^C$. Nevertheless, there are at least two ways of doing so; these two modified modules are labelled seHSQC1 and seHSQC2 respectively.

The seHSQC1 module (fig. 4.8b) was developed by me.* It retains the same general structure of the CRK seHSQC up until t_1 , but immediately after t_1 a composite ^1H pulse is used to effect the transformations

$$I_z \rightarrow I_y; \quad I_y \rightarrow I_x, \quad (4.10) \quad \{\text{eq:sehsqc1_dp}\}$$

where the former is required for the $^1\text{H}^{\text{C}}$ pool and the latter for $^1\text{H}^{\text{C}}$. This has the effect of storing the sine-modulated term as $2I_zS_z$ magnetisation for one spin echo (as opposed to the CRK seHSQC, which stores cosine-modulated term as I_z). At the beginning of the final spin echo (containing the rephasing gradient), this is transformed into antiphase magnetisation of the form $2I_xS_z$; thus, this spin echo must be lengthened to a total duration of 2Δ in order to fully refocus $^1J_{\text{CH}}$. The final modification involves the addition of an extra gradient immediately before to t_1 : this ensures that the bulk $^1\text{H}^{\text{C}}$ magnetisation is not dephased, just like in the NOAH HSQC module (fig. 4.2a).

The seHSQC2 module (fig. 4.8c), on the other hand, was initially reported by Hansen et al.⁵⁷ In this pulse sequence, the initial ^1H 90° excitation pulse is replaced with a zz isotope-selective pulse element (ZIP element), which is very similar to the zz -filter but has different pulse phases. This acts as a 90°_x pulse on the $^1\text{H}^{\text{C}}$ magnetisation pool and thus ultimately leads to the same signals being detected (save for a trivial 180° phase shift). However, on $^1\text{H}^{\text{C}}$ magnetisation, the ZIP element acts as a 90°_y pulse; it turns out that this modification alone is sufficient to return the bulk $^1\text{H}^{\text{C}}$ magnetisation to $+z$ at the end of the sequence. The ZIP element therefore represents an isotope-specific rotation on ^1H spins, where the rotation axis depends on whether it is coupled to ^{13}C or not.

./figures/pp/sehsqc/grad_schemes.png

Figure 4.9: Comparison of CTP gradient schemes in seHSQC2 module. (a) As reported in Hansen et al.⁵⁷ g_0 is a purge gradient with arbitrary amplitude; the amplitude of the final CTP gradient must be halved. (b) The version used in this work (corresponding to fig. 4.8c).

In my work, I made one change to the experiment, namely the addition of an extra gradient echo prior to t_1 (thus leading to a symmetric gradient scheme similar to that in seHSQC1). Instead of this, the original paper had in fact inserted a purge gradient between the ^1H and ^{13}C 90° pulses just after the INEPT spin echo (fig. 4.9). The scheme I used leads to similar results, but has one

*Through a great deal of trial and error, and certainly *not* intelligent design.

advantage in that it allows the amplitude of the final CTP gradient (g_2 in fig. 4.8) to be twice as large: this is particularly relevant to ^{15}N experiments, as will be discussed in § 4.3.2.

./figures/noah/sehsqc_comp.png

Figure 4.10: Sensitivities of seHSQC and CLIP-COSY modules in the NOAH-2 S^+C^c supersequences (run using $\Delta' = 1/(8 \cdot J_{\text{CH}})$). Intensities are reported relative to the corresponding peaks in a NOAH-2 SC^c supersequence; HSQC peaks are further broken down by their multiplicity. Each dot represents one peak; the solid lines as well as the numbers at the bottom of each plot represent averages over all peaks. (a) Using the CRK seHSQC. (b) Using the seHSQC1 module. (c) Using the seHSQC2 module. Data code: 7A-201115.

The primary consideration when evaluating the different seHSQC versions in fig. 4.8 is naturally sensitivity. Figure 4.10 compares the sensitivities of the various possible NOAH-2 S^+C^c supersequence against a NOAH-2 SC^c experiment. As can be seen, all three seHSQC implementations yield improvements in the sensitivities of CH peaks: the original CRK seHSQC has the largest effect here, followed by seHSQC2 and seHSQC1. For CH_2 and CH_3 peaks, the CRK seHSQC and seHSQC2 perform better than the standard HSQC, but the average sensitivities in seHSQC1 have dipped slightly below. This is not entirely surprising in light of the discussion in § 4.1.1: the modified seHSQC1 and seHSQC2 sequences are expected to have lower sensitivities than the original experiment from which they are derived. In this case, it appears that the modifications made to the seHSQC1 sequence have caused sensitivity losses which outweigh the benefits of using a sensitivity-enhanced experiment.

In the context of a NOAH supersequence, it is also important to consider how well each module preserves $^1\text{H}^{13}\text{C}$ magnetisation for subsequent homonuclear module(s). In fig. 4.10, the CLIP-COSY module is used as the ‘reporter’ module, but the conclusions drawn here are applicable to *any* homonuclear module (or HMBC). The CRK seHSQC naturally does poorly in this respect, as it dephases the bulk magnetisation: this leads to almost an order-of-magnitude sensitivity loss in the CLIP-COSY. Both the other NOAH seHSQC modules, however, perform almost identically to the original HSQC module, as expected from the product operator analysis in

fig. 4.8.

From fig. 4.10, we can draw some very simple conclusions: if the seHSQC is to be used at (or near) the *beginning* of a NOAH supersequence, where it needs to preserve $^1\text{H}^1\text{C}$ magnetisation, then the seHSQC2 module is the best choice. On the other hand, if the seHSQC module is placed at the *end* (say in a NOAH-2 BS^+ supersequence), then the CRK seHSQC is optimal. This logic is encoded in GENESIS.

COSY-type artefacts

One (minor) way in which the seHSQC1 module outperforms seHSQC2 is in the suppression of COSY-type artefacts in the seHSQC spectrum.⁵⁸ These arise due to evolution of $^nJ_{\text{HH}}$ during the second-last spin echo of the CRK seHSQC. Specifically, if we assume the presence of a separate ^1H spin K which is coupled to spin I , the sine-modulated $2I_yS_z$ term can evolve under both $^1J_{IS}$ and $^nJ_{IK}$ into $2I_yK_z$, and the last ^1H 90° pulse transfers this coherence to the spin K . This leads to peaks correlating spin S with K . This is also true of the seHSQC2 module, as the product operator analysis for the CRK seHSQC is entirely applicable to it.

However, for the seHSQC1 module, the corresponding term giving rise to these artefacts would be the cosine-modulated I_x term (at the beginning of the second-last spin echo). During this spin echo, this can again evolve under both J-couplings into $4I_yK_zS_z$, and the final 90° pulse would transform this to $-4I_zK_yS_z$. However, crucially, this term is antiphase with respect to the heteronucleus S : therefore, when decoupling is applied during acquisition, this term should not be observed. This analysis can be verified experimentally by inspection of the seHSQC spectra thus obtained. The COSY-type artefacts, labelled with red boxes in the seHSQC2 spectrum (fig. 4.11b), are largely absent in the seHSQC1 spectrum (fig. 4.11a). Some artefacts still remain, which perhaps arise due to pulse imperfections (or perhaps more complicated spin systems than the three-spin system considered here; I did not analyse this in any further detail).

./figures/noah/sehsqc_cosy_arts.png

Figure 4.11: Comparison of COSY-type artefacts in NOAH seHSQC modules. (a) seHSQC1. (b) seHSQC2. The artefacts are highlighted in red boxes. Data code: 7A-201115.

Wing artefacts

One point worth considering is whether the extra gradient in the seHSQC2 module is truly needed. In the HSQC and seHSQC1 modules, the bulk magnetisation is placed along the transverse axis during t_1 ; therefore, if a pair of symmetric gradients are not used, this magnetisation will be dephased (as in the CRK seHSQC). However, in the seHSQC2 module, the bulk magnetisation is longitudinal, which suggests that this gradient is not necessary.

This gradient can indeed be removed in the seHSQC2 module, and doing so does not lead to any poorer preservation of $^1\text{H}^1\text{C}$ magnetisation. However, the omission of this gradient leads to artefacts in the CLIP-COSY spectrum, which I term ‘wing artefacts’ because of the way they flank peaks in the CLIP-COSY (fig. 4.12). These artefacts can most clearly be seen in the diagonal peaks of methyl groups, but are present across the entire spectrum.

./figures/noah/sehsqc_wing_arts.png

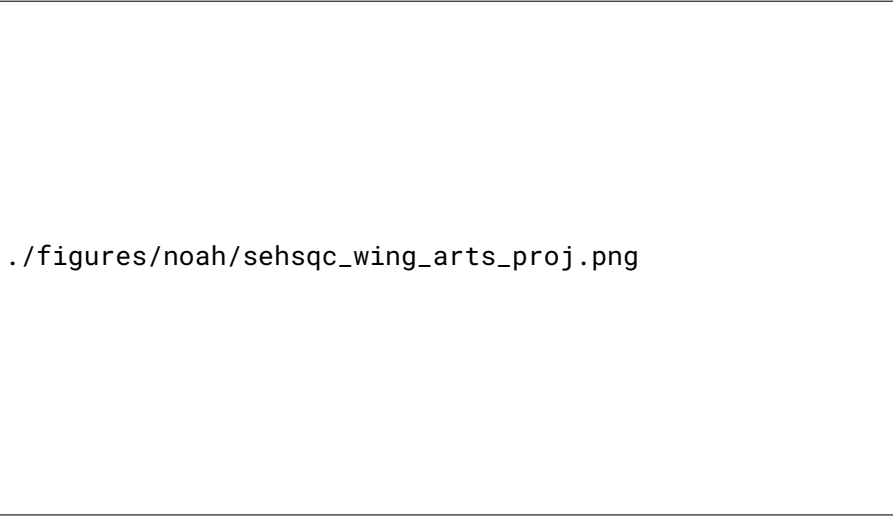
Figure 4.12: Wing artefacts in CLIP-COSY spectra, taken from NOAH-2 S^+C^c super-sequences. (a) Using the seHSQC2 module as shown in fig. 4.8c. (b) Using a modified seHSQC2 module where the gradient echo just before t_1 is removed. The wing artefacts flanking the two rightmost diagonal peaks can be clearly seen; the boxed artefacts are studied further in fig. 4.13. Data code: 7A-201115.

A clue as to their origin is provided by the characteristic frequencies of the artefacts:

$$\left(\Omega_1, \Omega_2 = \Omega_I \pm \frac{\Omega_I \cdot [t_{1,\text{HSQC}}/2]}{t_{1,\text{COSY}}}, \Omega_I \right) \quad (4.11) \quad \text{(eq:wing_artefact_freq)}$$

where $t_{1,X}$ refers to the value of t_1 in experiment X (it does not matter which increment is used, because the ratio of t_1 in the fraction above is constant). In accordance with this, when the seHSQC indirect-dimension spectral width is reduced, the artefacts are displaced outwards (fig. 4.13e). This suggests that these artefacts arise from $^1\text{H}^1\text{C}$ magnetisation which is frequency-labelled in two different t_1 periods: specifically, it evolves once during *half* of the seHSQC t_1 period, and then again during the CLIP-COSY t_1 period. In fact, it is necessary to apply CTP gradients on both sides of t_1 in order to suppress evolution of this stray magnetisation during

both halves: if either or both of the gradients are removed, the artefacts are present (figs. 4.13a to 4.13d).



./figures/noah/sehsqc_wing_arts_proj.png

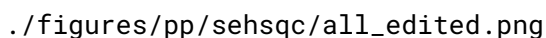
Figure 4.13: A closer look at wing artefacts in CLIP-COSY spectra, taken from NOAH-2 S^+C^c supersequences with various modifications made to the seHSQC2 module. The spectra being plotted are 1D slices through $F_2 = 0.67$ ppm of the 2D CLIP-COSY spectrum; this corresponds to the boxed region in fig. 4.12b. (a) Using the default seHSQC2 module, with one gradient before and one after t_1 . (b) The same as (a), but with the gradient before t_1 turned off (the spin echo is still present, but the gradient intensity is set to 0). (c) The same as (a), but with the gradient after t_1 turned off. (d) The same as (a), but with both gradients turned off. (e) The same as (b), but with the seHSQC spectral width reduced by a factor of 4. *Data code:* 7A-201115.

These wing artefacts are unique to fast-pulsing experiments such as NOAH supersequences: in a typical 2D experiment, these are less likely to arise because of the long(er) recovery delays between data acquisition periods. In the sections which follow, we will see these surface repeatedly. Fortunately, it proves to be relatively easy to suppress them through the judicious use of gradients.

Multiplicity editing

Multiplicity editing is reasonably easy to include in all of the seHSQC sequences above. It suffices to add a spin echo of total duration $4\Delta = 1/{}^1J_{CH}$ just after t_1 , while also making sure to change some pulse phases to account for the extra 1H 180° pulse (fig. 4.14).

The inclusion of editing does not make a substantial difference in the sensitivity comparisons (fig. 4.15). However, it is interesting to note that the edited seHSQC2 in fact performs *better* than the edited HSQC in terms of preserving bulk magnetisation, as evidenced by the larger COSY intensities in fig. 4.15c. This can be explained by the fact that in the editing period of the HSQC experiment (and seHSQC1), the bulk magnetisation is placed in the transverse plane.



./figures/pp/sehsqc/all_edited.png

Figure 4.14: Multiplicity-edited NOAH seHSQC modules. (a) Edited seHSQC1. (b) Edited seHSQC2.



./figures/noah/sehsqc_comp_edited.png

Figure 4.15: Sensitivity comparisons for multiplicity-edited seHSQC in NOAH-2 S^+C^c supersequences. The delay Δ' was set to $1/(8 \cdot J_{CH})$. (a) Using the edited CRK seHSQC. (b) Using the edited seHSQC1 module. (c) Using the edited seHSQC2 module. Data code: 7A-201115.

The evolution of homonuclear couplings will thus lead to a small loss in the amount of $^1H^1C$ magnetisation preserved. In the seHSQC2 sequence, the bulk magnetisation is longitudinal during the editing period, so does not evolve under J_{HH} .

Choice of Δ'

As discussed previously, there are several possible values for the delay Δ' . I thus also investigated the possibility of setting $\Delta' = 1/(4 \cdot {}^1J_{\text{CH}})$. The corresponding sensitivity comparisons are shown in fig. 4.16.

./figures/noah/sehsqc_1over4j.png

Figure 4.16: Sensitivity comparisons with Δ' set to $1/(4 \cdot {}^1J_{\text{CH}})$. Multiplicity editing was not used. (a) Using the CRK seHSQC. (b) Using the seHSQC1 module. (c) Using the seHSQC2 module. Data code: 7A-201115.

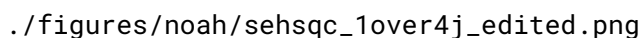
As can be appreciated, the sensitivity boosts obtained for CH groups is higher than in the corresponding spectra with $\Delta' = 1/(8 \cdot {}^1J_{\text{CH}})$ (fig. 4.10). However, in this case, there is a small sensitivity loss for CH_2 and CH_3 groups as compared to the original HSQC (which is consistent with previous studies⁵⁶). For CH_3 groups this is unlikely to be of any consequence, but particularly for diastereotopic CH_2 groups this may not be desirable.

It is interesting to note that the performance of the seHSQC1 module is much closer to that of the seHSQC2 here. The fact that seHSQC1 performs worse with the reduced value of $\Delta' = 1/(8 \cdot {}^1J_{\text{CH}})$ suggests that there are some inefficiencies in this section of the pulse sequence; however, there is no immediate explanation for this in the product operators (the relevant terms in the seHSQC1 are entirely similar to that in the CRK, save for a minus sign).

The conclusions drawn are entirely similar when multiplicity editing is enabled (fig. 4.17), so will not be further discussed.

Optimal control for seHSQC1

One unresolved question is why the seHSQC1 module has a lower sensitivity than the seHSQC2, despite being shorter and containing fewer 180° pulses. There is also nothing in the product operator analysis to explain why this should be the case. One remaining possibility is the presence



./figures/noah/sehsqc_1over4j_edited.png

Figure 4.17: Sensitivity comparisons with Δ' set to $1/(4 \cdot J_{\text{CH}})$ and with multiplicity editing. (a) Using the edited CRK seHSQC. (b) Using the edited seHSQC1 module. (c) Using the edited seHSQC2 module. Data code: 7A-201115.

of some non-ideality in the pulses themselves, and the composite ^1H pulse is an obvious candidate for investigation.*

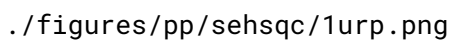
In order to investigate the extent to which this was responsible, I sought to use optimal control theory to develop a *universal rotation pulse* (URP) which could replace this composite pulse. Such a pulse must accomplish the transformations in eq. (4.10), namely $z \rightarrow y$ and $y \rightarrow x$.[†] This optimisation was performed using an interior-point algorithm (the default in Matlab `fmincon`) and the ESCALADE method⁶⁰ for the calculation of analytic derivatives. Pulse fidelity was calculated as an average over 51 ^1H spins, evenly distributed across a frequency range of 11 kHz (corresponding to 15.7 ppm at 700 MHz); the duration of the pulse was fixed at 200 μs , and 200 pulse points were used.

The ^{13}C 90° pulse which is simultaneously applied during the pulse sequence was not optimised together with this: because of the longer duration of the ^1H URP, the sequence must be modified slightly (fig. 4.18). In particular, the delays α and β must be chosen in order to satisfy the relations $2\varepsilon = \alpha + \beta$ (to ensure $^1\text{H}^{13}\text{C}$ magnetisation is refocused), and $\alpha = \beta + \tau$ (to ensure that for $^1\text{H}^{\text{C}}$ magnetisation, the ^{13}C chemical shift evolves for a total duration of t_1).

This optimisation process yielded a pulse with 99.99% fidelity: the (theoretical) performance of this pulse on z - and y -magnetisation is shown in fig. 4.19. However, when tested in the actual

*The concept of a *composite pulse*⁵⁹ is usually associated with greater efficiency / uniformity, but here I have used the term to loosely refer to a consecutive series of pulses.

[†]The effect of this pulse on x -magnetisation is not important for the seHSQC1, but is in fact fully determined by these two constraints: $U I_x U^\dagger = -iU(I_y I_z - I_z I_y)U^\dagger = -i(U I_y U^\dagger U I_z U^\dagger - U I_z U^\dagger U I_y U^\dagger) = -i(I_x I_y - I_y I_x) = I_z$. This reveals a geometric interpretation of this pulse element: it is actually a 120° rotation about the vector (1, 1, 1), which is closely related to the C_3 symmetry operation in the octahedral point group.



./figures/pp/sehsqc/1urp.png

fig:sehsqc1_urp

Figure 4.18: seHSQC1 pulse sequence using a ^1H URP in place of the double- 90° composite pulse. τ is the difference in duration between the URP and the ^{13}C 90° hard pulse. Delays are set as: $\alpha = \varepsilon + \tau/2$; $\beta = \varepsilon - \tau/2$.



./figures/noah/spv1_urp_magn.png

f 4.19: spv1_urp_magn.png

Figure 4.19: Simulated performance of URP used for seHSQC1 module on z - and y -magnetisation. The pulse fidelity was 99.99%. (a)–(e) Using z -magnetisation as input: the plots respectively show the amount of x -magnetisation, y -magnetisation, z -magnetisation, transverse magnetisation ($M_{xy} = \sqrt{M_x^2 + M_y^2}$), and the phase of the transverse magnetisation generated, as a function of offset frequency. (f)–(j) The same, but using y -magnetisation as input.

seHSQC1 experiment, this failed to yield any substantial difference compared to the original double 90° pulse (figs. 4.20a and 4.20b). Importantly, the performance still falls below that of the seHSQC2 module (fig. 4.20c). The reason for the poorer sensitivity therefore likely lies elsewhere.

./figures/noah/sehsqc1_urp_sens.png

Figure 4.20: Sensitivity comparisons using the seHSQC1 URP. Δ' was set to $1/(8 \cdot {}^1J_{\text{CH}})$; no multiplicity editing was used. Note that a different dataset was used for this figure and fig. 4.10, so the numbers are very slightly different. (a) Original seHSQC1 module with double ${}^1\text{H}$ 90° pulse. (b) seHSQC1 using the optimised URP shown in fig. 4.19. (c) seHSQC2 module for comparison. *Data code:* 7A-220110.

BIG-BIRD versus ZIP

The final point in this section pertains to the implementation of the seHSQC2 module. As it stands, the isotope-specific rotation element placed at the start of the module is the ZIP element: its role is to effect 90° rotations with different phases on the ${}^1\text{H}^{\text{C}}$ and ${}^1\text{H}^{\text{I}^{\text{C}}}$ magnetisation pools. However, such pulse elements have been known for a long time: these include TANGO,⁶¹ BANGO,⁶² BIRD,^{63–65} BIG-BIRD,⁶⁶ and TIG-BIRD.⁶⁷ In particular, the BIG-BIRD element can be designed to accomplish the same overall effect as the ZIP element. For the seHSQC2 without multiplicity editing, we can therefore replace the ZIP element with

$$45_{45}^\circ({}^1\text{H})-2\Delta-180^\circ({}^1\text{H}, {}^{13}\text{C})-2\Delta-45_{225}^\circ({}^1\text{H}), \quad (4.12) \quad \text{\small \{eq:big_bird_unedited\}}$$

where β_ϕ represents a hard pulse with flip angle β and phase ϕ . For the edited seHSQC, the phases must be altered slightly:

$$45_{315}^\circ({}^1\text{H})-2\Delta-180^\circ({}^1\text{H}, {}^{13}\text{C})-2\Delta-45_{135}^\circ({}^1\text{H}). \quad (4.13) \quad \text{\small \{eq:big_bird_edited\}}$$

This BIG-BIRD version of the seHSQC2 was also evaluated. However, its performance in all respects was not as good as the ZIP version: both the seHSQC sensitivity itself, as well as the sensitivity of the later CLIP-COSY, were lower when the BIG-BIRD element was used.



./figures/noah/sehsqc_bigbird.png

Figure 4.21: Sensitivity comparisons of BIG-BIRD and ZIP pulse elements in seHSQC2 module. The reference dataset being compared against is still the NOAH-2 SC^c (but with editing in (c) and (d). The delay Δ' was set to $1/(8 \cdot {}^1J_{\text{CH}})$. (a) Unedited seHSQC2 using BIG-BIRD. (b) Unedited seHSQC2 using ZIP. (c) Edited seHSQC2 using BIG-BIRD. (d) Edited seHSQC2 using ZIP. Data code: 7A-201115.

4.3.2 ¹⁵N HMQC

In § 4.3.3, I will discuss how the sensitivity-enhanced HSQC modules developed above may be adapted into ¹H–¹⁵N experiments. However, before that, I make a slight detour to cover the ¹⁵N HMQC experiment, which (up until my DPhil) was the experiment of choice for detecting one-bond ¹H–¹⁵N correlations.

CTP gradient scheme

The HMQC module is based on the ASAP-HMQC reported by Kupče and Freeman,¹³ which used a symmetric gradient scheme similar to that in the seHSQC modules previously described (fig. 4.22a). However, in the NOAH module,³² bipolar gradient pulse pairs were placed before and

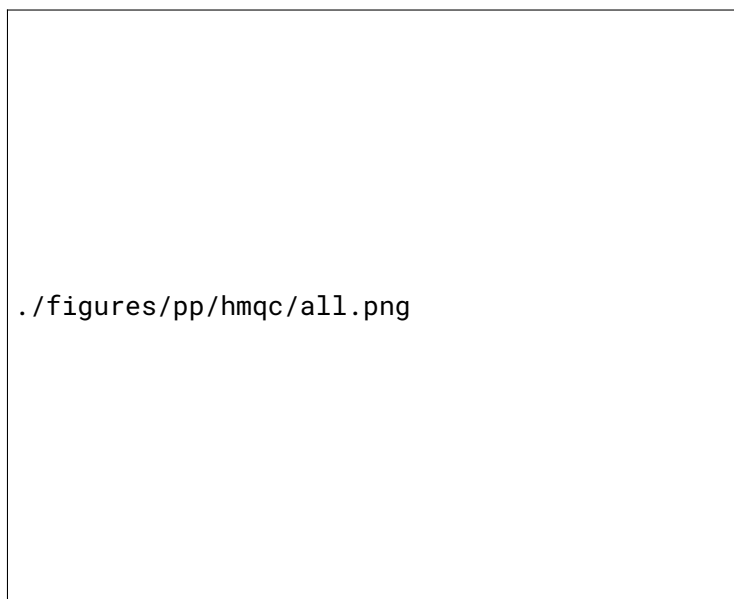


Figure 4.22: (a) With two encoding gradients around t_1 . (b) With four encoding gradients around t_1 . Phase cycling is performed with $\phi_1 = (x, -x)$, $\phi_2 = (x, x, -x, -x)$, and $\phi_{\text{rec}} = (x, -x, -x, x)$. The delay Δ is set to $1/(4 \cdot {}^1J_{\text{NH}})$. Gradient amplitudes are: $g_1 = 80\%$; $g_2 = \pm 32.4\%$; $g'_2 = g_2/2$.

after t_1 (fig. 4.22b). This was likely implemented in order to allow the final gradient, g_2 , to have as large an amplitude as possible. In heteronuclear experiments, this final gradient is particularly important for dephasing bulk magnetisation which is transverse just prior to detection (due to pulse imperfections or relaxation). If this gradient is too weak, this unwanted magnetisation will be incompletely dephased, leading to artefacts in the resulting spectrum.

Strategies to maximise this gradient amplitude are particularly crucial in ${}^1\text{H}$ - ${}^{15}\text{N}$ experiments (as compared to ${}^1\text{H}$ - ${}^{13}\text{C}$ experiments) for two reasons. Firstly, the natural abundance of ${}^{15}\text{N}$ (0.36%) is even smaller than ${}^{13}\text{C}$ (1.1%), meaning that better suppression must be achieved in order for the artefacts to not obscure the signal. Secondly, the gyromagnetic ratio of ${}^{15}\text{N}$ is also smaller: thus, since $g_2/g_1 \propto \gamma_{\text{N}}/\gamma_{\text{H}}$, an unmodified pulse sequence will naturally have a smaller g_2 .

In this respect, the four-gradient scheme in fig. 4.22b is superior to the two-gradient scheme, because the gradient g_2 will have an amplitude of $4\gamma_{\text{N}}g_1/\gamma_{\text{H}}$. However, when used in a NOAH supersequence, this leads to wing artefacts in downstream modules, since bulk ${}^1\text{H}$ - ${}^{15}\text{N}$ magnetisation effectively does not experience any coherence order selection during t_1 . This motivates a return to the two-gradient scheme of fig. 4.22a. To compensate for the fact that the decoding gradient g'_2 has half of the amplitude of g_2 , all CTP gradients were instead *lengthened* from their usual duration of 1 ms to 2.5 ms. This ensures that any stray transverse bulk magnetisation at the end of the HMQC module is effectively dephased.

The HMQC spectra thus obtained are shown in fig. 4.23. These, and all other ^1H - ^{15}N spectra in this chapter, were acquired assuming a $^1J_{\text{NH}}$ value of 90 Hz. The first column shows the spectra obtained with the original four-gradient scheme: although the artefacts at 2.2 ppm are reasonably well-suppressed in the HMQC module (fig. 4.23b), the CLIP-COSY spectrum clearly has a set of wing artefacts (fig. 4.23c). (Note that the wing artefacts occur at different frequencies compared to the ^{13}C seHSQC case, because the t_1 increment in the ^{15}N HMQC module is different.)

The second column shows what happens when the two-gradient scheme is adopted without changing the gradient duration. Although the CLIP-COSY wing artefacts disappear (fig. 4.23f), the HMQC artefacts are over twice as intense (fig. 4.23e), and (in this case) have comparable intensity to the desired peaks.

By using the two-gradient scheme and increasing the gradient duration to 2.5 ms, we obtain the best of both worlds: the HMQC artefacts are well-suppressed (fig. 4.23h, in fact even better than in the original spectrum), and the CLIP-COSY is free of wing artefacts (fig. 4.23i). The only drawback is a slight loss in signal intensity in the HMQC, which arises due to diffusion and relaxation during the longer pulse sequence. However, this decrease is only on the order of 5% (for this particular case), which is a totally acceptable price to pay in return for the improved spectral quality.

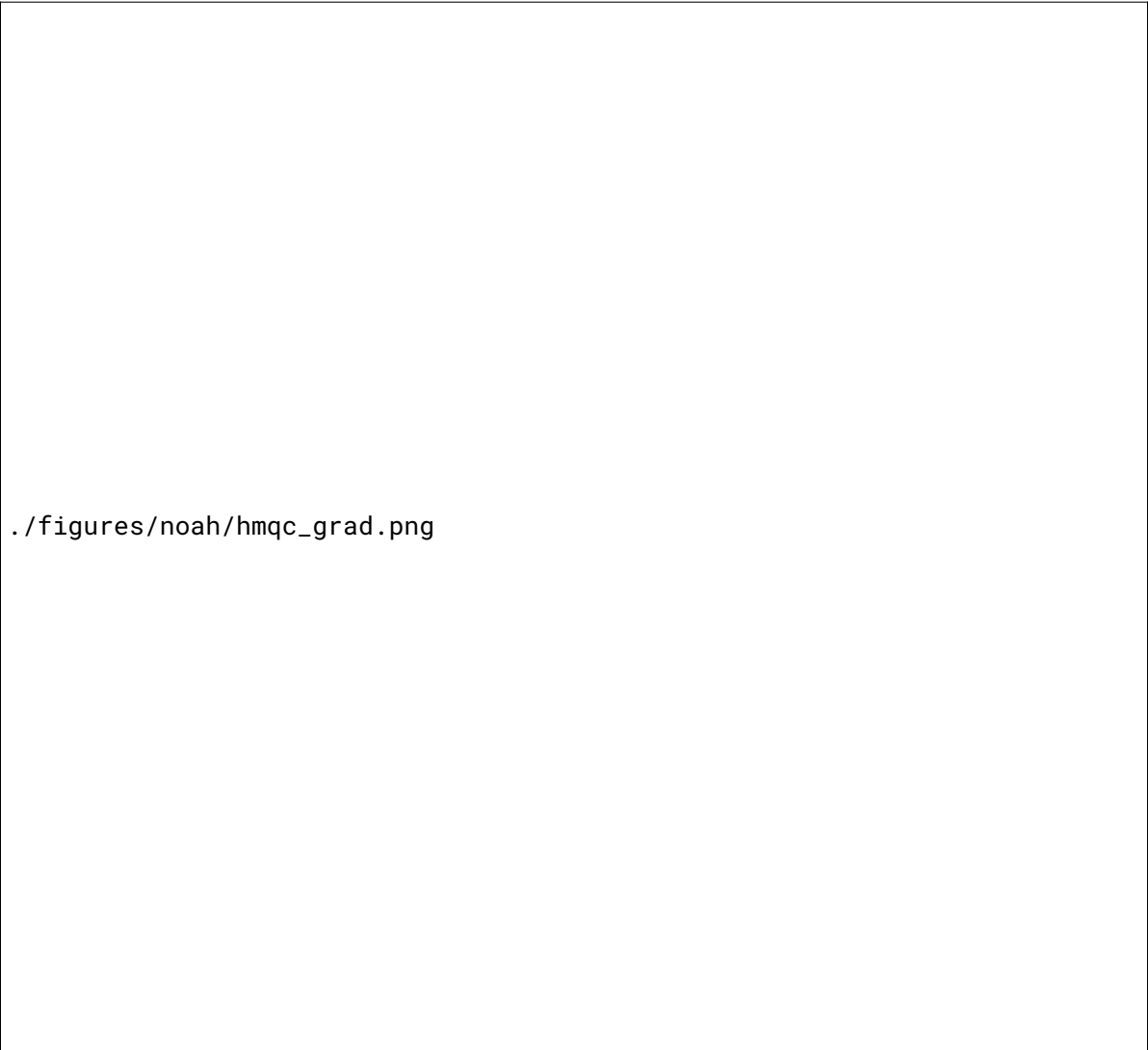
It is of some interest to check whether such a long gradient is truly required. I therefore ran the two-gradient HMQC experiment with a series of gradient durations from 1 ms to 2.5 ms; the signal and artefact intensities in each of these experiments are plotted in fig. 4.24. Generally, there is little variation in the intensities of the two desired peaks. The artefact intensity is more erratic, which possibly reflects the fact that gradient dephasing varies sinusoidally with the gradient duration τ due to the spatial integral

$$\frac{1}{L} \int_{-L/2}^{L/2} \exp(i\gamma G z \tau) dz = \frac{\sin(\gamma G L \tau / 2)}{\gamma G L \tau / 2}, \quad (4.14) \quad \text{(eq:gradient_dephasing)}$$

where L is the sample length and G the gradient amplitude (see also eq. (1.93)). Nevertheless, there is a clear decrease in the signal intensity as the gradient duration increases, which (at least in these datasets) is greatest with 2.5 ms gradients. Since the signal intensity is not affected much, I deemed this to be a perfectly suitable value.

***k*- and SW-scaling**

^1H - ^{15}N spectra of small molecules are often relatively sparse in the indirect dimension, and do not typically need to be acquired with the same resolution as a ^1H - ^{13}C experiment. However, if these experiments were to be combined together within a supersequence, it is not ordinarily possible to toggle the resolution of each module individually. One way of circumventing this



./figures/noah/hmqc_grad.png

Figure 4.23: Comparison of HMQC and CLIP-COSY spectra obtained from NOAH-3 $M_N S^+ C^c$ supersequences, acquired using different HMQC gradient schemes. In the first row, the HMQC spectrum itself is shown. In the second row, the positive projection of the HMQC spectrum onto the F_2 axis is shown; the numbers indicate peak intensities with respect to the reference dataset (the left column). The asterisks indicate artefacts arising from bulk magnetisation which is not sufficiently dephased by the final gradient. In the third row, (an inset of) the CLIP-COSY spectrum is shown. (a)–(c) Using the four-gradient scheme of fig. 4.22b, with 1 ms gradients. (d)–(f) Using the two-gradient scheme of fig. 4.22a, with 1 ms gradients. (g)–(i) Using the two-gradient scheme of fig. 4.22a, with 2.5 ms gradients. *Data code:* 7Z-200926.

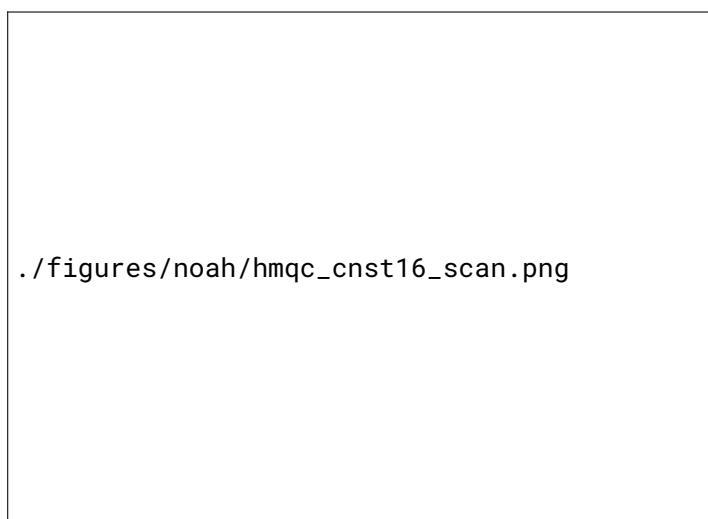


fig:hmqc_cnst16

Figure 4.24: Variation of HMQC signal and artefact intensity with CTP gradient duration, as measured by (absolute) peak heights in the positive F_2 projection. Data code: 7Z-200926.

issue is to decrease the frequency with which the ^{15}N t_1 duration is incremented in the pulse programme: this was first proposed by Parella et al. in the context of time-shared NMR,^{27,68} and in this thesis is called ‘ k -scaling’. This means that each t_1 increment is acquired several times before t_1 is incremented; effectively leading to k times fewer t_1 increments, but with each increment having k times the number of scans (after the data have been combined). An alternative is to simply increase the spectral width of the ^{15}N module (which is encoded as the CNST40 parameter in GENESIS).

Figure 4.25 illustrates all of these possibilities in detail. In a ‘typical’ NOAH supersequence (fig. 4.25a), 256 t_1 increments would be recorded (corresponding to the eight blue dots); for the gramicidin sample used here, the largest value of t_1 (denoted as AQ_1) is around 60 ms. The default TopSpin processing routine for 2D NMR applies forward linear prediction (LP)^{69–72} in the indirect dimension, such as to double the number of points: the data points obtained through LP are indicated by orange dots. This leads to an *effective* AQ_1 which is twice as large, denoted as $AQ_{1,\text{eff}}$. Finally, zero filling (ZF) is applied to increase the digital resolution to a given value, as represented by the green dots.

In the k -scaled spectrum, both AQ_1 (and thus $AQ_{1,\text{eff}}$) are halved, in return for a doubling of the number of scans (fig. 4.25b). The resolution in the indirect dimension is proportional to $AQ_{1,\text{eff}}$; thus, this also corresponds to a $2\times$ decrease in resolution. However, this can be counteracted through the use of extra linear prediction (fig. 4.25c) to extend $AQ_{1,\text{eff}}$ back to its original value. The SW-scaled spectra (figs. 4.25d and 4.25e) are almost entirely equivalent to the k -scaled spectra in terms of their effect on AQ_1 and $AQ_{1,\text{eff}}$, except that the sampling schedule is very slightly modified.



Figure 4.25: Pictorial representation of k - and SW-scaling in NOAH ^{15}N modules. Each blue dot represents 32 t_1 increments physically acquired as part of the experiment; the experimental time is proportional to the number of blue dots, and is constant across all of these experiments. Orange dots represent 32 t_1 increments obtained through forward linear prediction, and green dots represent zeroes. (a) The default experiment. (b)–(c) k -scaled experiment, without and with extra linear processing to restore the original value of $AQ_{1,\text{eff}}$. (d)–(e) SW-scaled experiment, without and with extra linear processing to restore the original value of $AQ_{1,\text{eff}}$.

Figure 4.26 shows the effects of performing k - or SW-scaling on the ^{15}N HMQC module (without any extra linear prediction beyond the default). In this case, these scaling procedures can in fact can lead to significant gains in SNR (as measured by peak heights), with up to $2.6\times$ improvements being observed at the extreme of 8-fold k - or SW-scaling. This likely arises because the J_{HH} modulation in the indirect dimension (visible in the standard spectrum, fig. 4.26b) is no longer

being resolved: the largest gains are attained for the peak at 123 ppm, where this modulation is especially prominent.

The effect of adding extra linear prediction is shown in fig. 4.27. In general, the combination of scaling plus LP leads to improvements in spectral SNR of up to 6×. However, this is accompanied by distortions in the F_1 multiplet structure, especially for the k -scaled spectra (figs. 4.27c to 4.27h): it is possible that the corresponding SW-scaled spectra are not so heavily distorted because there are more data points to extrapolate from.

However, caution should be exercised when interpreting these results. Although this improvement in SNR is genuine, it is not necessarily the case that this represents a true improvement in *detection sensitivity*: in other words, processing techniques such as LP (and to some extent, NUS) do not always allow for better discrimination between signal and noise.^{73,74*} Further tests would need to be done on more dilute samples[†] to ascertain the benefits of the scaling-plus-LP routine on spectra with less intrinsic SNR.

4.3.3 ^{15}N sensitivity-enhanced HSQC

The implementation of the ^{15}N seHSQC modules is entirely identical to the ^{13}C versions previously discussed (§ 4.3.1), except for the following points:

- CTP gradient amplitudes were set using $g_1 = 80\%$ and $g_2 = \mp 16.2\%$ (note the sign change because of the negative magnetogyric ratio of ^{15}N);
- CTP gradient durations were lengthened to 2.5 ms (as discussed for the ^{15}N HMQC) in order to suppress artefacts in the seHSQC itself;
- the delays Δ and Δ' were both set to $1/(4 \cdot {}^1J_{\text{NH}})$ to maximise sensitivity for NH groups;
- ^{13}C adiabatic pulses were replaced with hard pulses on ^{15}N .

Multiplicity editing was not implemented or used in the ^{15}N experiments; there is generally little need for this.

Sensitivity analysis

The seHSQC is expected to provide sensitivity gains over the HMQC for two reasons: first, the seHSQC peaks are not split by ${}^nJ_{\text{HH}}$ in the indirect dimension, and secondly, the PEP transfer element leads to (in theory) a doubling in sensitivity for NH groups. To quantify these gains, I ran several NOAH-3 XS^+C^c experiments, where the first module was a ^{15}N HSQC, seHSQC1,

*In recent years, this issue has been investigated more thoroughly in the context of NUS.⁷⁵

†Or, perhaps, less sensitive instruments—although the 700 MHz cryoprobe used here was the only option for these supersequences.

./figures/noah/hmqc_scale.png

Figure 4.26: Effects of k - and SW-scaling on NOAH HMQC spectrum (taken from NOAH-3 $M_N S^+ C^c$ supersequences). Each HMQC spectrum is shown together with a positive projection onto the F_1 axis. The relative SNR of each peak, with respect to the standard spectrum, is indicated on each of the other projections. (a)–(b) Standard spectrum. (c)–(h) k -scaled spectra. (i)–(n) SW-scaled spectra. Data code: 7G-210310.

./figures/noah/hmqc_scale_lp.png

Figure 4.27: The same as in fig. 4.26, but with extra linear prediction applied to all scaled spectra to bring $AQ_{1,\text{eff}}$ up to its original value in the standard spectrum. Linear prediction of k times more points leads to a \sqrt{k} increase in noise; to account for this, all spectra are plotted with the same noise level. (a)–(b) Standard spectrum. (c)–(h) k -scaled spectra. (i)–(n) SW-scaled spectra. *Data code: 7G-210310.*

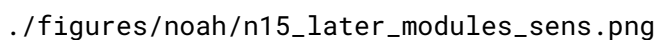
or seHSQC2 module (fig. 4.28). Including the ^{15}N HSQC module in this analysis allows us to determine how much of the sensitivity gain is due to multiplet collapse, and how much is due to the sensitivity enhancement block. The peak at 8.0 ppm is folded and is therefore omitted from this analysis.

./figures/noah/n15_modules_sens.png

Figure 4.28: Comparison of NOAH ^1H - ^{15}N modules; the 2D spectra and their positive projections onto the F_1 axis are shown. Numbers above each peak in the projections indicate sensitivity increases compared to the HMQC module (see, e.g., figs. 4.26a and 4.26b). (a)–(b) HSQC module. (c)–(d) seHSQC1 module. (e)–(f) seHSQC2 module. Data code: 7G-201017.

As can be seen, the HSQC alone allows for substantial sensitivity increases over the HMQC, with over $3\times$ gains being accomplished simply due to multiplet collapse. The seHSQC experiments push this even further, with an approximate $1.5\times$ sensitivity improvement for all peaks. In contrast to the ^{13}C case, the ^{15}N seHSQC1 module outperforms seHSQC2 in terms of raw sensitivity, though (as before) there is no clear explanation for this subtle difference.

However, this apparent advantage of the seHSQC1 vanishes when looking at the ^{13}C seHSQC module which comes later in the supersequence. When preceded by the ^{15}N HSQC or seHSQC1 modules, this module suffers from severely decreased sensitivity (fig. 4.29) as compared to when the seHSQC2 module is used. As the spectra and their F_1 projections show, this reduction in sensitivity actually stems from broadening in the indirect dimension. This in turn arises because $^1\text{H}^{15}\text{N}$ magnetisation (which includes the $^1\text{H}^{\text{C}}$ component sampled in this module) precesses in the transverse plane during the t_1 period of the ^{15}N HSQC and seHSQC1. Evolution of $^nJ_{\text{HH}}$, as well as T_2 relaxation, lead to a t_1 -dependent signal loss which (after Fourier transformation) is manifested as line broadening and ca. 65% decreased peak heights (figs. 4.29c and 4.29f).



./figures/noah/n15_later_modules_sens.png

Figure 4.29: Comparison of the ^{13}C seHSQC module from NOAH-3 XS^+C^c supersequences, where X is a ^1H - ^{15}N module. The 2D spectra, their positive projections onto the F_1 axis, as well as the relative intensities of all peaks (as compared to the corresponding module in the NOAH-3 $\text{M}_\text{N}\text{S}^+\text{C}^c$ supersequence), are shown. (a)–(c) X = ^{15}N HSQC. (d)–(f) X = ^{15}N seHSQC1. (g)–(i) X = ^{15}N seHSQC2. *Data code:* 7G-201017.

While the ^{15}N seHSQC2 module also does not preserve $^1\text{H}^{15}\text{N}$ magnetisation as well as the HMQC module (with an approximately 20% loss, see fig. 4.29i), this is not anywhere as drastic as with the other modules. Furthermore, these losses are constant across all t_1 increments, so there is no line broadening observed in the modules which follow. This small sensitivity loss in later modules is also a reasonable price to pay for the improvement in the ^{15}N module itself: typically, it is the ^{15}N module which has the smallest intrinsic sensitivity, so it is desirable to maximise this.

It should be noted that the ^{13}C seHSQC1 (and HSQC) modules also do place $^1\text{H}^{13}\text{C}$ magnetisation in the transverse plane during t_1 . However, they do not cause (appreciable) broadening in

downstream modules, as evidenced by the almost complete preservation of CLIP-COSY peak heights in fig. 4.10. This is because indirect-dimension spectral windows for ^{13}C experiments are often much wider, and the acquisition times (AQ_1 , following on from § 4.3.2) consequently shorter. For example, in the NOAH-3 XS^+C^c experiments shown here, the values of AQ_1 for the ^{15}N and ^{13}C experiments are respectively 60.1 ms and 5.38 ms.

CTP gradient duration

To verify that the 2.5 ms CTP gradients were necessarily in the ^{15}N seHSQC as well, I repeated the NOAH-3 $\text{S}_\text{N}^+\text{S}^+\text{C}^c$ experiment with increasing gradient durations. Only the seHSQC2 module was studied. It should be noted that the durations of *only* the CTP gradients g_1 and g_2 (in fig. 4.8c) were modified; g_3 and g_4 retain their original durations of 1 ms. The results, shown in fig. 4.30, are qualitatively very similar to that obtained with the HMQC (in fig. 4.24): increasing the gradient duration does not lead to substantial differences in signal intensity, but does provide much improved artefact suppression. In this case, equivalent results can be obtained using gradient durations of 2.2 ms to 2.3 ms; however, 2.5 ms still appears to be a reliable ‘default’ value which can be used without further optimisation.

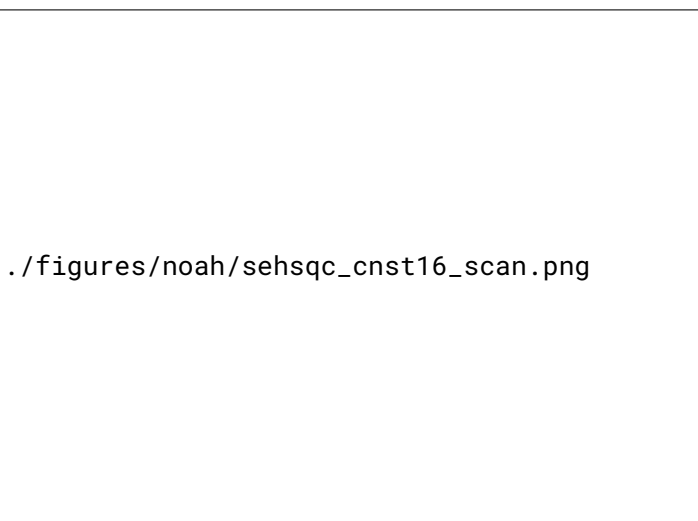


fig:sehsqc_cnst16

Figure 4.30: Variation of seHSQC2 signal and artefact intensity with CTP gradient duration, as measured by (absolute) peak heights in the positive F_2 projection. *Data code:* 7Z-200926.

k - and SW-scaling

Finally, the effects of k - and SW-scaling were also investigated for the seHSQC2 module. The effects of just performing scaling are very minimal (fig. 4.31): unlike the HMQC module where lowering the resolution avoids losses in peak height due to multiplet structure, there are no such gains for the seHSQC module. The use of indirect-dimension linear prediction, however, is

rather more successful for the seHSQC module (fig. 4.32): again this likely stems from the lack of multiplet structure in F_1 . As before, the application of LP to the SW-scaled spectra yields better peak shapes than the k -scaled spectra (compare, e.g., figs. 4.32g and 4.32m).

4.3.4 Dual HSQC and HSQC-TOCSY

Having completed our survey of ^{15}N modules, we now return to ^{13}C modules. In particular, I was interested in how *two* (or more) modules drawing on $^1\text{H}^{\text{C}}$ magnetisation could be combined in the same supersequence. All of the ^{13}C modules described so far fully consume $^1\text{H}^{\text{C}}$ magnetisation: if we were to crudely concatenate two such modules, the second of these modules will have greatly reduced sensitivity. This is acceptable only if the second module has a far greater intrinsic sensitivity. More ideally, we should like to have a way to *partition* the magnetisation pool between the two different modules as needed: this would allow us to balance their sensitivities.

This can be accomplished by modifying the first module to only excite a portion of $^1\text{H}^{\text{C}}$ magnetisation, storing the remainder along $+z$. The NOAH HSQC module—which is derived from the ASAP-HSQC experiment,^{11,45} previously described in § 3.4.5—does in fact allow for this. I therefore begin by describing SSX-type supersequences, where the first HSQC only partially excites $^1\text{H}^{\text{C}}$ magnetisation, and the second consumes the remainder. Here, X represents a homonuclear module, which in this section is the CLIP-COSY; however, the conclusions drawn here are applicable to any homonuclear module.

Supersequences with two HSQC modules

In order to accomplish partial $^1\text{H}^{\text{C}}$ excitation in the NOAH HSQC module (fig. 4.33), the INEPT delay Δ_{E} should be modified from its usual value of $1/(4J)$ (where J is short for $^1J_{\text{CH}}$). After the $90^\circ(I) - \Delta_{\text{E}} - 180^\circ(I, S) - \Delta_{\text{E}}$ INEPT block, the relevant product operators are

$$\cos(2\pi J \Delta_{\text{E}}) I_y - \sin(2\pi J \Delta_{\text{E}}) 2I_x S_z. \quad (4.15) \quad \{\text{eq:inept_changed}\}$$

In a ‘normal’ INEPT block, the choice of $\Delta_{\text{E}} = 1/(4J)$ makes the cosine term vanish, leaving us with only the term $-2I_x S_z$. Since this term is subsequently transferred to spin S and labelled in t_1 , this choice of $\Delta_{\text{E}} = 1/(4J)$ corresponds to *complete* excitation of $^1\text{H}^{\text{C}}$ magnetisation.

However, if we choose $\Delta_{\text{E}} < 1/(4J)$, then the first I_y term—which corresponds to ‘stored’ or unexcited $^1\text{H}^{\text{C}}$ magnetisation—is eventually returned to I_z , as shown by the product operator analysis in fig. 4.33.* To be precise, in order to excite a fraction f of $^1\text{H}^{\text{C}}$ magnetisation (and

*In the context of the ASAP experiments (both HMQC and HSQC), this is termed *Ernst angle* excitation because the unexcited magnetisation is stored for later repetitions of the *same* experiment, which mirrors the original Ernst angle for the 1D pulse-acquire experiment. However, for NOAH supersequences, the magnetisation is stored for other modules, so it is more correct to refer to this as a *partial* excitation.

./figures/noah/sehsqc_scale.png

Figure 4.31: Effects of k - and SW-scaling on NOAH seHSQC2 spectrum (taken from NOAH-3 $S_N^+S^+C^c$ supersequences). Each seHSQC spectrum is shown together with a positive projection onto the F_1 axis. The relative SNR of each peak, with respect to the standard spectrum, is indicated on each of the other projections. (a)–(b) Standard spectrum. (c)–(h) k -scaled spectra. (i)–(n) SW-scaled spectra. Data code: 7G-210310.

./figures/noah/sehsqc_scale_lp.png

Figure 4.32: The same as in fig. 4.31, but with extra linear prediction applied to all scaled spectra to bring $AQ_{1,\text{eff}}$ up to its original value in the standard spectrum. Linear prediction of k times more points leads to a \sqrt{k} increase in noise; to account for this, all spectra are plotted with the same noise level. (a)–(b) Standard spectrum. (c)–(h) k -scaled spectra. (i)–(n) SW-scaled spectra. Data code: 7G-210310.

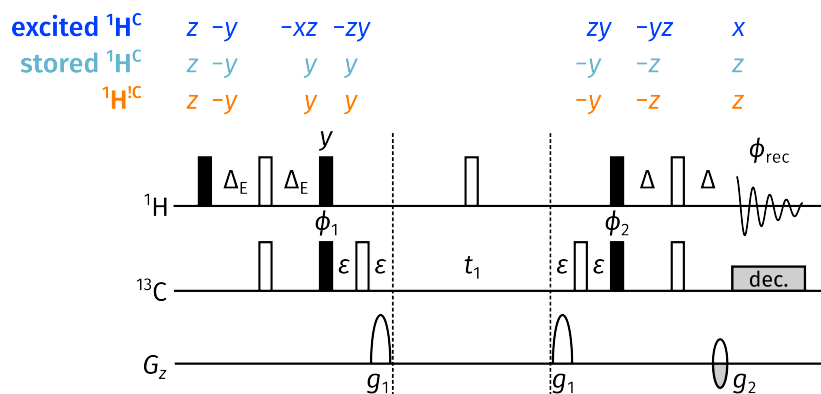


Figure 4.33: NOAH HSQC module with partial excitation, where the delay Δ_E is changed from the usual value of $1/(4J)$. As shown by the product operator analysis, proportion f of $^1\text{H}^C$ magnetisation is stored along $+z$ at the end of the sequence and can be sampled again in a later module. Gradient amplitudes are $(g_1, g_2) = (75\%, \pm 18.9\%)$; all other symbols have the same meaning as in fig. 4.8. (The different CTP gradient amplitudes are chosen to avoid accidental refocusing between different modules.)

store the remaining $(1 - f)$ for the next module), we require that

$$\Delta_E = \frac{2\Delta \arcsin f}{\pi}, \quad (4.16) \quad \{\text{eq:ssc_inept_delay}\}$$

where Δ is the usual value of $1/(4J)$. The spectra obtained from a NOAH-3 SSC^c supersequence, using this partial $^1\text{H}^C$ excitation in the first HSQC module (with $f = 0.8$), are shown in fig. 4.34.

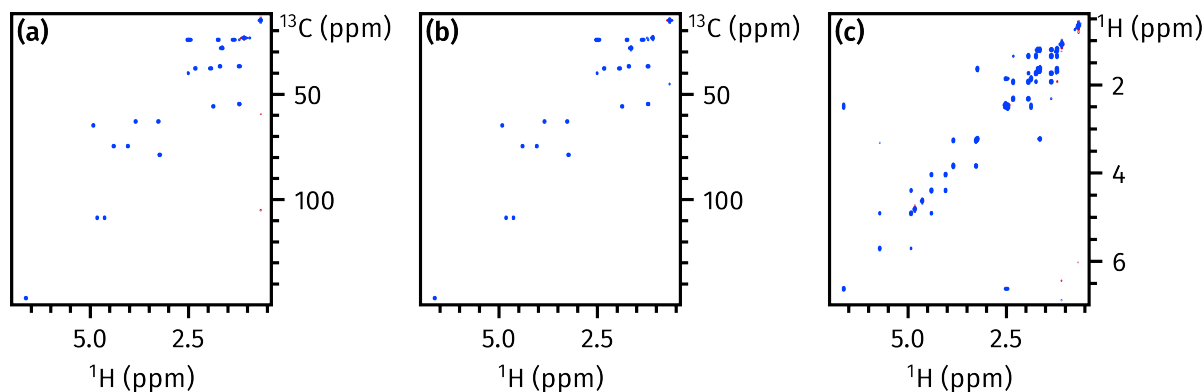


Figure 4.34: Spectra from a NOAH-3 SSC^c supersequence, where the INEPT delay of the first HSQC module was modified to only excite a fraction $f = 0.8$ of $^1\text{H}^C$ magnetisation. (a) First HSQC. (b) Second HSQC. (c) CLIP-COSY. Data code: 7A-201010.

In fig. 4.35a, the intensities of these spectra are compared against the HSQC and CLIP-COSY in a NOAH-2 SC^c supersequence. As expected, the first HSQC retains (around) 80% of its ‘base’ sensitivity, corresponding to the fraction of excited magnetisation. The second HSQC spectrum *nominally* only has access to the remaining 20% of magnetisation: however, due to recovery

of $^1\text{H}^\text{C}$ magnetisation during the FID of the first HSQC, this number is boosted to 65%. The CLIP-COSY sensitivity is (very slightly) decreased compared to a NOAH-2 SC^C supersequence: this is because of cumulative losses from the two HSQC modules.

Figures 4.35b to 4.35d detail several possible modifications to this basic scheme. In the first of these (fig. 4.35b), we further increase the sensitivity of the second HSQC module by converting it into a seHSQC2 module.* The CLIP-COSY sensitivity is slightly decreased due to poorer $^1\text{H}^\text{C}$ preservation, which is consistent with § 4.3.1. Note, however, that it is not possible to change the *first* HSQC into a seHSQC experiment: none of the seHSQC versions discussed in § 4.3.1 preserve unused $^1\text{H}^\text{C}$ magnetisation in the same way as the HSQC module above.

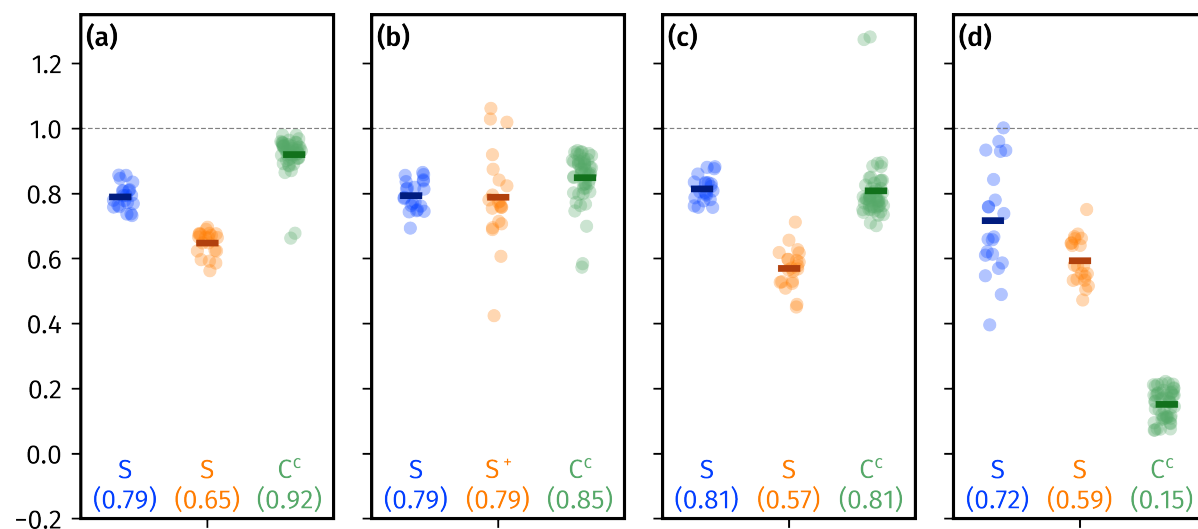


Figure 4.35: Comparisons of HSQC and CLIP-COSY sensitivities of NOAH-3 SSC^C and $\text{SS}^+\text{C}^\text{C}$ supersequences. The three groups of dots in each subplots refer to the three respective modules in the supersequence. Peak intensities are normalised against the HSQC and CLIP-COSY experiments in a NOAH-2 SC^C supersequence. (a) NOAH-3 SSC^C with $f = 0.8$ (the same spectra as shown in fig. 4.34). (b) NOAH-3 $\text{SS}^+\text{C}^\text{C}$ with $f = 0.8$. (c) NOAH-3 SSC^C with $f = 0.8$, plus 35 ms DIPSI-2 mixing after the first HSQC module. (d) A NOAH-3 SSC^C supersequence, but using the split-seHSQC implementation of Nolis et al.³⁸ (as opposed to the ASAP-HSQC module) for the double HSQC. Data code: 7A-201010.

Alternatively, it is also possible to include a period of isotropic mixing between the two HSQC modules: here, the DIPSI-2 sequence⁷⁶ was chosen. Since the $^1\text{H}^\text{C}$ magnetisation pool has been (partially) depleted, and the $^1\text{H}^\text{C}$ magnetisation pool is (almost) full, this should in theory lead to transfer of polarisation from the $^1\text{H}^\text{C}$ pool to $^1\text{H}^\text{C}$. However, when tested, this was not found to have a beneficial impact: in fact, small *decreases* in sensitivity were observed for both the second HSQC module and the final CLIP-COSY (fig. 4.35c).

Lastly, it should also be noted that the acquisition of two HSQC spectra in one experiment has also

*The sensitivity increases are not uniform because they depend on multiplicity.

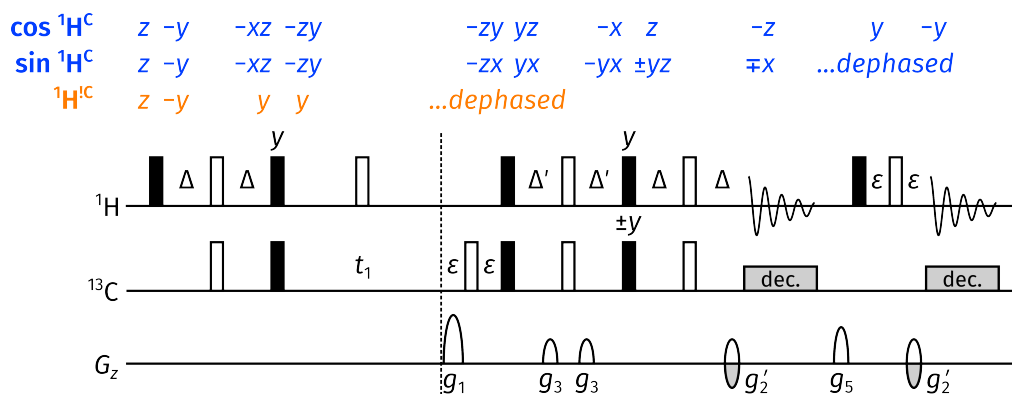


fig:split_crk

Figure 4.36: Split-seHSQC experiment used for the collection of two HSQC spectra.³⁸ All symbols have the same meaning as in fig. 4.8a; g_5 is a purge gradient with arbitrary amplitude.

been accomplished in a different way by Parella and coworkers.^{38,39} This relies on ‘splitting’ up the CRK seHSQC experiment (fig. 4.8a), such that the cosine- and sine-modulated components are separately detected.* This can be easily accomplished by inserting a detection period before the final ^1H 90° pulse (fig. 4.36), where the cosine-modulated component is stored as longitudinal magnetisation and the sine-modulated component is transverse (and in-phase).

However, this implementation does not fare as well in the context of the NOAH-3 SSC^c supersequences investigated here. The sensitivity of the three modules when using this is shown in fig. 4.35d: the two HSQC spectra have comparable, but slightly poorer, sensitivity than the $f = 0.8$ partial excitation scheme used in fig. 4.35a. There is also a slightly larger spread in sensitivity, which can be attributed to the fact that the seHSQC does not boost intensities uniformly. Furthermore, since this experiment (like the parent CRK seHSQC) dephases $^1\text{H}^1\text{C}$ magnetisation, the CLIP-COSY which follows suffers from a large drop in intensity. Prepending the experiment with the ZIP element to make a ‘split seHSQC2’ does not help, because the bulk magnetisation is in the transverse plane during the first FID. Finally, the split-seHSQC implementation does not easily allow for features such as multiplicity editing to be independently applied to one of the two signals.[†]

Figure 4.37 summarises all of these factors, and further shows how sensitivity varies as a function of the parameter f . From figs. 4.37a and 4.37b, it is clear that the sensitivity of the first HSQC is directly proportional to f . The sensitivity of the second HSQC module in fig. 4.37a stems from both the unexcited $(1 - f)$ proportion of $^1\text{H}^1\text{C}$ magnetisation, plus any that has recovered during the first FID: this latter component decreases as f increases. The CLIP-COSY intensities

*In my paper,¹ this was referred to as an ‘MFA’ (multiple-FID acquisition) implementation. I refrain from using this term here because it is ambiguous—after all, NOAH experiments are also multiple-FID experiments.

[†]It should at least be *possible* to apply editing to one signal using a modification similar to that done by Nolis et al.³⁹ However, that is not as simple as the ASAP implementation, where each module is distinct.

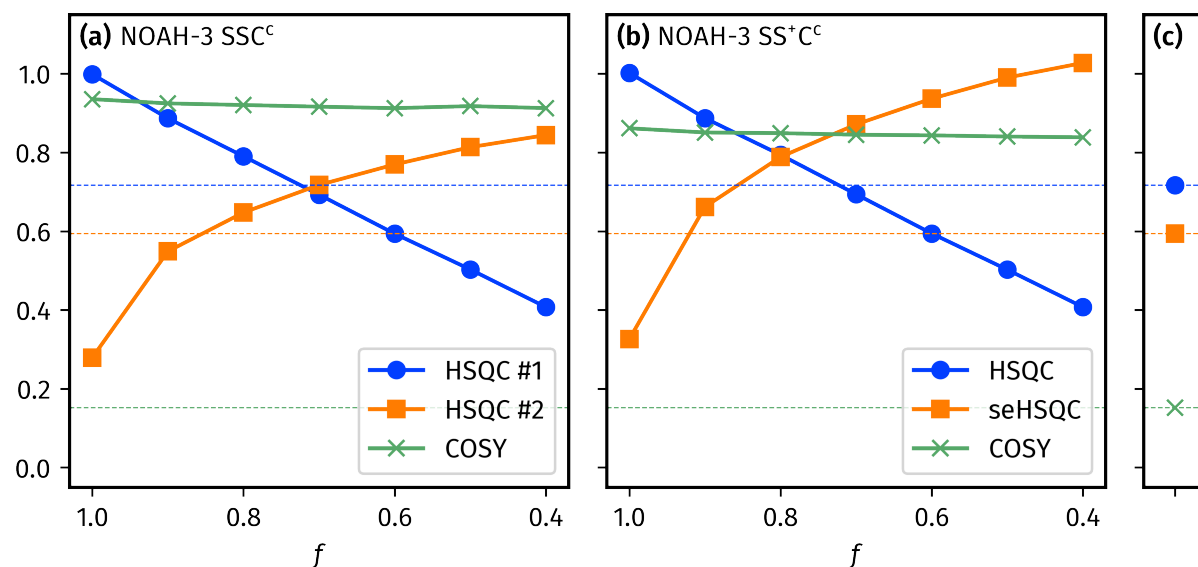


Figure 4.37: Sensitivity comparisons for NOAH-3 SSC^c and NOAH-3 SS⁺C^c supersequences. Intensities are compared against the HSQC and CLIP-COSY modules in a NOAH-2 SC^c experiment, and averaged over all peaks. (a) NOAH-3 SSC^c supersequences acquired with different values of f . (b) NOAH-3 SS⁺C^c supersequences acquired with different values of f . (c) Using the split-seHSQC implementation. Data code: 7A-201010.

generally do not vary with f . In fig. 4.37b, the second HSQC module is replaced with the seHSQC2: this allows f to be increased (from roughly 0.7 to 0.8) in order to obtain spectra with balanced sensitivities. Finally, for completeness, the split-seHSQC implementation is shown in fig. 4.37c; the numbers here are the same as in fig. 4.35d. It is clear that there are several values of f which allow the NOAH/ASAP-type implementation to outperform the split-seHSQC experiment in sensitivity.

On its own, the acquisition of two HSQC spectra—as has so far been shown—is not particularly groundbreaking. However, it is possible to differentiate the two HSQC signals and thereby extract more information. For example, one spectrum may be run without decoupling in order to measure one-bond coupling constants;^{38,77} multiplicity editing may be implemented;⁴⁵ or the indirect-dimension spectral width of one of the HSQC spectra can be changed in order to make use of spectral aliasing techniques.^{25,39} Most interesting of all, though, would be to modify the pulse sequence itself to obtain different *types* of ¹H–¹³C spectra: for example, the addition of an isotropic mixing block to the first HSQC yields an HSQC-TOCSY + HSQC combination,³⁸ which I now discuss.

HSQC-TOCSY

The addition of DIPSI mixing inside the partial-excitation HSQC module leads to an HSQC-TOCSY module (fig. 4.38a), which is (conceptually) identical to the ASAP-HSQC-TOCSY

experiment also previously reported by Luy and coworkers.⁷⁸ Note that the ^1H 90° pulse immediately after t_1 has a different phase from in the HSQC module: this ensures that $^1\text{H}^\text{C}$ (and unused $^1\text{H}^\text{C}$) magnetisation is returned to $+z$ after accounting for the extra 180° pulse at the end.

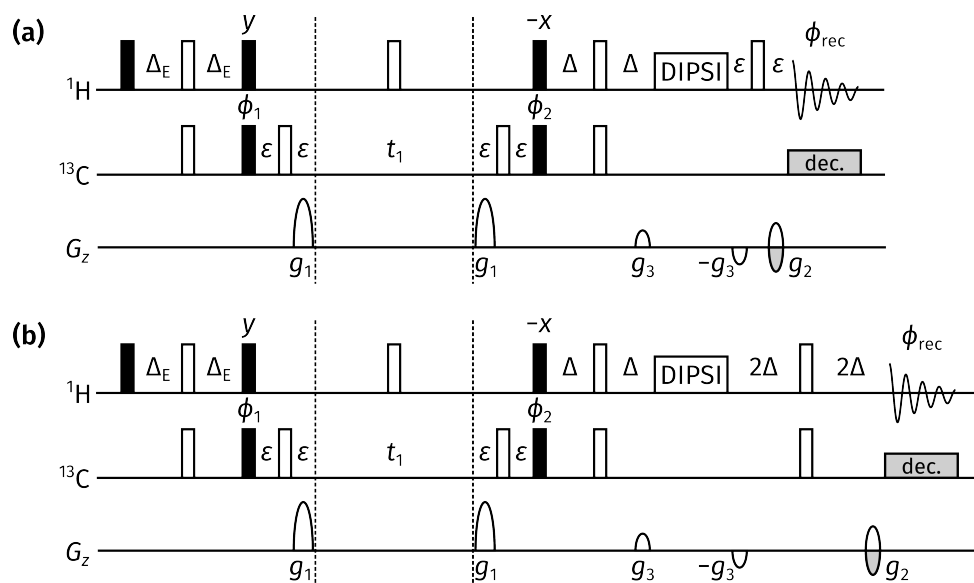


Figure 4.38: NOAH HSQC-TOCSY module: (a) without inversion of HSQC signals ('direct' responses); and (b) with inversion of HSQC signals.

The HSQC-TOCSY module may optionally be implemented with inversion of ‘direct’, HSQC-type responses, which correlate ^{13}C nuclei with directly bonded protons. This is to be contrasted with the ‘indirect’ responses, which correlate ^{13}C nuclei with other remote protons (in the same spin system), and represent magnetisation which has been transferred during the isotropic mixing period. This inversion may be accomplished by expanding the final gradient echo to a duration of $4\Delta = 1/J$ (fig. 4.38b); ^{13}C -bound protons will evolve under $^1J_{\text{CH}}$ and acquire an additional minus sign compared to remote protons.*

The use of such editing in the HSQC-TOCSY is perhaps slightly risky, because it may lead to unwanted peak cancellation through accidental overlap. Furthermore, if used together with a second HSQC module (as discussed here), this information does not need to be encoded in the HSQC-TOCSY. Thus, it is not enabled by default; the user must explicitly turn it on through an acquisition flag. The concept of inverting remote peaks is more important in the HSQC-COSY, which will be discussed in § 4.3.5.

With this module in hand, it is possible to implement either NOAH-3 S^TSC^c or NOAH-3 SS^TSC^c supersequences which yield both HSQC and HSQC-TOCSY data. In both cases, the first of the two ^{13}C modules can be adjusted to only partially excite $^1H^C$ magnetisation. However, the

*Of course, the remote protons may also happen to be bonded to ^{13}C , but the chance of this is only $\sim 1\%$.

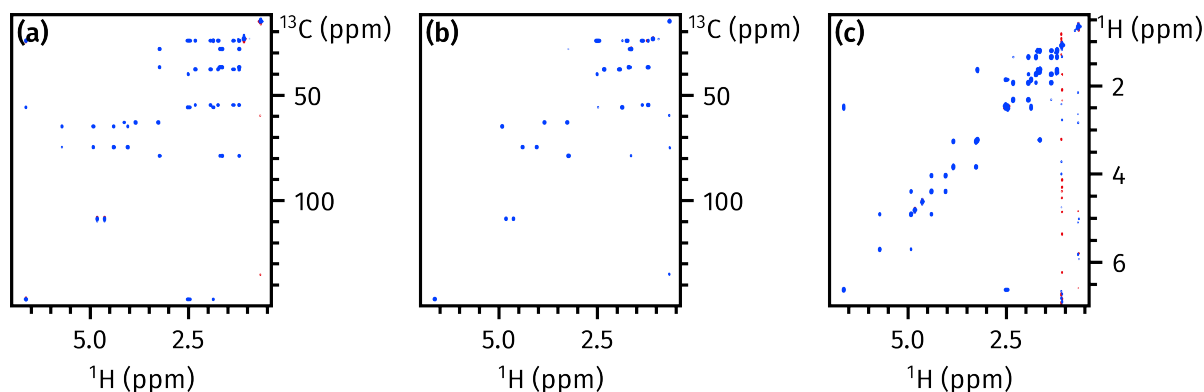


Figure 4.39: Spectra from a NOAH-3 $S^T S^+ C^C$ supersequence. (a) HSQC-TOCSY ($f = 0.9$). (b) seHSQC2. (c) CLIP-COSY. Data code: 7A-210126.

former is preferred as the HSQC-TOCSY has a lower intrinsic sensitivity compared to the HSQC: thus, it is better to place this first in the supersequence, and to also use a larger value of f in order to balance the relative sensitivities. Figure 4.39 shows an example of the spectra obtained with a setting of $f = 0.9$.

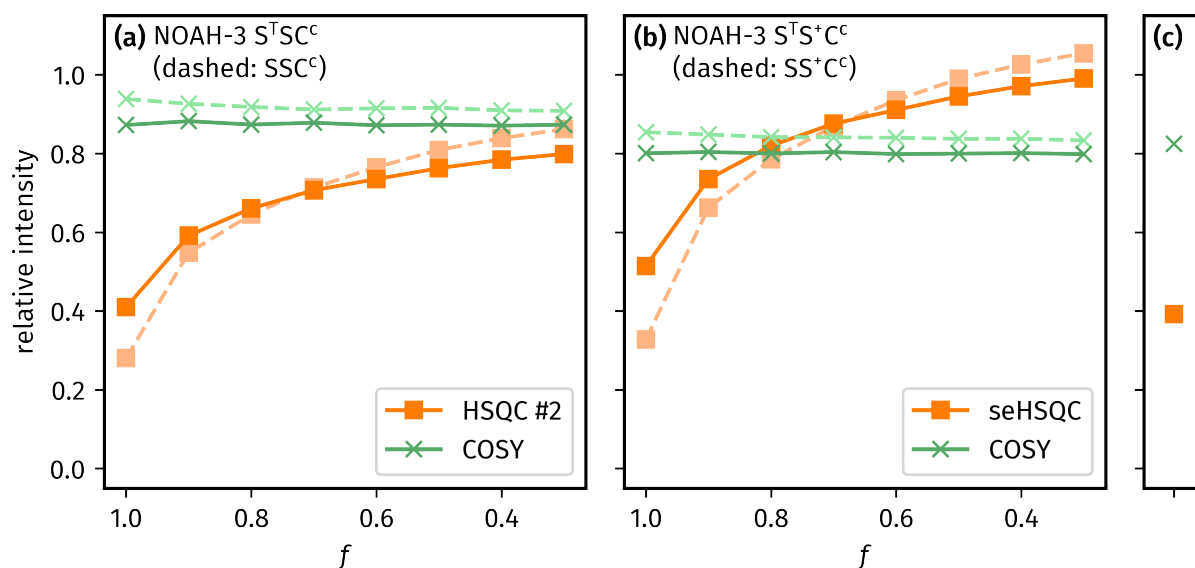


Figure 4.40: Sensitivity comparisons for NOAH-3 SSC^C and NOAH-3 $S^T S^+ C^C$ supersequences. The intensities of the latter two modules are compared against the HSQC and CLIP-COSY modules in a NOAH-2 SSC^C experiment, and averaged over all peaks. (a) NOAH-3 $S^T S^+ C^C$ supersequences acquired with different values of f ; the dashed lines are the corresponding intensities in the NOAH-3 SSC^C supersequence. (b) The same, but with the seHSQC2 as the second module instead. (c) The corresponding intensities of the second and third modules in a seHSQC-TOCSY + HSQC + CLIP-COSY supersequence: this is to be compared with the first data point ($f = 1$) in (a). Data code: 7A-210126.

Finally, I performed a series of experiments to establish whether changing the first module from an HSQC (i.e. SSC^C) to an HSQC-TOCSY (i.e. NOAH-3 $S^T S^+ C^C$) would affect the sensitivities of the two latter modules. The results are shown in figs. 4.40a and 4.40b, where the solid lines represent

the supersequences starting with the HSQC-TOCSY, and the dashed lines those starting with the HSQC. At large values of f (corresponding to depletion of the $^1\text{H}^{\text{C}}$ pool), the subsequent ^{13}C module experiences sensitivity *gains* when the HSQC-TOCSY is used. However, this changes at smaller values of f , where a drop in intensity is instead observed. For the CLIP-COSY module, the HSQC-TOCSY leads to slightly lower sensitivities across the board. All of these changes are, however, extremely minor: the supersequences shown here still work entirely as expected.

Figure 4.40c shows one final alternative which has not yet been considered: the use of the seHSQC-TOCSY⁵⁷ as the first module. This experiment is similar to the seHSQC2 module, but with the addition of isotropic mixing. Although this fully maximises the intensity of the HSQC-TOCSY component (not shown in fig. 4.40), and also preserves $^1\text{H}^{\text{C}}$ magnetisation for the CLIP-COSY (as evidenced by the relatively high CLIP-COSY intensity in fig. 4.40c), it cannot retain any portion of $^1\text{H}^{\text{C}}$ magnetisation. Thus, any later module which draws on the same magnetisation pool will only be able to use any signal which has recovered during the FID, just like in an experiment run with $f = 1$. In this case, the second module is a plain HSQC (not seHSQC): thus, its sensitivity is similar to the leftmost point in fig. 4.40a.

4.3.5 HSQC-COSY

One downside of the HSQC-TOCSY experiment discussed in the previous section is the (largely) indiscriminate transfer of magnetisation effected by the DIPSI mixing. It is difficult to determine how many transfer steps give rise to each peak, unless several HSQC-TOCSY spectra with different mixing times are recorded, which is a time-consuming process.*

For unambiguous spectral assignment, it may be preferable to have a mixing process which only effects coherence transfer across a single coupling: this can be described as an HSQC-COSY experiment. Similar experiments, including the H2BC,^{79,80} 2BOB/H2OBC,⁸¹ and HMQC-COSY⁸² have previously been proposed: the 2BOB experiment in particular has previously been incorporated in NOAH supersequences.⁵¹ These often use constant-time techniques in order to remove $^nJ_{\text{HH}}$ splittings and minimise linewidths in the indirect dimension; however, the drawback of this approach is that peak *amplitudes* are modulated by $^nJ_{\text{HH}}$. Furthermore, it is not generally possible to obtain absorption-mode lineshapes for all peaks in the spectrum: typically the ‘direct’ responses are in-phase absorption, and ‘indirect’ responses antiphase dispersion. (Here, the terms in-phase and antiphase are used with respect to $^nJ_{\text{HH}}$; specifically, for the indirect peaks, this refers to the ‘active’ coupling over which the coherence was transferred).

*Of course, as per the previous section, this could be done in a NOAH supersequence where each HSQC-TOCSY spectrum is assigned a fraction of the $^1\text{H}^{\text{C}}$ magnetisation. However, one must be wary of stretching the same magnetisation pool too thinly between many different modules: the resulting decrease in sensitivity may lead to peaks being lost.

HSQC-CLIP-COSY

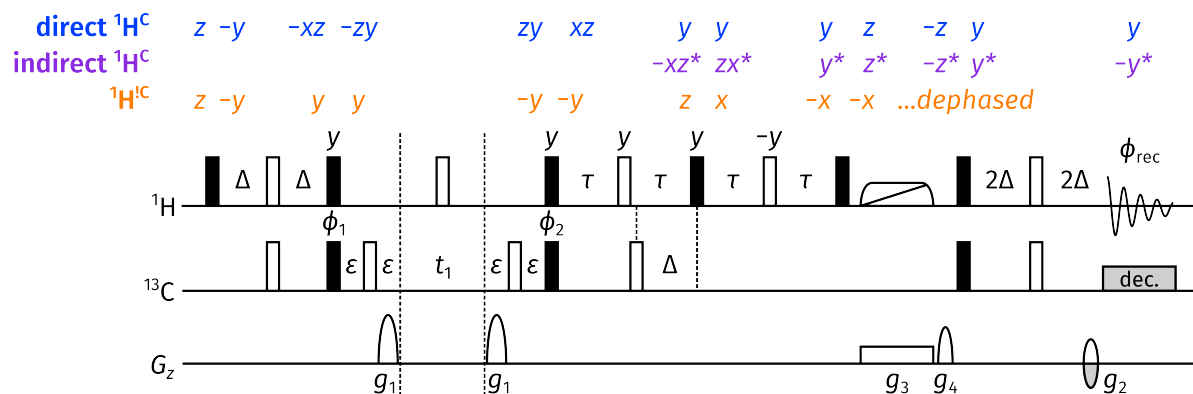


fig:hsqcc_clip_po

Figure 4.41: HSQC-CLIP-COSY experiment with product operator analysis for the HSQC-COSY signal derived from the $^1\text{H}^{\text{C}}$ magnetisation, as well as the bulk $^1\text{H}^{\text{C}}$ magnetisation. Both the ‘direct’, HSQC-type peaks, as well as the ‘indirect’ responses arising from coherence transfer in the perfect echo block, are analysed. The shorthand notation for product operators is expanded here to deal with a three-spin IKS system, where I and S are a mutually bonded ^1H – ^{13}C pair as usual, and K is a ‘remote’ proton coupled to I . Terms with asterisks are on spin K ; thus, for example, zx^* refers to an $I_z K_x$ term. The delay τ is chosen to be $1/(4 \cdot \sum J_{\text{HH}})$; typically, this sum of couplings is set as 30 Hz, leading to a value of $\tau = 8.33$ ms. The ZQF gradient g_3 should be calibrated as per Thrippleton et al.;⁸³ g_4 is a purge gradient with arbitrary amplitude. All other symbols have the same meaning as in fig. 4.8.

These problems are circumvented by the HSQC-CLIP-COSY experiment,^{84,85} where the basic HSQC experiment is combined with clean in-phase (CLIP) coherence transfer using a perfect echo^{86–88} and ZQF⁸³ (fig. 4.41). The use of a HSQC-type experiment means that $^nJ_{\text{HH}}$ does not evolve during t_1 , and the CLIP transfer ensures that all peaks have in-phase absorption lineshapes. Much like the HSQC-TOCSY experiment before it, this experiment may be implemented with direct/indirect response editing: it is this version of the experiment which is shown in fig. 4.41.* If this editing is not desired, then the final 2Δ – $180^\circ(I, S)$ – 2Δ spin echo can simply be reduced to a minimal gradient echo, i.e. ε – $180^\circ(I)$ – ε .

Unfortunately, the HSQC-CLIP-COSY experiment does not preserve $^1\text{H}^{\text{C}}$ magnetisation; thus, it cannot be directly used in a NOAH supersequence without sacrificing the sensitivity of terminal homonuclear modules. In particular, the ZQF used in the HSQC-CLIP-COSY experiment dephases all magnetisation that is not along z . If we wished to retain $^1\text{H}^{\text{C}}$ magnetisation, it would therefore have to (somehow) be placed along z during this period, and would have to be

*Note that this editing is orthogonal to *multiplicity editing*, which labels both direct and indirect responses with a sign that depends on the multiplicity of the ^{13}C nucleus detected in t_1 . The addition of multiplicity editing leads to highly confusing spectra, so is ignored here—although the option to do so is provided in the GENESIS pulse programmes if the user so desires.

differentiated from the HSQC-COSY signal *after* the ZQF, which is not possible.* On top of that, the experiment also cannot be modified to provide partial excitation of $^1\text{H}^{\text{C}}$ magnetisation, which limits the ways in which it can be combined with other ^{13}C modules.

Double spin echo HSQC-COSY

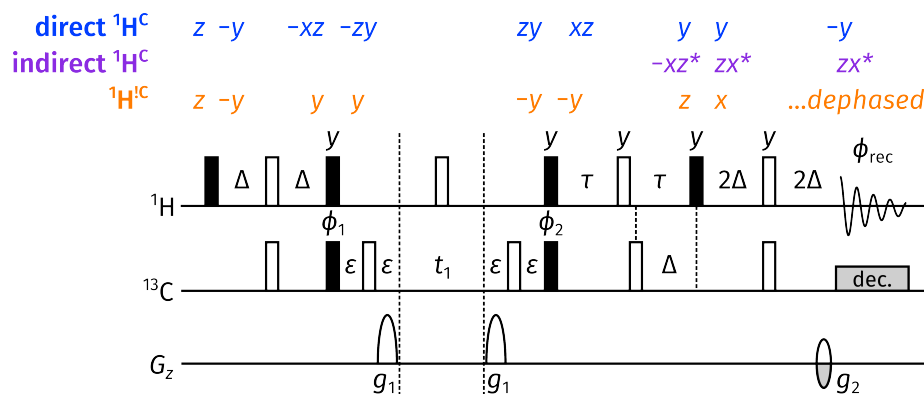


fig:hsqcc_dse_po

Figure 4.42: ‘Double spin echo’ HSQC-COSY experiment; all symbols have the same meaning as in fig. 4.41.

Before tackling these problems directly, I discuss a simpler version of the HSQC-COSY experiment, which uses a simple spin echo for $^nJ_{\text{HH}}$ evolution instead of the perfect echo of the CLIP version. Together with the final 4Δ spin echo, this forms a ‘double spin echo’ (DSE) version of the HSQC-COSY experiment (fig. 4.42): the ‘double’ refers only to the mixing section after t_1 . The removal of the CLIP coherence transfer element leads to mixed lineshapes in this experiment, where the direct responses are (mostly) in-phase absorption, and the indirect responses (mostly) antiphase dispersion.[†]

Like the CLIP version, this DSE experiment does not preserve bulk magnetisation; it is also incompatible with partial $^1\text{H}^{\text{C}}$ excitation. However, it does provide more raw sensitivity than the CLIP version: in the CLIP version, any antiphase signal at the end of the perfect echo is destroyed by the ZQF. All of this available signal is sampled in the DSE version, but this comes with a cost of not having pure absorption lineshapes.

It should be mentioned that prepending this DSE HSQC-COSY with the ZIP element would in fact return the bulk $^1\text{H}^{\text{C}}$ magnetisation to $+z$ at the end of the sequence. Unfortunately, I did not manage to test this experimentally.

*To be precise, although the $^1J_{\text{CH}}$ Hamiltonian could be used to separate bulk magnetisation and the HSQC-type ‘direct’ responses, the ‘indirect’ responses cannot be differentiated.

[†]The qualifier *mostly* is required because evolution of $^nJ_{\text{HH}}$ during the final spin echo leads to mixtures of in-phase absorption and antiphase dispersion. This evolution is generally small, though, because 2Δ is smaller than τ .

Triple spin echo HSQC-COSY

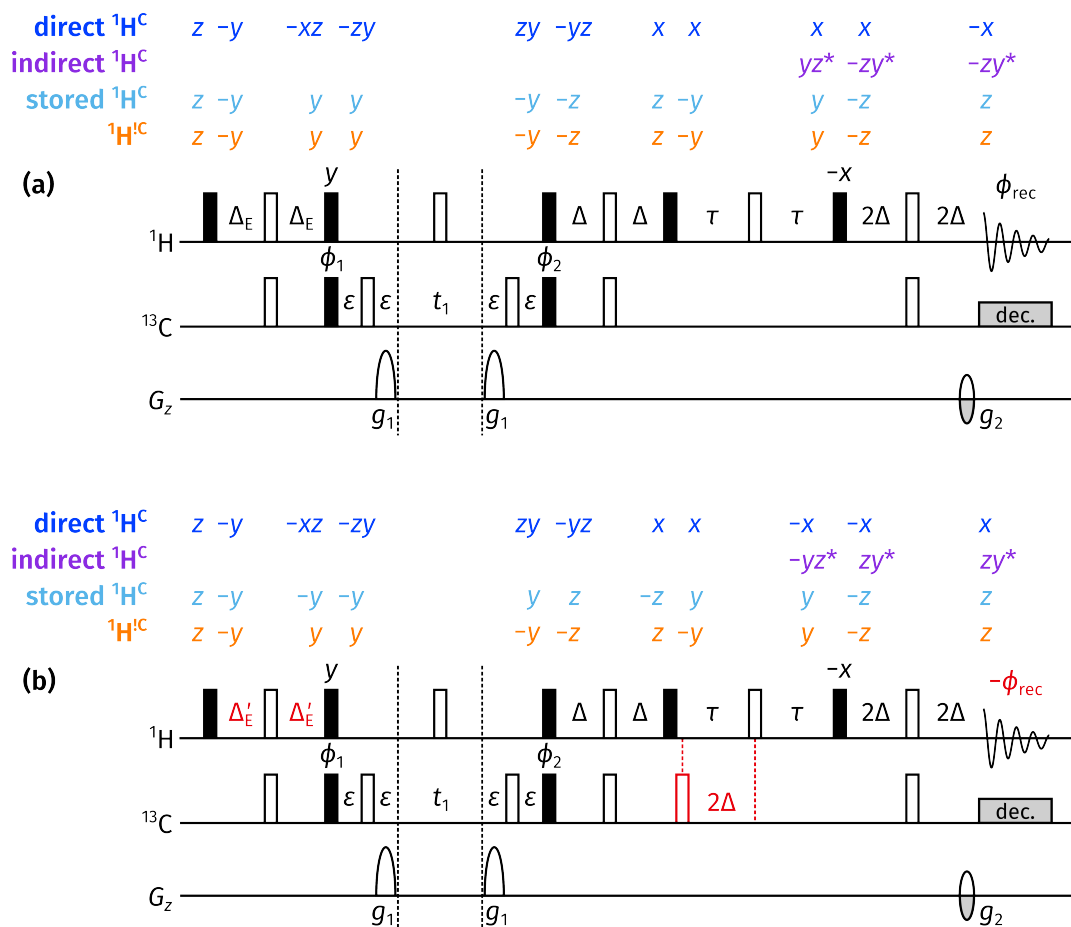


Figure 4.43: 'Triple spin echo' (TSE) HSQC-COSY experiment. (a) The first part of the experiment; this can be used on its own, but leads to spurious 'relayed' peaks arising via coherence transfer over two scalar couplings. (b) The second part of the experiment; co-adding this dataset with the first part leads to suppression of the relayed peaks. All symbols have the same meaning as in fig. 4.41.

In the DSE HSQC-COSY, the first of the two spin echoes after t_1 serves a dual purpose: $^1J_{\text{CH}}$ is allowed to evolve for a duration of $\tau - (\tau - \Delta) + \Delta = 2\Delta$ (thus generating peaks which are in-phase with respect to $^1J_{\text{CH}}$), and $^nJ_{\text{HH}}$ evolves for the total duration of 2τ (allowing coherence transfer to remote spins). The triple spin echo (TSE) HSQC-COSY is derived from the DSE version by separating the first spin echo into two distinct parts: one for $^1J_{\text{CH}}$ refocusing, and one for $^nJ_{\text{HH}}$ evolution. As shown by the product operator analysis in fig. 4.43a, this not only preserves the bulk $^1\text{H}^{13}\text{C}$ magnetisation, but is also compatible with partial $^1\text{H}^C$ excitation.

The problem with the TSE version is the spectral quality: consider an even larger spin system of the form $S-I-K-L$, where $\{I, K, L\}$ are ^1H and S is ^{13}C . At the end of t_1 , single-quantum magnetisation on spin I is present. Any evolution of J_{IK} in the first spin echo (of duration 2Δ) leads to terms of the form $2I_yK_z$, and can then be transferred onto spin K by the subsequent 90_x°

pulse. This magnetisation can then further evolve under J_{KL} during the 2τ spin echo, and then be transferred a *second* time by the 90°_x to spin L . Since the intensity of this transfer pathway is proportional to $\sin(2\pi J_{IK}\Delta)$, these ‘relay’ artefacts are especially prominent for large J_{IK} .

In order to suppress these, the experiment must be run a second time but with an additional 180° ^{13}C pulse inserted during the second spin echo (fig. 4.43b). Any magnetisation still on spin I will therefore evolve under $^1J_{\text{CH}}$ for a total period of 4Δ , leading to net inversion. However, magnetisation which has already been transferred to spin K at this point will not be inverted: it is this magnetisation which is responsible for the relay artefacts. Therefore, by subtracting the two datasets (or equivalently, inverting the receiver phase and adding the two datasets), the desired peaks will be added up and the artefacts cancelled through subtraction.

The insertion of this 180° pulse also causes any unexcited $^1\text{H}^\text{C}$ magnetisation to be inverted. In order to ensure that this is returned to $+z$ at the end of the sequence (and not $-z$), the initial INEPT delay must be *lengthened* instead of shortened, as per:

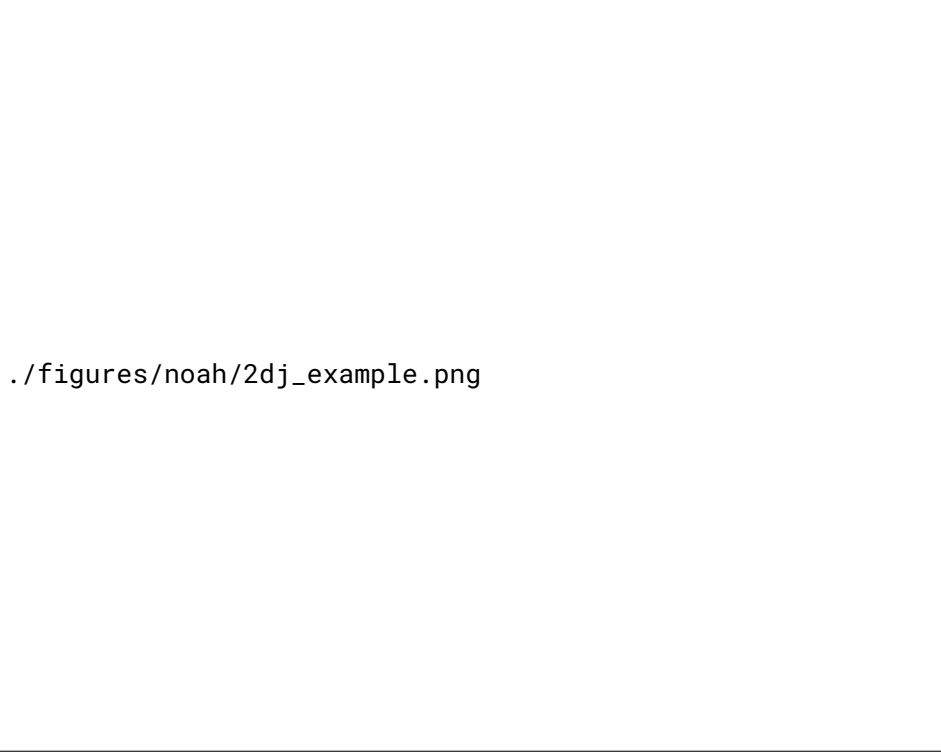
$$\Delta'_\text{E} = \frac{2\Delta(\pi - \arcsin f)}{\pi}, \quad (4.17) \quad \text{\small \{eq:delta_e_prime\}}$$

where, as before, f is the proportion of magnetisation to be excited.

4.3.6 2DJ and PSYCHE

‘Normal’ homonuclear modules are almost trivial to include in NOAH supersequences: since these are placed at the end of supersequences, there is rarely any need to modify them, as they do not need to preserve any magnetisation. One exception to this is the family of 2DJ and pseudo-2D pure shift experiments (here typified by PSYCHE), where the spectral width in the indirect dimension is extremely small, on the order of 50 Hz. In such cases, the number of t_1 increments required is far smaller than for a typical 2D experiment. Since—by default—each module in a NOAH supersequence is acquired with the same number of increments, directly adding such modules to the end of a supersequence would therefore prove suboptimal.

However, as described previously in § 4.3.3, it is possible to reduce the number of t_1 increments for a particular module, and in exchange, increase the number of scans recorded for that module. In the context of ^{15}N modules, this was a ‘special’ procedure referred to as k -scaling; however, for these homonuclear modules, it is natural and necessary. One difference in the implementation is that, instead of specifying a value k by which TD1 is scaled down by and NS scaled up by, the user is allowed to directly specify the number of t_1 increments as an integer (CNST37 in TopSpin). This value must be a divisor of TD1/NBL, i.e., the number of t_1 increments for all other modules. The indirect-dimension spectral width is specified as CNST38.



./figures/noah/2dj_example.png

Figure 4.44: Spectra obtained from a NOAH-3 $S_N^+S^+J$ supersequence. (a) ^{15}N seHSQC (256 t_1 increments and 2 scans per increment). (b) ^{13}C seHSQC. (c) PSYCHE 2DJ (32 t_1 increments and 8 scans per increment). *Data code:* 7G-201028.

The modules thus implemented include the standard magnitude-mode 2DJ experiment, the PSYCHE 2DJ experiment,⁸⁹ the original 1D PSYCHE,⁹⁰ and the 1D TSE-PSYCHE.⁸⁹ An example of the data thus obtained (with the PSYCHE 2DJ) is shown in fig. 4.44. One particular advantage of including PSYCHE-type modules in NOAH supersequences is that sensitivity is not likely to be at a premium: this is partly because of the increased number of scans, but also partly because other 2D experiments have comparably low sensitivity (meaning that in the time needed to acquire an HSQC, for example, the PSYCHE experiment will also have sufficient sensitivity). This allows the user to choose a relatively small flip angle (ca. 10°) for the PSYCHE saltire pulses in order to minimise artefacts from imperfect decoupling.

On top of that, for the 1D (TSE-)PSYCHE sequences, the extra transients can be used to perform SAPPHERE averaging:⁹¹ in this procedure, each chunk of the pure shift interferogram is collected multiple times while varying the point in time where the J-couplings are perfectly refocused. Summation of these data leads to the suppression of artefacts which arise due to the periodic J-modulation in the interferogram. This averaging is somewhat analogous to a phase cycle, and performing an 8-step SAPPHERE averaging procedure (for example) would often require the experiment to be lengthened beyond the duration which is truly necessary: however, in the context of NOAH this is obtained essentially ‘for free’. In the GENESIS pulse programmes,

this feature is enabled by default (it can be turned off by selecting the original modules using developer mode).

./figures/noah/psyche_wrongsw1.png

Figure 4.45: A series of 1D PSYCHE spectra obtained from the NOAH-3 $S_N^+S^+P$ super-sequence (saltire flip angle of 15°). (a) 1D PSYCHE spectrum acquired without SAPPHIRE averaging and an incorrect chunk size which is not an integral number of complex data points. (b) 1D PSYCHE spectrum with 8-step SAPPHIRE averaging and an incorrect chunk size; this manifests as phase errors which cannot be corrected. (c)–(d) The same as (a) and (b), but with the chunk size automatically corrected in the pulse programme. The impact of the SAPPHIRE averaging is less obvious in these datasets (compare (c) and (d)), but is more striking when larger chunk sizes are used, as discussed in the original paper.⁹¹ Data code: 7C-211123.

A final and more prosaic implementation detail is that in the 1D pure shift modules, the chunk size is automatically rounded to the nearest even multiple of the dwell time τ_{dw} (DW in TopSpin). This ensures that each chunk consists of an integral number of complex data points. Although this can be set by the user manually, it is very easy to forget, especially for someone not fully acquainted with the experiment; the results can be quite different, as illustrated in fig. 4.45. When an n -step SAPPHIRE averaging is used, the requirement is even stricter: the chunk size must be a multiple of $2n\tau_{dw}$. This is also encoded in the pulse programmes.

4.3.7 HMBC

The HMBC module is one which in fact does not fit perfectly into the NOAH principle of only exciting magnetisation which is needed. As described in § 4.1.3, the HMBC module should only

require magnetisation of protons which have long-range couplings to ^{13}C ; however, it ends up exciting *all* $^1\text{H}^{13}\text{C}$ magnetisation. This leads to sharply reduced, and also unbalanced, intensities of homonuclear modules which come later in the supersequences.

I made some early (and brief) attempts at devising a pulse sequence which sought to discriminate these two magnetisation components using a perfect echo.⁸⁷ However, this was quickly abandoned as it proved very difficult to *also* retain $^1\text{H}^{13}\text{C}$ magnetisation. I do not claim here that it is impossible to come up with a pulse sequence which does this, but it is certainly not easy, and ultimately I turned my focus to improving (rather than replacing) the HMBC module.

Suppression of one-bond artefacts

One of the issues with the NOAH HMBC module was that there were an unusual amount of one-bond artefacts, which arise from $^1\text{H}^{13}\text{C}$ magnetisation which is allowed to evolve during the pulse sequence. Generally, HMBC experiments seek to suppress this through the use of a low-pass J-filter (LPJF, see also § 3.4.7). The NOAH HMBC module *additionally* contains a zz-filter, which stores $^1\text{H}^{13}\text{C}$ magnetisation along +z before the LPJF. Thus, in theory, one-bond artefacts should be suppressed in the NOAH HMBC to an even greater extent.

However, this expectation is not borne out: in some cases, the NOAH HMBC in fact has *more intense* one-bond artefacts when compared against a standard HMBC experiment (figs. 4.46a and 4.46c). Even performing an optimisation of the LPJF delays, as described in § 3.4.7, did not lead to any reduction in artefacts. I hypothesised instead that these artefacts arose from imperfect manipulation of $^1\text{H}^{13}\text{C}$ magnetisation by the zz-filter.* In particular, any *antiphase* magnetisation (of the form I_xS_z or I_yS_z) generated after the zz-filter would be reconverted into in-phase I_x or I_y terms, which would not be destroyed by the LPJF. (The LPJF works based on the assumption that there is in-phase magnetisation at the beginning of it, which is true if the excitation element is just a ^1H 90° pulse.)

Such antiphase terms can be easily removed by the addition of a ^{13}C 90° pulse, which transforms them into a mixture of double- and zero-quantum terms: these are either unobservable, or can be efficiently dephased by CTP gradients. This technique is used in the CLIP-HSQC family of experiments,^{77,85} as well as the LPJF itself. In this case, we simply need to add an additional ^{13}C 90° pulse at the end of the zz-filter: this pulse is highlighted in fig. 4.2b. This results in a striking reduction of the one-bond artefacts, as shown in fig. 4.46b. The suppression accomplished with the addition of this 90° pulse is superior to that in the standard HMBC (fig. 4.46c), and is comparable to a standard HMBC with a third-order LPJF (fig. 4.46d). Of course, the NOAH module—which by default uses a second-order LPJF—can also be ‘upgraded’ to use a third-order

*It would be nice to back this up with simulations, but I did not have the time to run these.

LPJF. In GENESIS pulse programmes, this can be done using the `-DLP3` acquisition flag (although the results were not evaluated here).

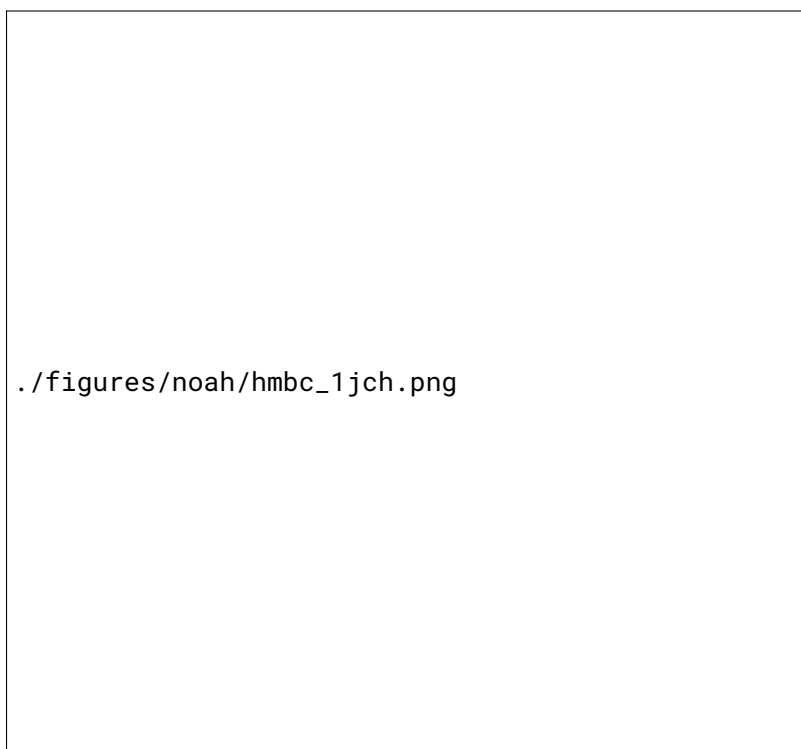


Figure 4.46: (a) NOAH zz -HMBC module without the additional 90° pulse. One-bond artefacts are highlighted in red. (b) NOAH zz -HMBC with the 90° pulse. (c) Standard library HMBC with a second-order LPJF. (d) Standard library HMBC with a third-order LPJF. Data code: 7A-210916.

Gradient selection schemes

Another point which was investigated (but bore less fruit) was the gradient scheme used for CTP selection. The NOAH module, as shown in fig. 4.2b, uses a ‘symmetric’ scheme where two gradients of equal amplitude surround the t_1 period: this encoding is later decoded by a third gradient just prior to acquisition. However, other choices exist: for example, the Bruker standard library HMBC (derived from the work of Cicero et al.⁹²) uses only two gradients in total, which have unequal amplitudes.

This gradient scheme cannot be directly used in a NOAH HMBC module, though. This is because the zz -filter element places $^1\text{H}^{\text{C}}$ magnetisation along the $+z$ axis just before the HMBC J-evolution delay (see fig. 4.2b). This magnetisation later experiences the ^1H 180° pulse in the middle of t_1 , which means that an extra 180° pulse must be added at the very end of the sequence to finally return it to $+z$. It is necessary to ensure that there is at least one gradient placed after this 180° pulse to ensure proper CTP selection (in the ‘symmetric’ scheme of fig. 4.2b, this is fulfilled by the gradient g_2).

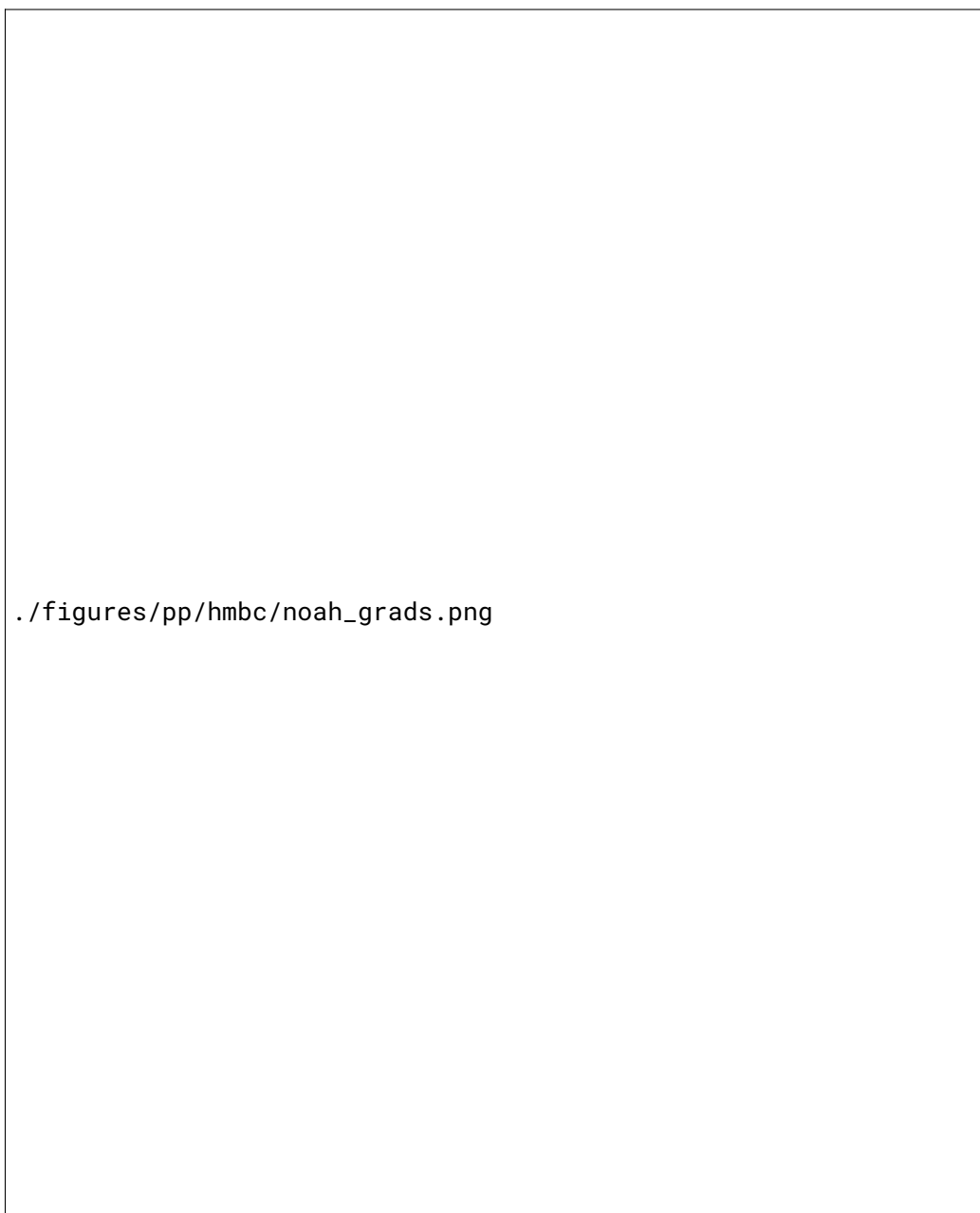


Figure 4.47: Alternative CTP gradient schemes investigated for the NOAH HMBC module. The coherences selected for during each gradient are indicated above each gradient, using the same notation for product operators as described in the *Preface*: the ‘upper’ term (e.g. $+$ in \pm) refers to the echo experiment, and the ‘lower’ term to the antiecho experiment. So, for example, $+\pm$ refers to selection of I_+S_+ during the echo experiment and I_+S_- during the antiecho experiment. Gradient amplitudes are as described in the text. (a) ‘Asymmetric scheme A’, modified from the standard library sequence to include an additional 180° pulse and gradient. (b) ‘Asymmetric scheme B’, where the 180° pulse is shifted forward to the end of t_1 . (c) ‘Asymmetric scheme C’, which modifies the zz -filter instead of using an extra 180° pulse. (d) The original ‘symmetric’ scheme (the same as in fig. 4.2b), placed here for convenience.

Using this knowledge, it is possible to construct several ‘asymmetric’ gradient schemes:

1. ‘Scheme A’ (fig. 4.47a) is modified from the Bruker standard library to include a 180° pulse and gradient at the end. The presence of an additional gradient means that there is a free parameter, here denoted as α , which can be used to control the relative amplitudes of these three CTP gradients. The gradient amplitudes are chosen as follows:

$$\text{echo:} \quad g_1 = gc_1 \quad g_2 = g \quad g_3 = gc_2 \quad (4.18)$$

$$\text{antiecho:} \quad g_1 = g \quad g_2 = gc_1 \quad g_3 = gc_2 \quad (4.19)$$

where $c_1 = -\alpha(\gamma_H - \gamma_C)/(\gamma_H + \gamma_C)$ and $c_2 = (1 - \alpha)(\gamma_H - \gamma_C)/\gamma_H$. In principle g is also a free parameter; for maximum suppression of artefacts I chose a relatively large value of 80%.

2. In ‘Scheme B’ (fig. 4.47b), the 180° pulse is shifted to immediately after t_1 , before any of the CTP gradients have been applied. This means that there is no need for a third gradient, and the CTP gradient amplitudes can be directly taken from the standard library sequence:

$$\text{echo:} \quad g_1 = g \quad g_2 = gc \quad (4.20)$$

$$\text{antiecho:} \quad g_1 = gc \quad g_2 = g \quad (4.21)$$

where $c = -(\gamma_H - \gamma_C)/(\gamma_H + \gamma_C)$ and $g = 80\%$.

3. ‘Scheme C’ (fig. 4.47c) simply does not add a 180° pulse, but instead modifies the phases of the zz -filter in order to place $^1\text{H}^C$ magnetisation along the $-z$ axis during the HMBC J-evolution delay. Here, the gradient amplitudes are the same as those in the standard library sequence as well as in scheme B.

It is of interest to note two limiting cases of scheme A: when $\alpha = (\gamma_H + \gamma_C)/(\gamma_H - \gamma_C) \approx 1.67$, we have that $g_1 : g_2 : g_3 = 1 : -1 : \pm 2\gamma_C/\gamma_H$, which mimics the original ‘symmetric’ scheme (fig. 4.47d); and when $\alpha = 1$, we have that $g_3 = 0$, i.e. a return to the two-gradient tactic of schemes B and C. In the tests which follow, I ran scheme A with $\alpha = 1.67$, $\alpha = 0.6$, and $\alpha = 0.3$.

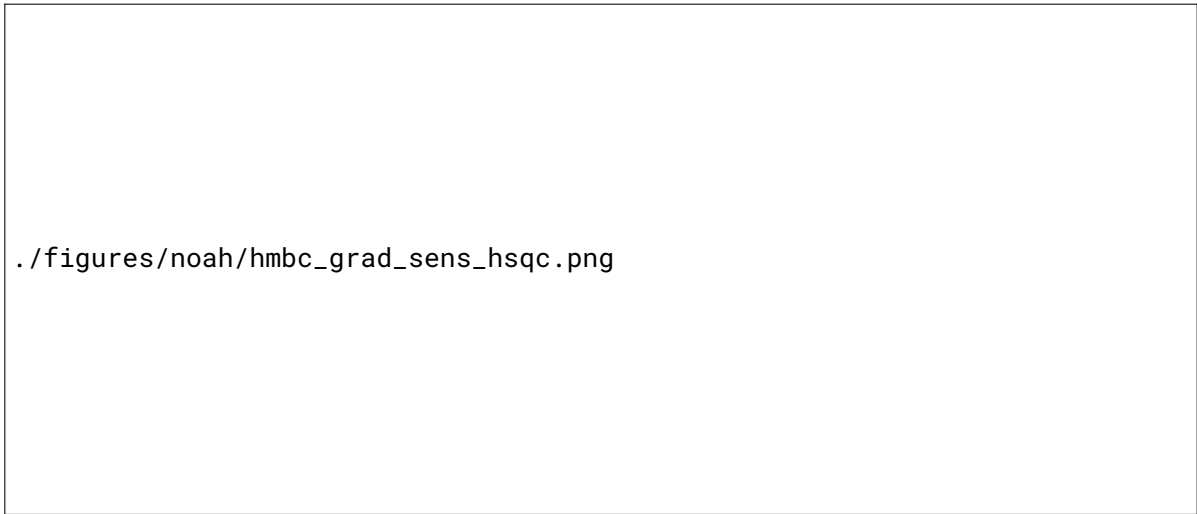
All of the different HMBC versions above, plus the original ‘symmetric’ scheme in fig. 4.2b, were tested in the context of a NOAH-2 BS supersequence using the andrographolide sample (fig. 4.48). Since the HMBC module is the first module in this supersequence, the values here are an accurate reflection of their intrinsic sensitivities. As can be seen, there is not much at all which separates the different versions (outliers with $> 2\times$ ‘sensitivity improvements’ can be attributed to different J-modulation in the multiplet). The most sensitive of these is asymmetric scheme C, which may be explained by the fact that it has one fewer 180° pulse: however, this comes with an



./figures/noah/hmbc_grad_sens.png

Figure 4.48: Sensitivities of various asymmetric HMBC gradient schemes, as compared to the symmetric scheme in fig. 4.2b. Each dot indicates one crosspeak in the HMBC spectrum; the numbers in parentheses are the average over all peaks. *Data code:* 7A-211226.

immediate drawback. Since scheme C places the $^1\text{H}^{\text{C}}$ magnetisation along $-z$ during the LPJF as well as the J-evolution delay Δ_{LR} (a total of ca. 70 ms), relaxation losses during this period lead to poorer retention of $^1\text{H}^{\text{C}}$ magnetisation for later modules, as shown by the decreased HSQC sensitivities in fig. 4.49. In contrast, all the other gradient schemes retain $^1\text{H}^{\text{C}}$ magnetisation equally well.



./figures/noah/hmbc_grad_sens_hsqc.png

Figure 4.49: Sensitivities of the HSQC module in a NOAH-2 BS supersequence, where the HMBC module is implemented using the gradient schemes of fig. 4.48. *Data code:* 7A-211226.

The final point worth studying is the quality of the HMBC spectrum itself. To do this, we need to look at the actual spectra (fig. 4.50). For the most part, the spectra are all the same; however,

there is a notable set of artefacts present in fig. 4.50b (scheme A with $\alpha = 1.67$) as well as fig. 4.50e (scheme B), highlighted in red boxes. These artefacts occur at the frequencies

$$(\Omega_1, \Omega_2) = \left(\Omega_S \pm \frac{\Omega_I}{2}, \Omega_I \right), \quad (4.22) \quad \text{\small {eq:hmbc_wing_artefact}}$$

and are in fact ‘wing’ artefacts similar to that observed in other modules [insert reference](#). In this case, they arise due to imperfect refocusing of the ^1H chemical shift during t_1 : specifically, whenever $I_z S_{\pm}$ terms are present during the second half of t_1 . Extra evidence for the origin of these artefacts comes from the observation that when the 180° pulse in the middle of t_1 is phase cycled, the artefacts are removed. In a standard HMBC, these terms would not be detected in the final FID; however, in this case, the addition of an extra 180° pulse after t_1 provides an opportunity for these to be converted back into observable spin- I magnetisation (through off-resonance effects or miscalibration).

The poorer performance may therefore be understood as follows: when scheme A is acquired with $\alpha = 1.67$, the gradients g_1 and g_2 have equal and opposite amplitudes, and so do not enforce any coherence selection on spin I during the second half of t_1 . Likewise, scheme B contains no gradients during the second half of t_1 .

The characteristics of these gradient schemes are summarised in table 4.4. As can be seen, the ‘best’ schemes are either the original symmetric scheme, or asymmetric scheme A with $\alpha \neq 1.67$. However, there is not much difference between these: it is not clear whether the improvement in sensitivity is reproducible across a wide range of samples, and in any case, the gains are extremely marginal.


Gradient scheme	HMBC sensitivity	HSQC sensitivity	Wing artefacts
Symmetric	1	1	No
Asymmetric A, $\alpha = 1.67$	1.05	0.99	Yes
Asymmetric A, $\alpha = 0.6$	1.04	0.99	No
Asymmetric A, $\alpha = 0.3$	1.05	0.99	No
Asymmetric B	1.06	1.01	Yes
Asymmetric C	1.09	0.71	No

tbl:hmbc_grads

Table 4.4: Comparison of HMBC gradient schemes discussed in this section: the data are a summary of figs. 4.48 to 4.50. *Data code:* 7A-211226.

Other artefacts

It has been established that the HMBC module (and supersequences containing it) are not fully ideal in terms of magnetisation preservation. However, there are also some other curious phenomena which have not been fully described in the literature. One of these is the presence

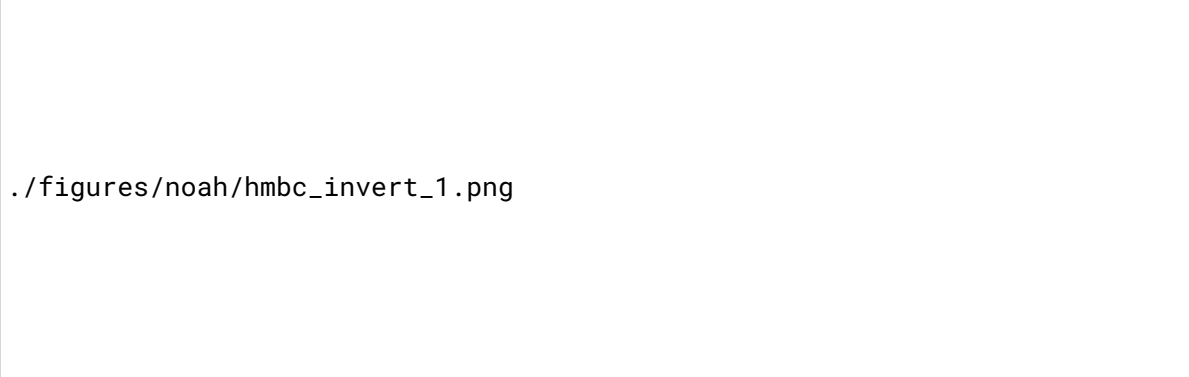


./figures/noah/hmbc_grad_spec.png

Figure 4.50: HMBC spectra acquired with the gradient schemes of fig. 4.48. Extra ‘wing’ artefacts present in two of the spectra (asymmetric scheme A with $\alpha = 1.67$, (b), and asymmetric scheme B, (e)) are highlighted in red boxes. Data code: 7A-211226.

of *inverted peaks* in the homonuclear X module(s) in a NOAH-3 BSX supersequence: this is illustrated in fig. 4.51a with the CLIP-COSY module ($X = C^c$). It is not clear why this occurs, because the HMBC module (and the gradients which follow) should dephase all $^1H^1C$ magnetisation. Although this leads to reduced sensitivity in the homonuclear module, in that the signal derives from polarisation which has recovered during the preceding FIDs, it is not clear why this polarisation should be *negative*. One clue lies in the fact that these peaks are very sensitive to the 1H 90° pulse width: simply changing this by 0.5 μs is sufficient to restore the correct signal sign (fig. 4.51b).

The modules placed between the HMBC and the homonuclear module also play an important role. When *two* HSQC modules are used, i.e. a NOAH-4 BSSC^c supersequence (using $f = 0.7$ as described in § 4.3.4—although this is unlikely to matter), the negative peaks are no longer observed (fig. 4.51c). In fact, having *no modules* between the HMBC and the homonuclear module is also (at least sometimes) acceptable: a separate set of data shows that the inverted peaks in an NOAH-3 BS⁺C^c experiment are not seen in a NOAH-3 S⁺BC^c supersequence



./figures/noah/hmbc_invert_1.png

Figure 4.51: (a) CLIP-COSY from a NOAH-3 BSC^c supersequence, acquired with a ¹H 90° pulse width of 11.28 μs (this value was obtained using the POISE calibration described in § 3.4.1). An inverted peak is visible at 2.25 ppm. (b) The same, but acquired using a 90° pulse width of 11.78 μs. (c) CLIP-COSY from a NOAH-4 BSSC^c supersequence. The 90° pulse width was 11.28 μs, the same as in (a). Data code: 7Z-220214.

(figs. 4.52a and 4.52b). The use of isotropic mixing (implemented as a sequence of adiabatic pulses,⁹³ and referred to as ‘ASAP’ mixing) just before the homonuclear module does not remedy this (figs. 4.52c and 4.52d). Unfortunately, a good explanation for these artefacts has remained elusive.



./figures/noah/hmbc_invert_2.png

Figure 4.52: (a) CLIP-COSY from a NOAH-3 BS⁺C^c supersequence. An inverted diagonal peak can be seen at 6.6 ppm. (b) From a NOAH-3 S⁺BC^c supersequence. (c)–(d) The same as (a) and (b), but with 40 ms ASAP mixing placed just before the CLIP-COSY module. Data code: 7A-211227.

¹⁵N HMBC module

The entirety of this section has—until now—been devoted to the ¹³C HMBC module. However, the techniques used in constructing this, including the implementation of the zz-filter, are equally applicable to a ¹⁵N HMBC. For simplicity, the NOAH ¹⁵N HMBC module uses a first-order LPJF (since ¹J_{NH} pairs are less common); this may be omitted if desired. To minimise the number of pulses, a simple magnitude-mode version of the HMBC is used (fig. 4.53). The implementation of this module within supersequences is discussed in greater detail within the context of *generalised supersequences*, in REF.

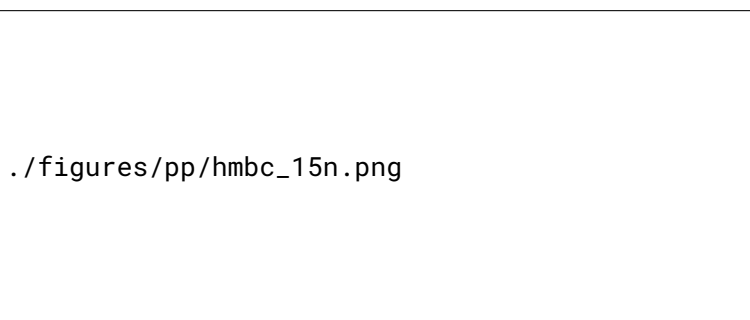


fig:noah_15n_hmbc

Figure 4.53: NOAH ¹⁵N HMBC module. The zz-filter can be implemented as necessary in the same way as for the ¹³C HMBC module (a final ¹H 180° pulse may also be required, but is not shown here). Delays are set as follows: $\Delta_N = 1/(2 \cdot {}^1J_{NH})$; $\Delta_{LR,N} = 1/(2 \cdot {}^nJ_{NH})$. Phase cycling is performed using $\phi_1 = \phi_{rec} = (x, -x)$ and $\phi_2 = (x, x, -x, -x)$. Gradient amplitudes are $(g_1, g_2, g_3, g_4) = (5\%, 70\%, 30\%, 50.1\%)$.

4.3.8 ADEQUATE

subsec:noah_adequate

The final ‘new’ module to be described in this section is the 1,1-ADEQUATE experiment,⁹⁴ which provides two-bond C–H correlations through a combination of ¹J_{CH} and ¹J_{CC}. Because of the requirement for two adjacent ¹³C nuclei, the sensitivity of the ADEQUATE experiment is considerably lower than almost all other NOAH modules considered so far. As established in § 4.1.1, sensitivity imbalances between different modules lead to less ideal supersequences with smaller effective time savings $\rho_{t,eff}$.

In this section, I only consider the design of the NOAH ADEQUATE module itself, which turns out to be extraordinarily simple. The ¹H pulses in the original ADEQUATE experiment mirror that of the CRK seHSQC almost perfectly, save for one extra 180° pulse. In particular, the INEPT excitation and the PEP transfer element are the same. Thus, the ADEQUATE module can be modified to preserve ¹H¹C magnetisation using exactly the same strategy in seHSQC2: namely, replacing the first ¹H excitation pulse with the ZIP element (fig. 4.54). In order to compensate for the extra 180° pulse (which arises in the constant-time period), the pulse phases in the ZIP element are modified accordingly: thus, the third ¹H 90° pulse has a phase of γ (instead of $-\gamma$ in

seHSQC2).

`./figures/pp/adequate.png`

fig:adequate_noah

Figure 4.54: NOAH 1,1-ADEQUATE module. The grey filled bar is a 120° pulse, optimised for ^{13}C double-quantum to single-quantum coherence transfer.⁹⁵ Delays are set as follows: $\Delta = 1/(4 \cdot ^1J_{\text{CH}})$, $\Delta' = 1/(8 \cdot ^1J_{\text{CH}})$, and $\tau = 1/(4 \cdot ^1J_{\text{CC}})$. Phase cycling is performed using $\phi_1 = (x, -x)$, $\phi_2 = (x, x, -x, -x)$, $\phi_3 = (y, y, -y, -y)$, $\phi_4 = (x, x, x, x, -x, -x, -x, -x)$, and $\phi_{\text{rec}} = (x, -x, -x, x, -x, x, x, -x)$. Gradient amplitudes are $(g_1, g_2, g_3) = (78.5\%, 77.6\%, \mp 59\%)$. Echo-antiecho selection is achieved by inverting the sign of g_3 as well as the pulse phase ϕ_3 .

An example of a NOAH-2 AB supersequence is shown in fig. 4.55. This is not the best setting to use the ADEQUATE module in, because the ^{13}C HMBC module has roughly 100 times the sensitivity of the ADEQUATE; however, it demonstrates that the ADEQUATE module does indeed work as intended. More constructive uses of the ADEQUATE module are deferred to [Section REF](#): in there, I discuss combinations with the (lower-sensitivity) ^{15}N HMBC module, and show how other modules may be added to form so-called ‘generalised’ supersequences.

`./figures/noah/ab.png`

fig:igoababab

Figure 4.55: Spectra from a NOAH-2 AB supersequence. (a) 1,1-ADEQUATE module. (a) HMBC module. *Data code:* 7T-211231.

4.4 Solvent suppression in NOAH

sec:noah__solvsupp

Solvent suppression is one of the most important aspects of modern NMR, and has been incorporated into a large number of experiments. It is not a particularly difficult task to implement

some basic solvent suppression techniques in NOAH supersequences, as will be described in this section. All suppression techniques shown here can be enabled via acquisition flags (the TopSpin ZGPTNS parameter); this means that there is no need to switch pulse sequences.

4.4.1 Presaturation

A simple first step is to implement simple presaturation of the solvent resonance during the recovery delay of the sequence. This often provides excellent suppression in the first module in a supersequence, and to a lesser extent, later modules (as the solvent magnetisation recovers during acquisition periods).

Presaturation is also included during long delays, in particular mixing times in NOESY experiments. The use of presaturation during the HMBC J-evolution delay was also tested, but was found to be generally unnecessary, especially since the HMBC module is typically placed first in supersequences.

4.4.2 Intrinsic suppression

A number of NOAH modules in fact come with an *intrinsic* form of solvent suppression, in that they return $^1\text{H}^{\text{X}}$ magnetisation (including that of solvents) to the +z axis at the end of the module. This is generally true of many of the HSQC-based NOAH modules, which seek to only sample $^1\text{H}^{\text{X}}$ magnetisation pool. Thus, these modules already have far better solvent suppression properties compared to standard library sequences: there is no need for further modification.

For these sequences, it is interesting to go one step further and to see how the solvent suppression varies with transmitter offset. This is less relevant if the solvent is just water (in which case it suffices to put the water peak on resonance), but may be important for samples in protonated solvents or mixtures thereof. I tested this by recording the first increment of the NOAH HSQC and seHSQC modules on an aqueous sample of sucrose, and integrating the water peak. The results (fig. 4.56) indicate that the HSQC module provides the best suppression across a range of offsets; of the two seHSQC modules, seHSQC1 provides more uniform suppression, whereas seHSQC2 has some regions ('spikes') where suppression is poorer than average.

It is not surprising that the more complicated seHSQC sequences have slightly poorer suppression: there are substantially more pulses involved which lead to cumulative errors, especially for peaks which are further away from resonance. However, it is not entirely clear why seHSQC2 has such large spikes. Some further investigation showed that the poorer suppression partly arises from imperfect cancellation of the water signal by phase cycling. This is, however, not a full explanation; it merely replaces one mystery with another. Nevertheless, it should be reiterated

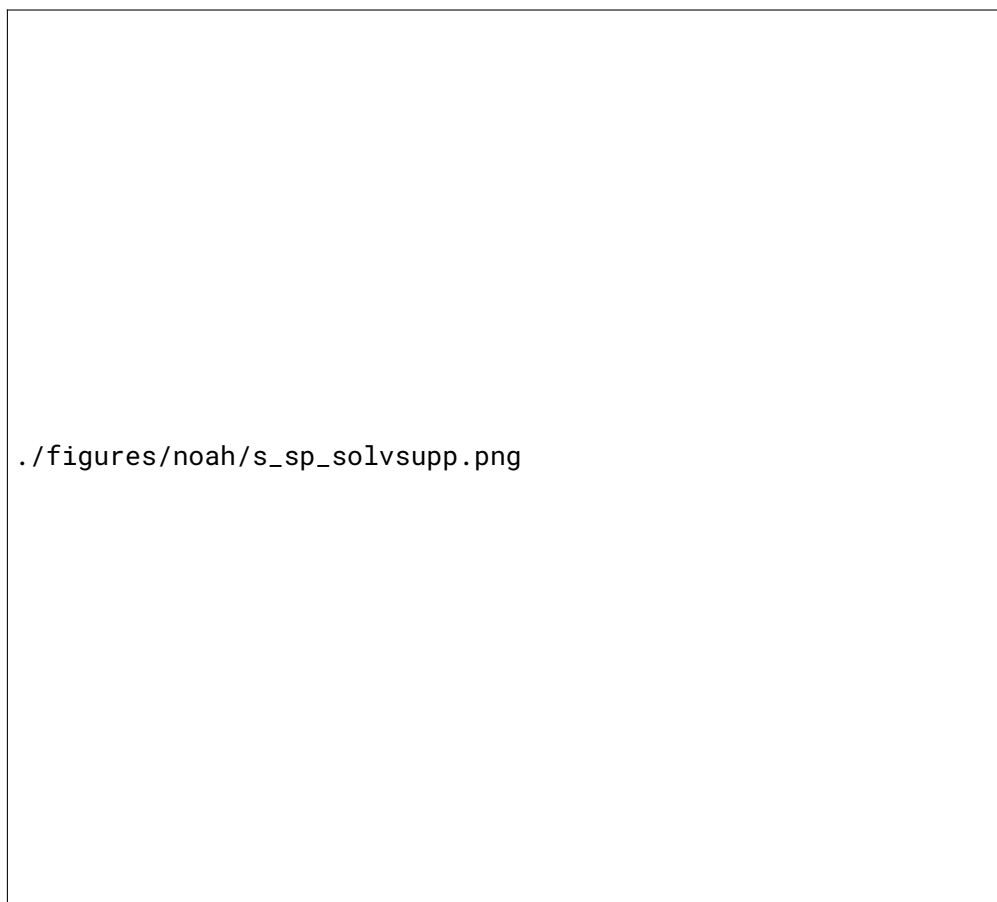


Figure 4.56: Residual water peaks observed in the first increment of NOAH HSQC and seHSQC modules, as a function of transmitter offset. The y -axes of the three subplots are the same. (a) HSQC module. (b) seHSQC1 module. (c) seHSQC2 module. Data code: 7S-201014.

that all of these sequences still provide excellent water suppression. The standard library seHSQC sequences, for example, do not even come close to this level of suppression (although these do dephase water magnetisation prior to acquisition, radiation damping still leads to a very large signal being detected).

4.4.3 Excitation sculpting

Since solvent suppression in HMBC and HSQC-type modules can be adequately accomplished through presaturation and intrinsic suppression, it remains to consider the suppression in homo-nuclear modules. These modules invariably occur at the end of supersequences, and thus almost any form of solvent suppression can be used: there is no need to consider how magnetisation needs to be preserved for other modules.

In practice, I chose to implement excitation sculpting⁹⁶ (ES) just prior to acquisition: the refocusing element chosen was a combination of a selective 180° sinc pulse and a hard 180° pulse.

This worked perfectly for almost all of the homonuclear modules used in NOAH supersequences, with only a few adjustments needed, e.g. for the PSYCHE modules to ensure that chemical shifts and J-couplings evolved for the correct amount of time.

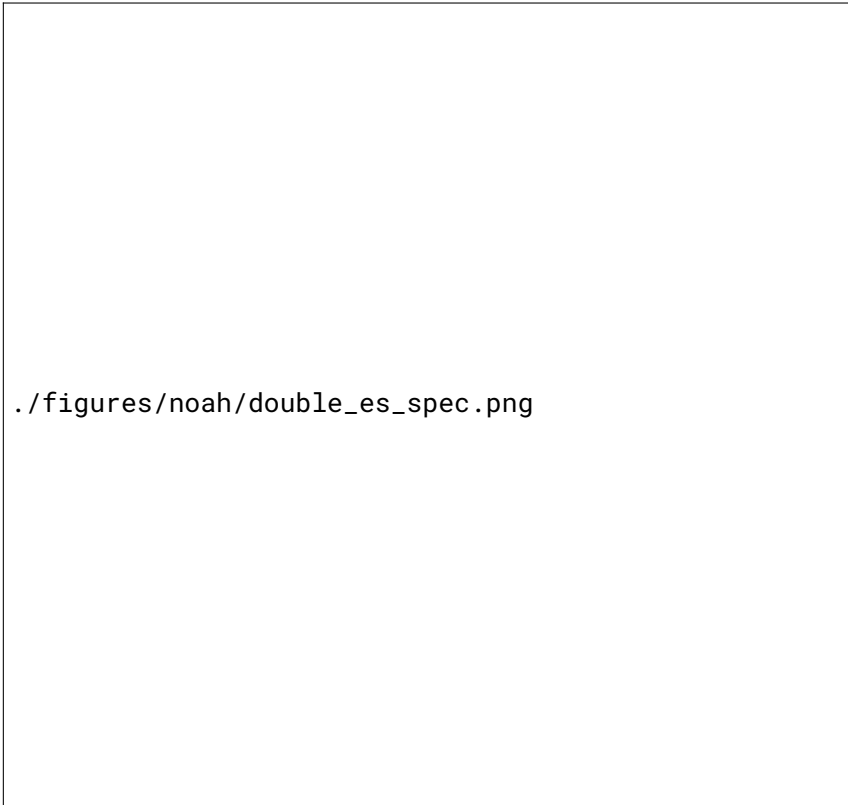
The case of the ‘double’ COSY + X homonuclear modules, however, proved to be more intricate. This is illustrated here using $X = \text{TOCSY}$, but the considerations below are equally applicable to $X = \text{NOESY}$ or ROESY . It is tempting to simply place ES blocks prior to both FIDs: in the COSY module, this dephases transverse solvent magnetisation as desired, and (in principle) should leave longitudinal magnetisation untouched, meaning that the TOCSY module which later consumes this should be unaffected.

However, this is not totally true. *Inside* the bandwidth of the selective 180° pulse, any longitudinal magnetisation experiences an 720° rotation; and *outside* of the bandwidth, it experiences a 360° rotation. However, *between* these two extremes, there is a crossover point where longitudinal magnetisation is sent into the transverse plane and subsequently dephased by gradients. These lead to nulls in fig. 4.57b, and peaks which fall within this range will be lost in the TOCSY module. This is visible in the spectra of fig. 4.58: although the water suppression obtained using this ‘double ES’ scheme is better, several peaks in the TOCSY spectrum have disappeared, because they fall precisely into these nulls. It proves better to omit the ES in the COSY module: an adequate degree of water suppression in the COSY can still be attained thanks to the use of presaturation.

./figures/noah/double_es_sim.png

Figure 4.57: Simulations showing the proportion of magnetisation retained by the excitation sculpting block (using a 2 ms sinc pulse). **(a)** Retention of transverse magnetisation: this was obtained by simulating the spectrum of a 90° –ES–detect pulse sequence. **(b)** Retention of longitudinal magnetisation: this was obtained using an ES– 90° –detect pulse sequence.

Of course, it may well be that *no* peaks fall within this null, and thus the better solvent suppression may be obtained at no cost. This was the case when the experiments in fig. 4.58 were reacquired on a 700 MHz spectrometer; or when the sinc pulse was lengthened to 4 ms. However, such fortuitousness cannot always be relied on.



./figures/noah/double_es_spec.png

Figure 4.58: (a)–(b) COSY and TOCSY spectra obtained from a NOAH-3 SCT super-sequence where excitation sculpting was placed before both the COSY and TOCSY FIDs. Although the water suppression is better, some peaks in the TOCSY module are lost. (c)–(d) The same, except that excitation sculpting was applied only in the TOCSY module. For all spectra shown here, presaturation of the water resonance was applied during the recovery delay. Data code: 4S-211105.

4.5 Parallel and generalised NOAH supersequences

Blah.

4.6 References

- (1) Yong, J. R. J.; Hansen, A. L.; Kupče, Ě.; Claridge, T. D. W. Increasing sensitivity and versatility in NMR supersequences with new HSQC-based modules. *J. Magn. Reson.* **2021**, 329, 107027, DOI: [10.1016/j.jmr.2021.107027](https://doi.org/10.1016/j.jmr.2021.107027).
- (2) Kupče, Ě.; Yong, J. R. J.; Widmalm, G.; Claridge, T. D. W. Parallel NMR Supersequences: Ten Spectra in a Single Measurement. *JACS Au* **2021**, 1, 1892–1897, DOI: [10.1021/jacsau.1c00423](https://doi.org/10.1021/jacsau.1c00423).

- Yong2022AC (3) Yong, J. R. J.; Kupče, Ě.; Claridge, T. D. W. Modular Pulse Program Generation for NMR Supersequences. *Anal. Chem.* **2022**, *94*, 2271–2278, DOI: [10.1021/acs.analchem.1c04964](https://doi.org/10.1021/acs.analchem.1c04964).
- Yong2022_ABBS (4) Yong, J. R. J.; Kupče, Ě.; Claridge, T. D. W. Uniting Low- and High-Sensitivity Experiments through Generalised NMR Supersequences. **2022**, manuscript in preparation.
- Kupce2021NRMP (5) Kupče, Ě.; Frydman, L.; Webb, A. G.; Yong, J. R. J.; Claridge, T. D. W. Parallel nuclear magnetic resonance spectroscopy. *Nat. Rev. Methods Primers* **2021**, *1*, No. 27, DOI: [10.1038/s43586-021-00024-3](https://doi.org/10.1038/s43586-021-00024-3).
- Yong2022RSCBook (6) Yong, J. R. J.; Kupče, Ě.; Claridge, T. D. W. In *Fast 2D solution-state NMR: concepts and applications*, Giraudeau, P., Dumez, J.-N., Eds., forthcoming, 2022.
- Barna1987JMR (7) Barna, J. C. J.; Laue, E. D.; Mayger, M. R.; Skilling, J.; Worrall, S. J. P. Exponential sampling, an alternative method for sampling in two-dimensional NMR experiments. *J. Magn. Reson.* **1987**, *73*, 69–77, DOI: [10.1016/0022-2364\(87\)90225-3](https://doi.org/10.1016/0022-2364(87)90225-3).
- Kazimierczuk2010PNMRS (8) Kazimierczuk, K.; Stanek, J.; Zawadzka-Kazimierczuk, A.; Koźmiński, W. Random sampling in multidimensional NMR spectroscopy. *Prog. Nucl. Magn. Reson. Spectrosc.* **2010**, *57*, 420–434, DOI: [10.1016/j.pnmrs.2010.07.002](https://doi.org/10.1016/j.pnmrs.2010.07.002).
- Mobli2014PNMRS (9) Mobli, M.; Hoch, J. C. Nonuniform sampling and non-Fourier signal processing methods in multidimensional NMR. *Prog. Nucl. Magn. Reson. Spectrosc.* **2014**, *83*, 21–41, DOI: [10.1016/j.pnmrs.2014.09.002](https://doi.org/10.1016/j.pnmrs.2014.09.002).
- Kazimierczuk2015MRC (10) Kazimierczuk, K.; Orekhov, V. Non-uniform sampling: post-Fourier era of NMR data collection and processing. *Magn. Reson. Chem.* **2015**, *53*, 921–926, DOI: [10.1002/mrc.4284](https://doi.org/10.1002/mrc.4284).
- Sunninghausen2014JACS (11) Schulze-Sünninghausen, D.; Becker, J.; Luy, B. Rapid Heteronuclear Single Quantum Correlation NMR Spectra at Natural Abundance. *J. Am. Chem. Soc.* **2014**, *136*, 1242–1245, DOI: [10.1021/ja411588d](https://doi.org/10.1021/ja411588d).
- Schanda2006JACS (12) Schanda, P.; Van Melckebeke, H.; Brutscher, B. Speeding Up Three-Dimensional Protein NMR Experiments to a Few Minutes. *J. Am. Chem. Soc.* **2006**, *128*, 9042–9043, DOI: [10.1021/ja062025p](https://doi.org/10.1021/ja062025p).
- Kupce2007MRC (13) Kupče, Ě.; Freeman, R. Fast multidimensional NMR by polarization sharing. *Magn. Reson. Chem.* **2007**, *45*, 2–4, DOI: [10.1002/mrc.1931](https://doi.org/10.1002/mrc.1931).
- Schanda2009PNMRS (14) Schanda, P. Fast-pulsing longitudinal relaxation optimized techniques: Enriching the toolbox of fast biomolecular NMR spectroscopy. *Prog. Nucl. Magn. Reson. Spectrosc.* **2009**, *55*, 238–265, DOI: [10.1016/j.pnmrs.2009.05.002](https://doi.org/10.1016/j.pnmrs.2009.05.002).
- Frydman2002PNASUSA (15) Frydman, L.; Scherf, T.; Lupulescu, A. The acquisition of multidimensional NMR spectra within a single scan. *Proc. Natl. Acad. Sci. U. S. A.* **2002**, *99*, 15858–15862, DOI: [10.1073/pnas.252644399](https://doi.org/10.1073/pnas.252644399).

- PeLupessy2003JACS (16) Pelupessy, P. Adiabatic Single Scan Two-Dimensional NMR Spectroscopy. *J. Am. Chem. Soc.* **2003**, *125*, 12345–12350, DOI: [10.1021/ja034958g](https://doi.org/10.1021/ja034958g).
- Frydman2003JACS (17) Frydman, L.; Lupulescu, A.; Scherf, T. Principles and Features of Single-Scan Two-Dimensional NMR Spectroscopy. *J. Am. Chem. Soc.* **2003**, *125*, 9204–9217, DOI: [10.1021/ja030055b](https://doi.org/10.1021/ja030055b).
- Tal2010PNMRS (18) Tal, A.; Frydman, L. Single-scan multidimensional magnetic resonance. *Prog. Nucl. Magn. Reson. Spectrosc.* **2010**, *57*, 241–292, DOI: [10.1016/j.pnmrs.2010.04.001](https://doi.org/10.1016/j.pnmrs.2010.04.001).
- Gouilleux2018ARNMRS (19) Gouilleux, B.; Rouger, L.; Giraudeau, P. Ultrafast 2D NMR: Methods and Applications. *Annu. Rep. NMR Spectrosc.* **2018**, 75–144, DOI: [10.1016/bs.arnmr.2017.08.003](https://doi.org/10.1016/bs.arnmr.2017.08.003).
- Kupce2003JMR (20) Kupče, Ě.; Freeman, R. Two-dimensional Hadamard spectroscopy. *J. Magn. Reson.* **2003**, *162*, 300–310, DOI: [10.1016/s1090-7807\(02\)00196-9](https://doi.org/10.1016/s1090-7807(02)00196-9).
- Kupce2003PNMRS (21) Kupče, E.; Nishida, T.; Freeman, R. Hadamard NMR spectroscopy. *Prog. Nucl. Magn. Reson. Spectrosc.* **2003**, *42*, 95–122, DOI: [10.1016/s0079-6565\(03\)00022-0](https://doi.org/10.1016/s0079-6565(03)00022-0).
- Jeannerat2000MRC (22) Jeannerat, D. High resolution in the indirectly detected dimension exploiting the processing of folded spectra. *Magn. Reson. Chem.* **2000**, *38*, 415–422, DOI: [10.1002/1097-458x\(200006\)38:6<415::aid-mrc665>3.0.co;2-u](https://doi.org/10.1002/1097-458x(200006)38:6<415::aid-mrc665>3.0.co;2-u).
- Bermel2009JACS (23) Bermel, W.; Bertini, I.; Felli, I. C.; Pierattelli, R. Speeding Up ^{13}C Direct Detection Biomolecular NMR Spectroscopy. *J. Am. Chem. Soc.* **2009**, *131*, 15339–15345, DOI: [10.1021/ja9058525](https://doi.org/10.1021/ja9058525).
- Njock2010C (24) Njock, G. B. B.; Pegnyemb, D. E.; Bartholomeusz, T. A.; Christen, P.; Vitorge, B.; Nuzillard, J.-M.; Shivapurkar, R.; Foroozandeh, M.; Jeannerat, D. Spectral Aliasing: A Super Zoom for 2D-NMR Spectra. Principles and Applications. *Chimia* **2010**, *64*, 235, DOI: [10.2533/chimia.2010.235](https://doi.org/10.2533/chimia.2010.235).
- Jeannerat2011eMR (25) Jeannerat, D. In *eMagRes*; Wiley: 2011, DOI: [10.1002/9780470034590.emrstm1187](https://doi.org/10.1002/9780470034590.emrstm1187).
- Nolis2007ACIE (26) Nolis, P.; Pérez-Trujillo, M.; Parella, T. Multiple FID Acquisition of Complementary HMBC Data. *Angew. Chem. Int. Ed.* **2007**, *46*, 7495–7497, DOI: [10.1002/anie.200702258](https://doi.org/10.1002/anie.200702258).
- Parella2010CMR (27) Parella, T.; Nolis, P. Time-shared NMR experiments. *Concepts Magn. Reson.* **2010**, *36A*, 1–23, DOI: [10.1002/cmr.a.20150](https://doi.org/10.1002/cmr.a.20150).
- Nolis2019JMR_pshSQC (28) Nolis, P.; Motiram-Corral, K.; Pérez-Trujillo, M.; Parella, T. Broadband homodecoupled time-shared ^1H – ^{13}C and ^1H – ^{15}N HSQC experiments. *J. Magn. Reson.* **2019**, *298*, 23–30, DOI: [10.1016/j.jmr.2018.11.005](https://doi.org/10.1016/j.jmr.2018.11.005).
- Kupce2006JACS (29) Kupče, Ě.; Freeman, R.; John, B. K. Parallel Acquisition of Two-Dimensional NMR Spectra of Several Nuclear Species. *J. Am. Chem. Soc.* **2006**, *128*, 9606–9607, DOI: [10.1021/ja0634876](https://doi.org/10.1021/ja0634876).
- Kupce2008JACS (30) Kupče, Ě.; Freeman, R. Molecular Structure from a Single NMR Experiment. *J. Am. Chem. Soc.* **2008**, *130*, 10788–10792, DOI: [10.1021/ja8036492](https://doi.org/10.1021/ja8036492).

- Kovacs2016MRC (31) Kovacs, H.; Kupče, Ě. Parallel NMR spectroscopy with simultaneous detection of ^1H and ^{19}F nuclei. *Magn. Reson. Chem.* **2016**, *54*, 544–560, DOI: [10.1002/mrc.4428](https://doi.org/10.1002/mrc.4428).
- Kupce2017ACIE (32) Kupče, Ě.; Claridge, T. D. W. NOAH: NMR Supersequences for Small Molecule Analysis and Structure Elucidation. *Angew. Chem. Int. Ed.* **2017**, *56*, 11779–11783, DOI: [10.1002/anie.201705506](https://doi.org/10.1002/anie.201705506).
- Kupce2021PNMRS (33) Kupče, Ě.; Mote, K. R.; Webb, A.; Madhu, P. K.; Claridge, T. D. W. Multiplexing experiments in NMR and multi-nuclear MRI. *Prog. Nucl. Magn. Reson. Spectrosc.* **2021**, *124–125*, 1–56, DOI: [10.1016/j.pnmrs.2021.03.001](https://doi.org/10.1016/j.pnmrs.2021.03.001).
- Haasnoot1984JMR (34) Haasnoot, C. A. G.; van de Ven, F. J. M.; Hilbers, C. W. COCONOSY. Combination of 2D correlated and 2D nuclear overhauser enhancement spectroscopy in a single experiment. *J. Magn. Reson.* **1984**, *56*, 343–349, DOI: [10.1016/0022-2364\(84\)90114-8](https://doi.org/10.1016/0022-2364(84)90114-8).
- Gurevich1984JMR (35) Gurevich, A. Z.; Barsukov, I. L.; Arseniev, A. S.; Bystrov, V. F. Combined COSY-NOESY experiment. *J. Magn. Reson.* **1984**, *56*, 471–478, DOI: [10.1016/0022-2364\(84\)90311-1](https://doi.org/10.1016/0022-2364(84)90311-1).
- MotiramCorral2018CC (36) Motiram-Corral, K.; Pérez-Trujillo, M.; Nolis, P.; Parella, T. Implementing one-shot multiple-FID acquisition into homonuclear and heteronuclear NMR experiments. *Chem. Commun.* **2018**, *54*, 13507–13510, DOI: [10.1039/C8CC08065H](https://doi.org/10.1039/C8CC08065H).
- Nolis2019MRC (37) Nolis, P.; Parella, T. Practical aspects of the simultaneous collection of COSY and TOCSY spectra. *Magn. Reson. Chem.* **2019**, *57*, S85–S94, DOI: [10.1002/mrc.4835](https://doi.org/10.1002/mrc.4835).
- Nolis2019CPC (38) Nolis, P.; Motiram-Corral, K.; Pérez-Trujillo, M.; Parella, T. Interleaved Dual NMR Acquisition of Equivalent Transfer Pathways in TOCSY and HSQC Experiments. *ChemPhysChem* **2019**, *20*, 356–360, DOI: [10.1002/cphc.201801034](https://doi.org/10.1002/cphc.201801034).
- Nolis2019JMR (39) Nolis, P.; Motiram-Corral, K.; Pérez-Trujillo, M.; Parella, T. Simultaneous acquisition of two 2D HSQC spectra with different ^{13}C spectral widths. *J. Magn. Reson.* **2019**, *300*, 1–7, DOI: [10.1016/j.jmr.2019.01.004](https://doi.org/10.1016/j.jmr.2019.01.004).
- Nagy2019CC (40) Nagy, T. M.; Gyöngyösi, T.; Kövér, K. E.; Sørensen, O. W. BANGO SEA XLOC/HMBC–H2OBC: complete heteronuclear correlation within minutes from one NMR pulse sequence. *Chem. Commun.* **2019**, *55*, 12208–12211, DOI: [10.1039/c9cc06253j](https://doi.org/10.1039/c9cc06253j).
- Nagy2020JMR (41) Nagy, T. M.; Kövér, K. E.; Sørensen, O. W. Double and adiabatic BANGO for concatenating two NMR experiments relying on the same pool of magnetization. *J. Magn. Reson.* **2020**, *316*, 106767, DOI: [10.1016/j.jmr.2020.106767](https://doi.org/10.1016/j.jmr.2020.106767).
- Nagy2021ACIE (42) Nagy, T. M.; Kövér, K. E.; Sørensen, O. W. NORD: NO Relaxation Delay NMR Spectroscopy. *Angew. Chem. Int. Ed.* **2021**, *60*, 13587–13590, DOI: [10.1002/anie.202102487](https://doi.org/10.1002/anie.202102487).
- Timari2022CC (43) Timári, I.; Nagy, T. M.; Kövér, K. E.; Sørensen, O. W. Synergy and sensitivity-balance in concatenating experiments in NO relaxation delay NMR (NORD). *Chem. Commun.* **2022**, *58*, 2516–2519, DOI: [10.1039/d1cc06663c](https://doi.org/10.1039/d1cc06663c).
- Orts2018M (44) Orts, J.; Gossert, A. D. Structure determination of protein-ligand complexes by NMR in solution. *Methods* **2018**, *138–139*, 3–25, DOI: [10.1016/j.ymeth.2018.01.019](https://doi.org/10.1016/j.ymeth.2018.01.019).

- (45) Schulze-Sünninghausen, D.; Becker, J.; Koos, M. R. M.; Luy, B. Improvements, extensions, and practical aspects of rapid ASAP-HSQC and ALSOFAST-HSQC pulse sequences for studying small molecules at natural abundance. *J. Magn. Reson.* **2017**, *281*, 151–161, DOI: [10.1016/j.jmr.2017.05.012](https://doi.org/10.1016/j.jmr.2017.05.012).
- (46) Vitorge, B.; Bodenhausen, G.; Pelupessy, P. Speeding up nuclear magnetic resonance spectroscopy by the use of SMALL Recovery Times – SMART NMR. *J. Magn. Reson.* **2010**, *207*, 149–152, DOI: [10.1016/j.jmr.2010.07.017](https://doi.org/10.1016/j.jmr.2010.07.017).
- (47) Shaw, A. A.; Salaun, C.; Dauphin, J.-F.; Ancian, B. Artifact-Free PFG-Enhanced Double-Quantum-Filtered COSY Experiments. *J. Magn. Reson., Ser. A* **1996**, *120*, 110–115, DOI: [10.1006/jmra.1996.0105](https://doi.org/10.1006/jmra.1996.0105).
- (48) Howe, P. W. A. Rapid pulsing artefacts in pulsed-field gradient double-quantum filtered COSY spectra. *Magn. Reson. Chem.* **2014**, *52*, 329–332, DOI: [10.1002/mrc.4060](https://doi.org/10.1002/mrc.4060).
- (49) Claridge, T. D. W.; Mayzel, M.; Kupče, Ě. Triplet NOAH supersequences optimised for small molecule structure characterisation. *Magn. Reson. Chem.* **2019**, *57*, 946–952, DOI: [10.1002/mrc.4887](https://doi.org/10.1002/mrc.4887).
- (50) Kupče, Ě.; Claridge, T. D. W. Molecular structure from a single NMR supersequence. *Chem. Commun.* **2018**, *54*, 7139–7142, DOI: [10.1039/c8cc03296c](https://doi.org/10.1039/c8cc03296c).
- (51) Kupče, Ě.; Claridge, T. D. W. New NOAH modules for structure elucidation at natural isotopic abundance. *J. Magn. Reson.* **2019**, *307*, 106568, DOI: [10.1016/j.jmr.2019.106568](https://doi.org/10.1016/j.jmr.2019.106568).
- (52) Kontaxis, G.; Stonehouse, J.; Laue, E. D.; Keeler, J. The Sensitivity of Experiments Which Use Gradient Pulses for Coherence-Pathway Selection. *J. Magn. Reson., Ser. A* **1994**, *111*, 70–76, DOI: [10.1006/jmra.1994.1227](https://doi.org/10.1006/jmra.1994.1227).
- (53) Palmer III, A. G.; Cavanagh, J.; Wright, P. E.; Rance, M. Sensitivity improvement in proton-detected two-dimensional heteronuclear correlation NMR spectroscopy. *J. Magn. Reson.* **1991**, *93*, 151–170, DOI: [10.1016/0022-2364\(91\)90036-s](https://doi.org/10.1016/0022-2364(91)90036-s).
- (54) Kay, L. E.; Keifer, P.; Saarinen, T. Pure absorption gradient enhanced heteronuclear single quantum correlation spectroscopy with improved sensitivity. *J. Am. Chem. Soc.* **1992**, *114*, 10663–10665, DOI: [10.1021/ja00052a088](https://doi.org/10.1021/ja00052a088).
- (55) Cavanagh, J.; Rance, M. Sensitivity-Enhanced NMR Techniques for the Study of Biomolecules. *Annu. Rep. NMR Spectrosc.* **1993**, *27*, 1–58, DOI: [10.1016/s0066-4103\(08\)60264-1](https://doi.org/10.1016/s0066-4103(08)60264-1).
- (56) Schleucher, J.; Schwendinger, M.; Sattler, M.; Schmidt, P.; Schedletzky, O.; Glaser, S. J.; Sørensen, O. W.; Griesinger, C. A general enhancement scheme in heteronuclear multidimensional NMR employing pulsed field gradients. *J. Biomol. NMR* **1994**, *4*, DOI: [10.1007/bf00175254](https://doi.org/10.1007/bf00175254).

- Hansen2021AC (57) Hansen, A. L.; Kupče, Ě.; Li, D.-W.; Bruschweiler-Li, L.; Wang, C.; Brüschweiler, R. 2D NMR-Based Metabolomics with HSQC/TOCSY NOAH Supersequences. *Anal. Chem.* **2021**, *93*, 6112–6119, DOI: [10.1021/acs.analchem.0c05205](https://doi.org/10.1021/acs.analchem.0c05205).
- Turner1999JMR (58) Turner, C. J.; Connolly, P. J.; Stern, A. S. Artifacts in Sensitivity-Enhanced HSQC. *J. Magn. Reson.* **1999**, *137*, 281–284, DOI: [10.1006/jmre.1998.1692](https://doi.org/10.1006/jmre.1998.1692).
- Levitt1986PNMRS (59) Levitt, M. H. Composite pulses. *Prog. Nucl. Magn. Reson. Spectrosc.* **1986**, *18*, 61–122, DOI: [10.1016/0079-6565\(86\)80005-x](https://doi.org/10.1016/0079-6565(86)80005-x).
- Foroozandeh2021A (60) Foroozandeh, M.; Singh, P. Optimal control of spins by Analytical Lie Algebraic Derivatives. *Automatica* **2021**, *129*, 109611, DOI: [10.1016/j.automatica.2021.109611](https://doi.org/10.1016/j.automatica.2021.109611).
- Wimperis1984JMR (61) Wimperis, S.; Freeman, R. An excitation sequence which discriminates between direct and long-range CH coupling. *J. Magn. Reson.* **1984**, *58*, 348–353, DOI: [10.1016/0022-2364\(84\)90227-0](https://doi.org/10.1016/0022-2364(84)90227-0).
- Sorensen1994BMR (62) Sørensen, O. W. Selective Rotations Using Non-Selective Pulses and Heteronuclear Couplings. *Bull. Magn. Reson.* **1994**, *16*, 49–53, available via https://ismar.org/wp-content/uploads/2021/09/BMR_16_049-053_1994.pdf (accessed 25 September 2022).
- Garbow1982CPL (63) Garbow, J. R.; Weitekamp, D. P.; Pines, A. Bilinear rotation decoupling of homonuclear scalar interactions. *Chem. Phys. Lett.* **1982**, *93*, 504–509, DOI: [10.1016/0009-2614\(82\)83229-6](https://doi.org/10.1016/0009-2614(82)83229-6).
- Uhrin1993JMRSa (64) Uhrin, D.; Liptaj, T.; Kover, K. E. Modified BIRD Pulses and Design of Heteronuclear Pulse Sequences. *J. Magn. Reson., Ser. A* **1993**, *101*, 41–46, DOI: [10.1006/jmra.1993.1005](https://doi.org/10.1006/jmra.1993.1005).
- Kaltschnee2014CC (65) Kaltschnee, L.; Kolmer, A.; Timári, I.; Schmidts, V.; Adams, R. W.; Nilsson, M.; Kövér, K. E.; Morris, G. A.; Thiele, C. M. “Perfecting” pure shift HSQC: full homodecoupling for accurate and precise determination of heteronuclear couplings. *Chem. Commun.* **2014**, *50*, 15702–15705, DOI: [10.1039/c4cc04217d](https://doi.org/10.1039/c4cc04217d).
- Briand1997JMR (66) Briand, J.; Sørensen, O. W. A Novel Pulse Sequence Element for Biselective and Independent Rotations with Arbitrary Flip Angles and Phases for I and IS Spin Systems. *J. Magn. Reson.* **1997**, *125*, 202–206, DOI: [10.1006/jmre.1996.1095](https://doi.org/10.1006/jmre.1996.1095).
- Briand1998JMR (67) Briand, J.; Sørensen, O. W. Simultaneous and Independent Rotations with Arbitrary Flip Angles and Phases for I, IS α , and IS β Spin Systems. *J. Magn. Reson.* **1998**, *135*, 44–49, DOI: [10.1006/jmre.1998.1556](https://doi.org/10.1006/jmre.1998.1556).
- PerezTrujillo2007MRC (68) Pérez-Trujillo, M.; Nolis, P.; Bermel, W.; Parella, T. Optimizing sensitivity and resolution in time-shared NMR experiments. *Magn. Reson. Chem.* **2007**, *45*, 325–329, DOI: [10.1002/mrc.1973](https://doi.org/10.1002/mrc.1973).
- Ni1986JMR (69) Ni, F.; Scheraga, H. A. Phase-sensitive spectral analysis by maximum entropy extrapolation. *J. Magn. Reson.* **1986**, *70*, 506–511, DOI: [10.1016/0022-2364\(86\)90145-9](https://doi.org/10.1016/0022-2364(86)90145-9).
- Tirendi1989JMR (70) Tirendi, C. F.; Martin, J. F. Fast linear prediction processing in two-dimensional NMR spectroscopy. *J. Magn. Reson.* **1989**, *81*, 577–585, DOI: [10.1016/0022-2364\(89\)90096-6](https://doi.org/10.1016/0022-2364(89)90096-6).

- Led1991CR (71) Led, J. J.; Gesmar, H. Application of the linear prediction method to NMR spectroscopy. *Chem. Rev.* **1991**, *91*, 1413–1426, DOI: [10.1021/cr00007a007](https://doi.org/10.1021/cr00007a007).
- Koehl1999PNMRS (72) Koehl, P. Linear prediction spectral analysis of NMR data. *Prog. Nucl. Magn. Reson. Spectrosc.* **1999**, *34*, 257–299, DOI: [10.1016/S0079-6565\(99\)00002-3](https://doi.org/10.1016/S0079-6565(99)00002-3).
- Donoho1990PNASUSA (73) Donoho, D. L.; Johnstone, I. M.; Stern, A. S.; Hoch, J. C. Does the maximum entropy method improve sensitivity? *Proc. Natl. Acad. Sci. U. S. A.* **1990**, *87*, 5066–5068, DOI: [10.1073/pnas.87.13.5066](https://doi.org/10.1073/pnas.87.13.5066).
- Stern2002JACS (74) Stern, A. S.; Li, K.-B.; Hoch, J. C. Modern Spectrum Analysis in Multidimensional NMR Spectroscopy: Comparison of Linear-Prediction Extrapolation and Maximum-Entropy Reconstruction. *J. Am. Chem. Soc.* **2002**, *124*, 1982–1993, DOI: [10.1021/ja011669o](https://doi.org/10.1021/ja011669o).
- Palmer2015JPCB (75) Palmer, M. R.; Suiter, C. L.; Henry, G. E.; Rovnyak, J.; Hoch, J. C.; Polenova, T.; Rovnyak, D. Sensitivity of Nonuniform Sampling NMR. *J. Phys. Chem. B* **2015**, *119*, 6502–6515, DOI: [10.1021/jp5126415](https://doi.org/10.1021/jp5126415).
- Shaka1988JMR (76) Shaka, A. J.; Lee, C. J.; Pines, A. Iterative schemes for bilinear operators; application to spin decoupling. *J. Magn. Reson.* **1988**, *77*, 274–293, DOI: [10.1016/0022-2364\(88\)90178-3](https://doi.org/10.1016/0022-2364(88)90178-3).
- Enthart2008JMR (77) Enthart, A.; Freudenberg, J. C.; Furrer, J.; Kessler, H.; Luy, B. The CLIP/CLAP-HSQC: Pure absorptive spectra for the measurement of one-bond couplings. *J. Magn. Reson.* **2008**, *192*, 314–322, DOI: [10.1016/j.jmr.2008.03.009](https://doi.org/10.1016/j.jmr.2008.03.009).
- Becker2019JMR (78) Becker, J.; Koos, M. R. M.; Schulze-Sünninghausen, D.; Luy, B. ASAP-HSQC-TOCSY for fast spin system identification and extraction of long-range couplings. *J. Magn. Reson.* **2019**, *300*, 76–83, DOI: [10.1016/j.jmr.2018.12.021](https://doi.org/10.1016/j.jmr.2018.12.021).
- Nyberg2005JACS (79) Nyberg, N. T.; Duus, J. Ø.; Sørensen, O. W. Heteronuclear Two-Bond Correlation: Suppressing Heteronuclear Three-Bond or Higher NMR Correlations while Enhancing Two-Bond Correlations Even for Vanishing $^2J_{CH}$. *J. Am. Chem. Soc.* **2005**, *127*, 6154–6155, DOI: [10.1021/ja050878w](https://doi.org/10.1021/ja050878w).
- Nyberg2005MRC (80) Nyberg, N. T.; Duus, J. Ø.; Sørensen, O. W. Editing of H2BC NMR spectra. *Magn. Reson. Chem.* **2005**, *43*, 971–974, DOI: [10.1002/mrc.1698](https://doi.org/10.1002/mrc.1698).
- Kupce2017MRC (81) Kupče, Ě.; Sørensen, O. W. 2BOB - extracting an H2BC and an HSQC-type spectrum from the same data set, and H2OBC - a fast experiment delineating the protonated ^{13}C backbone. *Magn. Reson. Chem.* **2017**, *55*, 515–518, DOI: [10.1002/mrc.4584](https://doi.org/10.1002/mrc.4584).
- Hu2011JBMR (82) Hu, K.; Westler, W. M.; Markley, J. L. Two-dimensional concurrent HMQC-COSY as an approach for small molecule chemical shift assignment and compound identification. *J. Biomol. NMR* **2011**, *49*, 291–296, DOI: [10.1007/s10858-011-9494-4](https://doi.org/10.1007/s10858-011-9494-4).
- Thrippleton2003ACIE (83) Thrippleton, M. J.; Keeler, J. Elimination of Zero-Quantum Interference in Two-Dimensional NMR Spectra. *Angew. Chem., Int. Ed.* **2003**, *42*, 3938–3941, DOI: [10.1002/anie.200351947](https://doi.org/10.1002/anie.200351947).

- Gyongyosi2018CPC (84) Gyöngyösi, T.; Timári, I.; Haller, J.; Koos, M. R. M.; Luy, B.; Kövér, K. E. Boosting the NMR Assignment of Carbohydrates with Clean In-Phase Correlation Experiments. *ChemPlusChem* **2018**, *83*, 53–60, DOI: [10.1002/cplu.201700452](https://doi.org/10.1002/cplu.201700452).
- Gyongyosi2021AC (85) Gyöngyösi, T.; Timári, I.; Sinnaeve, D.; Luy, B.; Kövér, K. E. Expedited Nuclear Magnetic Resonance Assignment of Small- to Medium-Sized Molecules with Improved HSQC-CLIP-COSY Experiments. *Anal. Chem.* **2021**, *93*, 3096–3102, DOI: [10.1021/acs.analchem.0c04124](https://doi.org/10.1021/acs.analchem.0c04124).
- Aguilar2012CC (86) Aguilar, J. A.; Nilsson, M.; Bodenhausen, G.; Morris, G. A. Spin echo NMR spectra without J modulation. *Chem. Commun.* **2012**, *48*, 811–813, DOI: [10.1039/c1cc16699a](https://doi.org/10.1039/c1cc16699a).
- Parella2019MRC (87) Parella, T. Towards perfect NMR: Spin-echo versus perfect-echo building blocks. *Magn. Reson. Chem.* **2019**, *57*, 13–29, DOI: [10.1002/mrc.4776](https://doi.org/10.1002/mrc.4776).
- Koos2016ACIE (88) Koos, M. R. M.; Kummerlöwe, G.; Kaltschnee, L.; Thiele, C. M.; Luy, B. CLIP-COSY: A Clean In-Phase Experiment for the Rapid Acquisition of COSY-type Correlations. *Angew. Chem., Int. Ed.* **2016**, *55*, 7655–7659, DOI: [10.1002/anie.201510938](https://doi.org/10.1002/anie.201510938).
- Foroozandeh2015CC (89) Foroozandeh, M.; Adams, R. W.; Kiraly, P.; Nilsson, M.; Morris, G. A. Measuring couplings in crowded NMR spectra: pure shift NMR with multiplet analysis. *Chem. Commun.* **2015**, *51*, 15410–15413, DOI: [10.1039/c5cc06293d](https://doi.org/10.1039/c5cc06293d).
- Foroozandeh2014ACIE (90) Foroozandeh, M.; Adams, R. W.; Meharry, N. J.; Jeannerat, D.; Nilsson, M.; Morris, G. A. Ultrahigh-Resolution NMR Spectroscopy. *Angew. Chem., Int. Ed.* **2014**, *53*, 6990–6992, DOI: [10.1002/anie.201404111](https://doi.org/10.1002/anie.201404111).
- Moutzouri2017CC (91) Moutzouri, P.; Chen, Y.; Foroozandeh, M.; Kiraly, P.; Phillips, A. R.; Coombes, S. R.; Nilsson, M.; Morris, G. A. Ultraclean pure shift NMR. *Chem. Commun.* **2017**, *53*, 10188–10191, DOI: [10.1039/c7cc04423b](https://doi.org/10.1039/c7cc04423b).
- Cicero2001JMR (92) Cicero, D. O.; Barbato, G.; Bazzo, R. Sensitivity Enhancement of a Two-Dimensional Experiment for the Measurement of Heteronuclear Long-Range Coupling Constants, by a New Scheme of Coherence Selection by Gradients. *J. Magn. Reson.* **2001**, *148*, 209–213, DOI: [10.1006/jmre.2000.2234](https://doi.org/10.1006/jmre.2000.2234).
- Kupce1998JMR (93) Kupče, E.; Schmidt, P.; Rance, M.; Wagner, G. Adiabatic Mixing in the Liquid State. *J. Magn. Reson.* **1998**, *135*, 361–367, DOI: [10.1006/jmre.1998.1607](https://doi.org/10.1006/jmre.1998.1607).
- Reif1996JMRSa (94) Reif, B.; Köck, M.; Kerssebaum, R.; Kang, H.; Fenical, W.; Griesinger, C. ADEQUATE, a New Set of Experiments to Determine the Constitution of Small Molecules at Natural Abundance. *J. Magn. Reson., Ser. A* **1996**, *118*, 282–285, DOI: [10.1006/jmra.1996.0038](https://doi.org/10.1006/jmra.1996.0038).
- Mareci1982JMR (95) Mareci, T. H.; Freeman, R. Echoes and antiechoes in coherence transfer NMR: Determining the signs of double-quantum frequencies. *J. Magn. Reson.* **1982**, *48*, 158–163, DOI: [10.1016/0022-2364\(82\)90250-5](https://doi.org/10.1016/0022-2364(82)90250-5).

- Hwang1995JMRS (96) Hwang, T. L.; Shaka, A. J. Water Suppression That Works. Excitation Sculpting Using Arbitrary Wave-Forms and Pulsed-Field Gradients. *J. Magn. Reson., Ser. A* **1995**, *112*, 275–279, DOI: [10.1006/jmra.1995.1047](https://doi.org/10.1006/jmra.1995.1047).

refsection:5